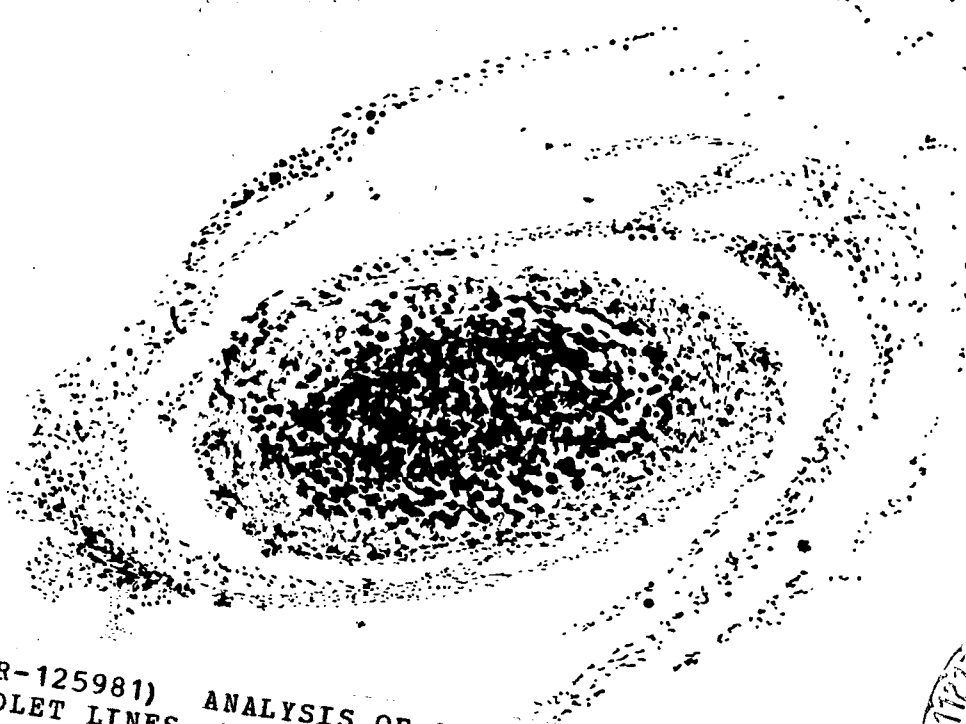


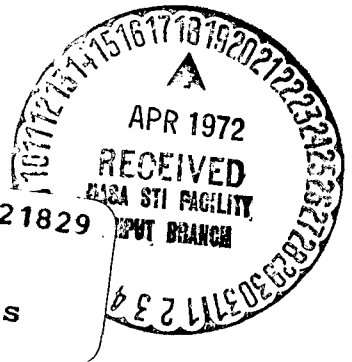
# ANALYSIS OF SOLAR ULTRAVIOLET LINES

E. CHIPMAN



(NASA-CR-125981) ANALYSIS OF SOLAR  
ULTRAVIOLET LINES E. Chipman (Smithsonian  
Astrophysical Observatory) 15 Sep. 1971  
193 p  
CSCS 03B

G3/29 Unclass  
23831



Smithsonian Astrophysical Observatory  
SPECIAL REPORT 338

CAT. 29

Research in Space Science  
SAO Special Report No. 338

ANALYSIS OF SOLAR ULTRAVIOLET LINES

Eric Chipman

Presented as a Thesis  
to the Department of Astronomy  
Harvard University  
October 1971

September 15, 1971

Smithsonian Institution  
Astrophysical Observatory  
Cambridge, Massachusetts 02138

TABLE OF CONTENTS

	<u>Page</u>
ABSTRACT . . . . .	v
1 HISTORY AND THEORY . . . . .	1
1.1 History. . . . .	1
1.2 Our Method of Solution . . . . .	7
1.2.1 The two-level case . . . . .	9
1.2.2 Multilevel atoms and statistical equilibrium . . . . .	21
1.3 Some Analytic Solutions. . . . .	28
2 ATMOSPHERES . . . . .	43
3 ATOMIC PARAMETERS . . . . .	55
3.1 Abundances . . . . .	55
3.2 Radiative Bound-Bound Rates . . . . .	55
3.3 Radiative Bound-Free Rates. . . . .	56
3.4 Collisional Bound-Bound Rates . . . . .	57
3.5 Collisional Ionization Rates . . . . .	60
3.6 Broadening Constants . . . . .	61
4 THE MAGNESIUM II H AND K LINES. . . . .	65
4.1 Introduction. . . . .	65
4.2 Observations . . . . .	67
4.3 Atomic Parameters . . . . .	67
4.4 Results. . . . .	72
4.5 General Remarks . . . . .	77
5 THE OXYGEN I RESONANCE LINES . . . . .	79
5.1 Comment on Ultraviolet Emission Lines. . . . .	79
5.2 The O I Lines — Introduction. . . . .	79
5.3 Atomic Constants . . . . .	83
5.4 Calculations and Results . . . . .	91

TABLE OF CONTENTS (Cont.)

	<u>Page</u>
6 THE CARBON II RESONANCE LINES. . . . .	115
6.1 Introduction. . . . .	115
6.2 The Observations . . . . .	115
6.3 Atomic Data and C I Ionization . . . . .	124
6.4 Calculations . . . . .	127
7 THE CARBON III LINES . . . . .	137
7.1 Introduction. . . . .	137
7.2 The Resonance Line . . . . .	139
7.3 Inclusion of the Subordinate Line. . . . .	147
8 CONCLUDING REMARKS. . . . .	157
9 ACKNOWLEDGMENTS . . . . .	163
10 REFERENCES. . . . .	165
APPENDIX: SOME REMARKS ON THE Ca II K LINE PROFILES . . . . .	A-1

## ABSTRACT

We have made a detailed study of the formation of the strongest ultraviolet emission lines of Mg II, O I, C II, and C III in the solar atmosphere. We solve the equations of statistical equilibrium and radiative transfer for each ion, using a general computer program that is capable of solving non-LTE line-formation problems for arbitrary atmospheric and atomic models. Interpreting the results in terms of the structure of the solar atmosphere, we conclude that the HSRA atmosphere has a temperature too low by about 500 K near  $h = 1100$  km and that a temperature plateau with  $T_e \approx 18,000$  K and width close to 60 km exists in the upper chromosphere. We also investigate the structure of the solar atmosphere in the range 20,000 to 100,000 K and the effects of microturbulence on the formation of lines.

We solve some approximate analytic line-formation problems relevant to the more exact solutions derived later. In the Appendix we attempt to make the best possible fit to the Ca II K line center-to-limb profiles with a one-component atmosphere, with an assumed source function and microturbulent velocity.

5

## RÉSUMÉ

Nous avons fait une étude détaillée de la formation dans l'atmosphère solaire des raies d'émission dans l'ultraviolet les plus intenses de MgII, O I, C II et C III. Nous résolvons les équations de l'équilibre statistique et du transfert radiatif pour chaque ion, en employant un programme général qui est capable de résoudre les problèmes de la formation des raies sans ETL pour des modèles atmosphériques et atomiques arbitraires. En interprétant les résultats du point de vue de la structure de l'atmosphère solaire, nous concluons que l'atmosphère HSRA a une température trop basse d'environ  $500^{\circ}\text{K}$  près de  $h = 1100$  km et qu'un plateau de la température à  $T_e \approx 18.000$  K et sur une largeur voisine de 60 km existe dans la chromosphère supérieure. Nous examinons aussi la structure de l'atmosphère solaire dans le domaine de 20.000 à 100.000 K et les effets de la microturbulence sur la formation des raies.

Nous résolvons certains problèmes analytiques et approximatifs de formation de raies applicables aux solutions plus exactes dérivées plus tard. Dans l'Appendice, nous essayons de faire concorder au mieux les profils des raies de Ca II K, du centre au bord, avec une atmosphère à une composante ayant une fonction source et une vitesse de microturbulence connues à l'avance.

## КОНСПЕКТ

Мы проделали детальное изучение образования наиболее сильных линий ультрафиолетового излучения Mg II, O I, C II и C III в солнечной атмосфере. Мы решаем уравнения статистического равновесия и излучающего переноса для каждого иона, пользуясь общей программой для электронной счетно-решающей машины способной решать задачи образования не-MTP линий для произвольных атмосферных и атомных моделей. Рассматривая результаты с точки зрения структуры солнечной атмосферы, мы пришли к выводу что атмосфера ГСЭА имеет температуру черезчур низкую, примерно на  $500^{\circ}\text{K}$  вблизи  $h=1100$  км и что температурное плато с  $T_e \approx 18000^{\circ}\text{K}$  и шириной около 16 км существует в верхней хромосфере. Мы также исследовали структуру солнечной атмосферы в диапазоне от 20000 до  $100000^{\circ}\text{K}$  и эффект микротурбулентностей на образование линий.

Мы решаем несколько приближительных и аналитических задач образования линий имеющих отношение к более точному решению выводимому позднее. В приложении мы пытаемся получить наиболее близкую пригонку к профилям центр линии-лиimbus Ca II K с однокомпонентной атмосферой с предположенной функцией источника и микротурбулентной скоростью.

# ANALYSIS OF SOLAR ULTRAVIOLET LINES

Eric Chipman

## 1. HISTORY AND THEORY

### 1.1 History

The study of spectral lines and line formation in astronomical objects has been carried on ever since the early experiments of Kirchoff and Bunsen. Using only information about wavelengths, one can identify elements that are present in a star or nebula, but one cannot obtain much more information. Schuster (1905), in his classic paper entitled "Radiation Through a Foggy Atmosphere," was the first to attack quantitatively and in detail the problem of line formation. He distinguished clearly between absorption and scattering and solved several simple cases analytically.

Many authors followed this general line of development. The so-called Schuster-Schwarzschild and Milne-Eddington models for the formation of lines were formulated and used extensively. In addition, the theory of ionization and excitation, as expressed by the Saha-Boltzmann equation, enabled astronomers to place stars on a temperature scale and implied that all normal stars have approximately equal compositions. Several workers, including Rosseland (1926) and Cillie (1932), developed the theory of line formation and radiative transfer in stellar atmospheres in terms of microscopic processes. Rosseland and Cillie were primarily concerned with the formation of emission lines in stars and nebulae, but most of their ideas can be applied to absorption lines as well. Milne (1930) summarized the current ideas on scattering and pure absorption in the formation of lines and continua.

Plaskett (1931) made a very detailed study of the Mg I b lines, which fall near  $\lambda 5184$ . He used center-to-limb observations of the line profiles and attempted to interpret these through the use of both the Schuster-Schwarzschild and the Milne-Eddington approximations. He showed that neither pure absorption nor pure coherent scattering will give the observed center-to-limb behavior of the lines. He pointed out the need for a statistical equilibrium, or non-LTE (local thermodynamic equilibrium), treatment of the transfer problem. At that time, work on strong absorption lines was somewhat hampered by the observed line profiles, which gave central intensities for the b lines almost four times larger than does more recent and more accurate work.

Korff (1932) showed that the shapes of the wings of the b lines correspond closely to the simple damping theory but are somewhat greater in absolute strength than predicted by the theory.

A series of papers collectively entitled Physical Processes in Gaseous Nebulae was published by Menzel, Baker, Aller, and Goldberg between 1937 and 1945. These papers all deal with line and continuum formation in terms of microscopic processes. Most deal with optically thin lines, but some (e.g., Baker, Aller, and Menzel, 1939) treat radiative transfer in the Lyman continuum. As in the work by Rosseland and Cillie, these papers deal primarily with planetary nebulae, but the methods can often be applied to other objects.

In the late 1940s, two groups, one in the United States and the other in Australia, began working independently on the problem of radiative transfer and non-LTE line formation in the solar chromosphere. Thomas (1948) and Giovanelli (1949) and their collaborators also made the first attempts to define a completely general non-LTE approach to the state of a stellar atmosphere or nebula. The radiation field was not treated self-consistently in these papers, however, so line formation in optically thick lines could not be dealt with accurately.

In the work of Plaskett and Korff and in other early analyses of solar absorption lines, the assumption of coherent scattering within the line was always made. That is, it was assumed that one can compute the radiative-transfer problem at each wavelength independent of all other wavelengths. This is not true, since for strong lines it is common for a photon to be absorbed at one wavelength and very soon thereafter to be reemitted at another wavelength within the same line. If the wavelengths of absorption and reemission are independent of one another, we have what is known as completely noncoherent scattering, or as complete frequency redistribution within the line, or as a frequency-independent line source function. Miyamoto (1954) found that the disk-center profiles of the Mg b lines could be explained better by noncoherent scattering theory than by coherent scattering. In his analysis, he used an assumed source function and a constant Doppler width. The center-to-limb profile variations seem, however, to correspond better to a coherent scattering theory.

The question of whether completely coherent or completely noncoherent scattering theory could adequately account for solar line profiles was debated for several years. Thomas (1957) showed that within three Doppler widths of line center, the assumption of complete frequency redistribution in the rest frame of the atom is valid. His paper was the first of an important series by Thomas, Jefferies, White, and Zirker entitled The Source Function in a Non-Equilibrium Atmosphere. These papers worked out the modern formulation of the problem of non-LTE line formation and pointed the way toward the numerical solution of realistic problems, as opposed to special analytic solutions. The interaction between different lines in multiplets was considered, as well as the general problem of multilevel, many-line line-formation cases (Jefferies, 1960). The actual methods of solution required large amounts of computing and had to await the development of electronic computers. Tomita (1960) attempted to treat the formation of the Na D lines under the assumption of noncoherent scattering. He was forced, however, to use several highly simplifying assumptions in order to make the problem tractable for hand calculation, so his results are somewhat open to question. For instance, Tomita used only one frequency point

in solving the noncoherent line-formation problem, but as we show below (see Section 1.3), this does not yield the correct source-function behavior at intermediate optical depths. In addition, in determining the Na I/Na II ionization equilibrium, he assumed a Boltzmann population distribution for the various levels of Na I, which is certainly incorrect at small optical depths. In fact, the ground state will be greatly overpopulated with respect to the excited states, and we cannot neglect photoionization from the ground state, as is implied by Tomita's Figure 1.

The question of the general validity of the assumption of complete frequency redistribution has often been raised. Jefferies and White (1960) made some calculations on the effects of collisions, and the resulting changes in velocity with respect to a stationary observer, on the redistribution of absorbed and emitted photons. The scattering was assumed to be coherent in the rest frame of the atom. Finn (1967) made detailed calculations in which he took into account the fact that complete redistribution in the rest frame of the moving atoms, such as one might find for impact collisional broadening, is not equivalent to complete redistribution in the rest frame of a stationary observer. He found considerable effects on the computed source functions, but negligible effects on the resulting line profiles. Hummer (1969) solved several cases, using a frequency-dependent isotropic source function, where he included noncoherence effects due to Doppler, natural, and collisional broadening. Hummer finds that the frequency-dependent and frequency-independent cases yield similar emergent intensities from the line center out to about three Doppler widths. Beyond this point, the frequency-dependent case approaches coherent scattering, with a resultant low emergent intensity. Hummer's neglect of continuous absorption sources, however, makes it difficult to apply his results to line formation in the sun. One source of noncoherence not treated by any of the above authors occurs in multiplets, where collisions between levels that lie close together in energy can be very rapid, approaching spontaneous radiative-transition rates. Such collisional transitions will destroy almost all coherence of absorbed and emitted photons. For most purposes, it would seem that the assumption of complete frequency redistribution throughout the line will produce reasonably accurate results.

This problem, along with the rest of the theory of line formation, is discussed in detail in Jefferies' recent book, Spectral Line Formation (1968). Another general discussion of line-formation theory is the monograph by Thomas (1965); this work contains a useful bibliography on the development of non-LTE theory.

The first series of computer programs in this field were capable of solving only problems where the Doppler width remained constant throughout the region of line formation. Such programs were used by Avrett (1965) and by Avrett and Hummer (1965) to compute the variation with optical depth of the source function for several parameterized models with constant properties through a semi-infinite atmosphere. The method of solution is described by Avrett and Loeser (1966). Using realistic model atmospheres, Johnson (1964), Finn, Mugglestone and Young (1967), and Chamaraux (1967) studied the formation of the Na D lines. Linsky (1968) studied the H and K lines of Ca II with a computer program that was similar to that of Avrett and Loeser (1966), but that was capable of solving multilevel line-formation problems.

Soon after this, a new method of simultaneous solution of the equations of radiative transfer and statistical equilibrium was developed, based on the scheme proposed by Feautrier (1964) for linearization of the problem. This method is capable of taking into account in a self-consistent way the effects of variable Doppler width through the region of line formation. Computer programs of this type were described by Cuny (1967), by Athay and Skumanich (1967), and by Avrett and Loeser (1969). Kalkofen (1968a) has described a method for the simultaneous solution of two or more strongly coupled lines; it avoids some of the convergence problems of the simpler iterative approach.

These various computer programs were first used to study the formation of the resonance lines of hydrogen (Cuny, 1968) and the H and K lines of Ca II and of Mg II (Dumont, 1967a, b; Athay and Skumanich, 1968a, b). More recently, studies have been made of the formation of lines of Na I and Mg I (Athay and Canfield, 1969) and of O I (Athay and Canfield, 1970).

This research has been of some value in elucidating the solar atmosphere, but in general no more than one or two multiplets have been studied at one time. There is a tendency for each paper to put forth a new model of the solar chromosphere, with little investigation of whether or not the results of the analyses of various lines are mutually consistent and whether or not the various derived atmospheres have essential differences. Of course, one long-recognized basic difficulty with line-profile analysis is that model atmospheres cannot be derived explicitly from line profiles; rather, one can only show that a given atmosphere is consistent with the observed profiles and realize that it is possible that other quite different atmospheres might produce equally good agreement. Nevertheless, it was felt that it would be valuable to study lines of several different atoms and ions simultaneously in an attempt to derive an atmosphere that might produce computed line profiles in agreement with the observations for as many lines as possible.

We wished to choose lines that are formed in overlapping, but not identical, regions of the solar atmosphere. We also decided to investigate some lines formed in the very high chromosphere, at temperatures approaching  $10^5$  K. After some consideration and initial experimentation, we chose to study in detail the following neutral atoms and ions: Mg II (the H and K lines), O I (the  $\lambda$  1305 triplet), C II (the  $\lambda$  1335 doublet), and C III (the  $\lambda$  977 and  $\lambda$  1176 lines). We were somewhat influenced in our choice of lines by the availability of new absolute-intensity data and limb-brightening curves for the lines of O I, C II, and C III obtained from the OSO 4 satellite. We did not investigate in detail the lines of Ca II or of hydrogen, since these species are currently being studied, with methods very similar to ours, by E. H. Avrett, J. L. Linsky, and J. Vernazza. We did in fact make a short study of the resonance K line of Ca II (see the Appendix), but this line is treated in a rather different manner than for the other lines in our work; for the K line, we have simply postulated the source function as a function of optical depth, rather than solving the line-transfer equations.

The lines of the four atomic species mentioned above are formed over the whole solar chromosphere from the temperature minimum to the highest

chromosphere. We have tried to make a self-consistent interpretation of the formation of all these lines and to determine what is implied about the structure of the solar atmosphere by the observations of these lines.

## 1.2 Our Method of Solution

For the solution of the equations of radiative transfer and statistical equilibrium reported in Sections 4 through 7, we have used a very general computer program, called PANDORA, which has been created primarily by E. H. Avrett and the programming done by R. Loeser (see Avrett and Loeser, 1969). This computer program is too large and complex to be described completely here, but we shall enumerate some of its most important features and give examples of the method of solution of some illustrative cases.

PANDORA is generalized in the sense that it can automatically set up the equations of statistical equilibrium and thus determine the parameters to be inserted in the radiative-transfer equations for any model atom chosen. The number of atomic levels and lines to be treated and the number of depth points in the model atmosphere can be arbitrary within limits set only by the memory-storage capacity of the computer. Of course, the amount of computer time required increases rapidly as the number of lines and atmospheric depth points is increased. We usually employ model atoms with from 3 to 6 levels, with up to 3 lines, and 33 to 44 depth points. One must specify the atomic parameters relevant to each level of the model atom, the transition rates between the levels, the ionization rates from each level, the model atmosphere to be used, and various other quantities. The treatment of the atomic parameters is discussed in Section 3, so here we simply assume that all these quantities are known.

In our examples, we shall see that it is necessary to know the "continuum source function," that is, the source function associated with the continuous opacity sources at the wavelength of the line under consideration. This source function is assumed constant over the small wavelength interval covered by

the line. PANDORA computes this continuum source function before solving the line-transfer problem. For a given model atmosphere, the opacities due to all the most important opacity sources are computed at each point in the atmosphere. These opacity sources include electron and Rayleigh scattering and  $H^-$  and H bound-free and free-free opacity, as well as opacity due to the neutral atoms silicon, magnesium, carbon, and aluminum. Then the equation for the continuum source function, including the effects of scattering, is solved by a matrix inversion in a manner similar to that described below for the line source function. The equation for the continuum source function is

$$S_c = \frac{\sum_Y k^Y S_c^Y}{\sum_Y k^Y}, \quad (1)$$

where  $S_c^Y$  is the constituent source function corresponding to the individual opacity  $k^Y$ . For electron and Rayleigh scattering,  $k^Y = \sigma$  and  $S_c^Y = J$ , where  $J$  is the local mean intensity of radiation at the specified wavelength. For free-free opacities and others for which LTE is assumed,  $S_c^Y = B$ , where  $B$  is the Planck function for the local electron temperature. In other cases (for bound-free hydrogen opacity in particular, and optionally for neutral carbon bound-free opacity),  $k^Y$  and  $S_c^Y$  are determined from the number densities computed by PANDORA for the particular atomic constituent.

Besides computing the continuum source function at the wavelength of any line being studied, PANDORA will compute the continuum source function and mean intensity of radiation at each depth point for one or more wavelengths within each ionization continuum for the atom under study. Thus, we can merely specify the photoionization cross section from each level, and the photoionization rates are computed automatically. Alternatively, we can specify a radiation temperature for each continuum at each depth point, and the photoionization rates will be computed on the assumption of a blackbody radiation field at this temperature.

### 1.2.1 The two-level case

As an example, let us consider the very simple case of a two-level atom with no continuum, formed in an atmosphere with some source of continuous absorption. If the populations of the two levels are assumed to be time independent, we have

$$n_1(C_{12} + \bar{J} B_{12}) = n_2(C_{21} + A_{21} + \bar{J} B_{21}) \quad , \quad (2)$$

where  $C_{12}$  and  $C_{21}$  are collisional transition rates;  $A_{21}$ ,  $B_{12}$ , and  $B_{21}$  are the Einstein A's and B's for spontaneous emission, absorption, and stimulated emission, respectively, and  $\bar{J}$  is the mean radiation field in the line, given by

$$\bar{J} = \int \Phi_\nu J_\nu d\nu \quad , \quad (3)$$

where  $\Phi_\nu$  is the line-absorption profile at frequency  $\nu$ , normalized such that

$$\int \Phi_\nu d\nu = 1 \quad . \quad (4)$$

Let us define

$$a = \frac{2 h \nu_{21}^3}{c^2} \quad , \quad (5)$$

$$\beta = e^{-h \nu_{21} / kT} \quad , \quad (6)$$

so that the Planck function is given by

$$B = \frac{a}{\beta^{-1} - 1} = \frac{a\beta}{1 - \beta} \quad , \quad (7)$$

and in LTE we have

$$\frac{n_2}{n_1} = \frac{\varpi_2}{\varpi_1} \beta \quad , \quad (8)$$

where  $\varpi_2$  and  $\varpi_1$  are the statistical weights of levels 2 and 1. Then from a consideration of the principle of detailed balance, we can readily show that

$$C_{12} = \frac{\varpi_2}{\varpi_1} \beta C_{21} \quad , \quad (9)$$

and if the density is so low that collisions are negligible, in thermodynamic equilibrium

$$n_1 B_{12} = n_2 (A_{21} + B_{21}) \quad , \quad (10)$$

which can be reduced, by using equations (8) and (7), to

$$a B_{12} = (1 - \beta) \frac{\varpi_2}{\varpi_1} A_{21} + \frac{\varpi_2}{\varpi_1} a \beta B_{21} \quad . \quad (11)$$

The Einstein A's and  $\beta$ 's must be independent of temperature (and hence of  $\beta$ ), so we equate coefficients and find

$$B_{12} = \frac{\varpi_2}{\varpi_1} \frac{A_{21}}{a} \quad (12)$$

and

$$B_{21} = \frac{A_{21}}{a} \quad . \quad (13)$$

Substituting these expressions for the  $B$ 's in equation (2) and using equation (7) for  $B$ , we can show with some algebra

$$\frac{a}{\frac{\omega_2}{\omega_1} \frac{n_1}{n_2} - 1} = \frac{\bar{J} + \frac{C_{21}}{A_{21}}(1 - \beta) B}{1 + \frac{C_{21}}{A_{21}}(1 - \beta)} \quad (14)$$

This quantity is called the source function

$$S = \frac{a}{\frac{\omega_2}{\omega_1} \frac{n_1}{n_2} - 1} \quad (15)$$

Note that  $S$  approaches  $B$  as  $n_1/n_2$  approaches its LTE value. Also it is a sufficient condition for  $S$  to equal  $B$  that either (1)  $\bar{J} = B$  or (2)  $C_{21}/A_{21} \gg 1$ , both of which we would expect from physical considerations.

We shall find it useful to define

$$\epsilon = \frac{C_{21}}{A_{21}} (1 - \beta) \quad (16)$$

and to write equation (14) as

$$S(\tau) = \frac{\bar{J}(\tau) + \epsilon(\tau) B(\tau)}{1 + \epsilon(\tau)} \quad (17)$$

where  $\tau$  is the optical depth at some frequency.

All of the above development has been used in several investigations by many workers (see Section 1.1 for references, especially those later than Thomas (1957)). In what follows, we outline a method used in our particular case to solve problems in which the Doppler width of the line varies with depth. If we represent some characteristic (constant) value of the Doppler width by  $\langle \Delta \lambda_D \rangle$  or  $\langle \Delta \nu_D \rangle$ , we can introduce a dimensionless wavelength variable

$$x = \frac{\lambda - \lambda_0}{\langle \Delta \lambda_D \rangle} = \frac{\nu - \nu_0}{\langle \Delta \nu_D \rangle} \quad (18)$$

and a new profile function

$$\phi_x(\tau) = \Delta \nu_D(\tau) \Phi_x(\tau) \quad , \quad (19)$$

with the normalization

$$\frac{2\langle \Delta \nu_D \rangle}{\Delta \nu_D(\tau)} \int_0^\infty \phi_x(\tau) dx = 1 \quad . \quad (20)$$

The profile function will in general be a Voigt profile, which is produced by combined Doppler broadening and damping and is given by

$$\phi_x(\tau) = \frac{a(\tau)}{\pi^{3/2}} \int_{-\infty}^{+\infty} \frac{e^{-z^2} dz}{[a(\tau)]^2 + \left[ z - \frac{\langle \Delta \nu_D \rangle x}{\Delta \nu_D(\tau)} \right]^2} \quad , \quad (21)$$

where

$$a(\tau) = \frac{\Gamma(\tau)}{4\pi \Delta \nu_D(\tau)} \quad (22)$$

is the ratio of damping width to Doppler width at depth  $\tau$ . If we denote a line opacity  $\kappa_L$  such that

$$\kappa_\nu = \kappa_L \phi_x \quad (23)$$

and let  $d\tau = \kappa_L dz$ , and  $r = \kappa_c / \kappa_L$ , where  $\kappa_c$  is the continuous opacity, we can write the transfer equation as

$$\frac{\mu dI_x(\tau, \mu)}{d\tau} = \phi_x(\tau) [I_x(\tau, \mu) - S(\tau)] + r(\tau) [I_x(\tau, \mu) - S_c(\tau)] \quad , \quad (24)$$

where  $S_c(\tau)$  is the continuum source function discussed above, and  $\mu$  is the cosine of the angle between the direction of propagation and the upward vertical. If we define the monochromatic optical depth  $\tau_x$  and the total source function  $S_x$  by

$$\tau_x = \int_0^{\tau} [\phi_x(t) + r(t)] dt \quad (25)$$

and

$$S_x = \frac{\phi_x S + r S_c}{\phi_x + r} \quad , \quad (26)$$

then

$$\frac{\mu dI_x(\tau_x, \mu)}{d\tau_x} = I_x(\tau_x, \mu) - S_x(\tau_x) \quad , \quad (27)$$

and the mean intensity is given by

$$J_x(\tau) = \frac{1}{2} \int_0^{\infty} E_1(|t_x - \tau_x|) S_x(t_x) dt_x \quad , \quad (28)$$

where  $E_1(\tau)$  is the first exponential integral.

The  $E_1$  function arises in the integration over angles, and in effect converts our integration over angles and optical depths into simply an integration over optical depths. This transformation depends on the fact that the line profile is not dependent on angle, so our computer program in its present form cannot treat anisotropic turbulence or systematic mass motions in atmospheres.

In what follows, let us use  $i$  and  $j$  as subscripts denoting depth points, and subscript  $k$  will denote frequency points. Then equation (3) can be rewritten, following Avrett (1971), as

$$\bar{J}_i = \sum_{k=1}^K \gamma_{ik} J_{ik} \quad , \quad (29)$$

where the  $\gamma$ 's are normalized such that

$$\sum_{k=1}^K \gamma_{ik} = 1 \quad . \quad (30)$$

Then

$$\bar{J}_i = \sum_{j=1}^N \sum_{k=1}^K \gamma_{ik} W_{ijk}^{(\Lambda)} S_{jk} \quad , \quad (31)$$

where  $\Lambda$  denotes the  $\Lambda$  operator, used in equation (28). We discuss below the determination of the coefficients  $W_{ijk}$ .

If we define

$$W_{ij}^{(\Lambda)} = \sum_{k=1}^K \gamma_{ik} W_{ijk}^{(\Lambda)} \quad (32)$$

and

$$x_{ij}^{(\Lambda)} = \sum_{k=1}^K \gamma_{ik} W_{ijk}^{(\Lambda)} \frac{r_{jk}}{\phi_{jk} + r_{jk}} \quad , \quad (33)$$

from the definition of the monochromatic source function (26), it follows that

$$\bar{J}_i = \sum_{j=1}^N \left\{ \left[ W_{ij}^{(\Lambda)} - x_{ij}^{(\Lambda)} \right] S_j + x_{ij}^{(\Lambda)} S_j^C \right\} . \quad (34)$$

Combining equation (17) with equation (34), we have

$$(1 + \epsilon_i) S_i - \sum_{j=1}^N \left[ W_{ij}^{(\Lambda)} - x_{ij}^{(\Lambda)} \right] S_j = \epsilon_i B_i + \sum_{j=1}^N x_{ij}^{(\Lambda)} S_j^C . \quad (35)$$

Here we have  $N$  equations in the  $N$  unknowns  $S_i$ , which are solved by a matrix inversion procedure.

A different equation for the  $S_i$ 's can be written in terms of the  $(\Lambda - 1)$  operator, defined by

$$\sum_{j=1}^N W_{ij}^{(\Lambda - 1)} S_j = \sum_{j=1}^N W_{ij}^{(\Lambda)} S_j - S_i , \quad (36)$$

which implies

$$(1 + \epsilon_i) S_i - \sum_{j=1}^N W_{ij}^{(\Lambda)} S_j = \epsilon_i S_i - \sum_{j=1}^N W_{ij}^{(\Lambda - 1)} S_j . \quad (37)$$

If we now write

$$\sum_{j=1}^N x_{ij}^{(\Lambda)} S_j = \sum_{j=1}^N x_{ij}^{(\Lambda - 1)} S_j + \delta_i S_i \quad (38)$$

and a similar equation in  $S_j^C$ , where

$$\delta_i = \sum_{k=1}^K \frac{\gamma_{ik} r_{ik}}{\phi_{ik} + r_{ik}}, \quad (39)$$

we can express equation (35) in the form

$$\begin{aligned} S_i &= \frac{1}{\epsilon_i + \delta_i} \sum_{j=1}^N \left[ W_{ij}^{(\Lambda-1)} - x_{ij}^{(\Lambda-1)} \right] S_j \\ &= \frac{\epsilon_i B_i + \delta_i S_i^C}{\epsilon_i + \delta_i} + \frac{1}{\epsilon_i + \delta_i} \sum_{j=1}^N x_{ij}^{(\Lambda-1)} S_j^C. \end{aligned} \quad (40)$$

As pointed out by Avrett (1971), equations (35) and (40) have the same properties and have identical solutions, provided the  $\gamma_{ik}$  coefficients are accurately normalized according to equation (30).

Athay and Skumanich (1967) have derived a version of equation (40) that gives the total source function at line center in terms of the derivative of the monochromatic fluxes:

$$S_t(0) = B + \frac{2N}{(1+r_0)(\epsilon+\delta)} \int_0^\infty \frac{\phi_x}{\phi_x + r_0} \frac{d}{d\tau_0} H_x dx, \quad (41)$$

where  $N$  is a normalizing factor arising in the normalization of the profile function, and the zeros refer to line-center quantities. This equation is closely related to equation (40) since

$$J_\nu(\tau_\nu) - S_\nu(\tau_\nu) = \frac{d}{d\tau_\nu} H_\nu(\tau_\nu) \quad (42)$$

and

$$J_{ik} - S_{ik} = \sum_{j=1}^N W_{ijk}^{(\Lambda-1)} S_{jk} \quad (43)$$

The differences between the expressions of Avrett and of Athay and Skumanich are due chiefly to different ways of determining the integral operator.

Kalkofen's (1968a) method of simultaneous solution for the source function of two or more lines involves writing the equations of statistical equilibrium as a matrix equation in column vectors of  $M$  components, where  $M$  is the number of lines. It is then possible, if we can neglect stimulated emissions, to derive  $M \times N$  linear equations in an equal number of unknowns, where  $N$  is the number of depth points. At high temperatures, stimulated emission is important, and the coupling between the source functions of different lines is nonlinear. Kalkofen describes a perturbation method for the rapid solution of the resulting nonlinear equations.

In expressing equation (28) in terms of discrete depths and frequencies, we have (omitting the  $k$  subscripts for simplicity)

$$J_i = \frac{1}{2} \int_0^{\infty} E_1(|t - \tau_i|) S(t)_j dt = \sum_{j=1}^N W_{ij}^{(\Lambda)} S_j \quad (44)$$

The coefficients  $W_{ij}^{(\Lambda)}$  can be shown to be independent of the function  $S(\tau)$ . They depend only on the given  $\tau$  values at frequency  $k$ , and on the way in which the function  $S(\tau)$  is assumed to vary between the given  $\tau$  points (that is, linearly, quadratically, etc.). For a given  $k$  or  $x$ , the  $\tau$  values are the monochromatic depths defined by equation (25).

To calculate the  $W_{ij}^{(\Lambda)}$  values (Avrett and Loeser, 1963), we let

$$S(\tau) = \sum_{j=1}^N f(\tau)_j c_j \quad (45)$$

where

$$f(\tau)_j = \begin{cases} 1 & j = 1 \\ \left(1 - \frac{\tau}{\tau_j}\right) \left(1 - \frac{\lambda\tau}{\tau_j}\right) & 0 \leq \tau \leq \tau_j \quad j = 2, 3, \dots (N-1) \\ 0 & \tau > \tau_j \quad j = 2, 3, \dots (N-1) \\ \tau & j = N \end{cases} \quad (46)$$

For  $\lambda = 1$ , this corresponds to the assumption that  $S(\tau)$  varies parabolically between the  $\tau$  points, with a slope continuous across the  $\tau$  points. We must also specify the starting slope, which is done by taking a linear variation of  $S(\tau)$  between the two deepest  $\tau$  points. For  $\lambda = 0$ , we have a linear variation from point to point, and intermediate  $\lambda$  values produce intermediate degrees of damping. In our calculations, we generally used the parabolic ( $\lambda = 1$ ) approximation, but for some extreme cases this choice produces negative source functions near the temperature minimum, and it was necessary to set  $\lambda = 0$ .

We can write the left side of equation (44) as

$$I_i = \sum_{j=1}^N G_{ij}^{(\Lambda)} c_j \quad , \quad (47)$$

where

$$G_{ij}^{(\Lambda)} = \frac{1}{2} \int_0^{\infty} E_1(|t - \tau_i|) f(t)_j dt \quad , \quad (48)$$

and from equation (45)

$$c_i = \sum_{j=1}^N f_{ij}^{-1} S(\tau_j) \quad , \quad (49)$$

where  $f_{ij}^{-1}$  is the inverse of  $f_{ij} = f(\tau_{ij})$ . From equations (44), (47), and (49), it then follows that

$$W_{ij}^{(\Lambda)} = \sum_{k=1}^N G_{ik}^{(\Lambda)} f_{kj}^{-1} \quad (50)$$

A similar development yields  $W_{ij}^{(\Lambda - 1)}$ , if we write equation (44) as

$$J_i - S(\tau_i) = \frac{1}{2} \int_0^{\infty} E_1(|t - \tau_i|) S(t)_j dt - S(\tau_i) = \sum_{j=1}^N W_{ij}^{(\Lambda - 1)} S(\tau_j) \quad (51)$$

and equation (48) as

$$G_{ij}^{(\Lambda - 1)} = \frac{1}{2} \int_0^{\infty} E_1(|t - \tau_i|) f(t)_j dt - f(\tau_i) \quad (52)$$

In practice, we have a choice of recalculating the  $W_{ij}$ 's anew for each frequency, line, and iteration, or we can calculate them once for a standard  $\tau$  set and then use the following depth transformation involving the monochromatic optical depths for calculating all the  $W_{ij}$  sets.

If we are given  $W^{(\Lambda - 1)}(x_1)_{ij}$  (or  $W^{(\Lambda)}(x_1)_{ij}$ ) at a standard  $\tau$  set corresponding to frequency  $x_1$ , we wish to find the corresponding set for another frequency  $x_2$ , where we have another set of  $\tau$  points. Let us express the left side of equation (51) as

$$G = (\Lambda - 1)S = \sum_{j=1}^N W_{ij}^{(\Lambda - 1)} S_j \quad (53)$$

where  $\Lambda - 1$  is a single operator. We use the operator  $\alpha$  to linearly interpolate from  $S$  as a function of  $\tau_{x_2}$  to  $S$  as a function of  $\tau_{x_1}$ , so

$$S(\tau_{x_1}) = \alpha S(\tau_{x_2}) \quad . \quad (54)$$

Then, using the  $\tau_{x_1}$  values, we could determine

$$G(\tau_{x_1}) = (\Lambda - 1)_{\tau_{x_1}} S(\tau_{x_1}) \quad . \quad (55)$$

Finally,  $G$  as a function of  $\tau_{x_2}$  could be determined by the linear interpolation matrix  $\beta$ :

$$G(\tau_{x_2}) = \beta G(\tau_{x_1}) \quad . \quad (56)$$

Putting these operators together, we have

$$G(\tau_{x_2}) = \beta \left[ (\Lambda - 1)_{\tau_{x_1}} \left( \alpha S_{\tau_{x_2}} \right) \right] \quad , \quad (57)$$

which is the same as

$$G(\tau_{x_2}) = \left[ \beta (\Lambda - 1)_{\tau_{x_1}} \alpha \right] S(\tau_{x_2}) \quad . \quad (58)$$

The matrix  $\left[ \beta (\Lambda - 1)_{\tau_{x_1}} \alpha \right]$  is, apart from the interpolation approximations, the same as  $(\Lambda - 1)_{\tau_{x_2}}$  or  $W_{x_2}^{(\Lambda - 1)}_{ij}$ , which avoids the recomputation of all the  $W_{ij}$ 's from the definition. The matrices  $\alpha$  and  $\beta$  are easily derived and are all zeros except for two numbers in each row or column, respectively.

This procedure, called "mapping," can save approximately 30% of the computer time used otherwise, but it has its hazards. There appears to be a systematic error of a few percent in the surface values of source functions derived by using the mapping technique. What is more, if we have more than two  $\tau$  points that fall between a given adjacent pair of  $\tau$  points in our "standard"  $\tau$  set, the central points are not treated correctly, in that their source functions are ignored in computing the intensity integrals. This problem does not generally arise for most strong lines, but for lines such as the C II and C III resonance lines, the mapping method is not usable.

Kalkofen (1968b) has investigated the relative accuracy of results obtained, using linear and parabolic interpolation in the transformations from the pre-tabulated  $W_{ij}$  matrix used in the mapping procedure to the  $W_{ijk}$ 's that are finally used. For an atmosphere with  $B$  and  $\epsilon$  constant, he found typical errors in surface value of the source function of 1% for linear and 0.1% for quadratic interpolation, although in some instances, the linear results were as bad as 6%. The mapping subroutine in PANDORA was written by using linear interpolation. In those cases where accuracy seemed important, we bypassed the mapping procedure and had the program calculate each  $W_{ijk}$  directly. The source functions at wavelengths in the ionization continua are always calculated without using the mapping procedure.

The simple two-level problem is an instructive example, and the curves given by Avrett (1965) and by Hummer (1968) show many aspects of the problem. In particular, we should note that for  $B = 1$  (constant) and constant  $\epsilon$ ,  $S$  departs from  $B$  first at  $\tau \approx 1/\epsilon$  ( $\tau$  = line-center optical depth) and reaches a minimum value of  $S = \sqrt{\epsilon}$  in the surface region  $\tau \lesssim 10^{-1}$ . These are useful indications of the range of line  $\tau$ , which we must consider in a non-LTE problem. In this approximation, the residual intensity at line center is  $2\sqrt{\epsilon}$ .

### 1.2.2 Multilevel atoms and statistical equilibrium

In most cases of interest, one must consider three or more energy levels, plus a continuum, in order to represent reasonably the physical situation.

When there is more than one radiative transition to be solved, we cannot solve the whole problem at once, but must iterate, solving each transition by using parameters for the others derived from the last iteration. We will develop the mathematics for multilevel atoms in a general form first, and then give an example, for the three-level case.

In a steady state, the number of transitions into and out of any level must be equal, so we have

$$n_{\ell} \left( \sum_{\substack{m=1 \\ m \neq \ell}}^N P_{\ell m} + P_{\ell K} \right) = \sum_{\substack{m=1 \\ m \neq \ell}}^N n_m P_{m\ell} + n_K P_{K\ell} \quad , \quad (59)$$

where  $n_K$  represents the number density of ionized atoms,  $P_{\ell m}$  is the transition rate per atom in level  $\ell$  per unit time to level  $m$ .  $P_{\ell K}$  and  $P_{K\ell}$  represent ionization and recombination. The equation for the continuum is

$$n_K \sum_{\ell=1}^N P_{K\ell} = \sum_{\ell=1}^N n_{\ell} P_{\ell K} \quad , \quad (60)$$

which can be used, along with equation (59) and the specified total number of atoms

$$n = n_K + n_1 + n_2 + \dots + n_N \quad (61)$$

to eliminate  $n_K$ . Now define

$$P_{ij} = \frac{P_{iK} P_{Kj}}{\sum_{\ell=1}^N P_{K\ell}} \quad (62)$$

so that equation (59) becomes

$$n_l \sum_{\substack{m=1 \\ m \neq l}}^N (P_{lm} + P_{lm}') = \sum_{\substack{m=1 \\ m \neq l}}^N n_m (P_{ml} + P_{ml}') \quad . \quad (63)$$

If we define the integrated mean intensity

$$\bar{J}_{ji} = \frac{1}{4\pi} \int d\omega \int d\nu \Phi_\nu I_\nu(\omega) \quad , \quad (64)$$

where  $I_\nu(\omega)$  is the specific intensity for solid angle  $\omega$ , and the line source function

$$S_{ji} = \frac{2h\nu_{ji}^3/c^2}{\frac{\omega_j}{\omega_i} \frac{n_i}{n_j} - 1} \quad , \quad (65)$$

we can then define the net radiative bracket

$$\rho_{ji} = 1 - \frac{\bar{J}_{ji}}{S_{ji}} \quad , \quad (66)$$

which is a measure of the lack of detailed balance of upward and downward radiative transitions in the  $ji$  line. Finally, we have

$$n_j (A_{ji} + B_{ji} \bar{J}_{ji}) - n_i B_{ij} \bar{J}_{ji} = n_j A_{ji} \rho_{ji} \quad , \quad (67)$$

where we have used the Einstein A's and B's.

For our purposes, it is more convenient to use in place of the  $n_i$ 's the departure coefficients, and, in particular, the ratios of the  $b_i$ 's defined by

$$\frac{b_j}{b_i} = \frac{n_j}{n_j^*} \frac{n_i^*}{n_i} \quad , \quad (68)$$

where  $n_i^*/n_j^*$  is the ratio defined by the Boltzmann equation. If we also say

$$\gamma_\ell = \omega_\ell e^{-h\nu_{\ell 1}/kT} \quad (69)$$

and define  $A'_{mn} = \gamma_m A_{mn}$ ,  $C'_{mn} = \gamma_m C_{mn}$ , and  $P'_{mn} = \gamma_m P_{mn}$ , we can write the statistical equilibrium equation (63) as

$$\begin{aligned} b_\ell \left[ \sum_{i=1}^{\ell-1} A'_{\ell i} \rho_{\ell i} + \sum_{\substack{m=1 \\ m \neq \ell}}^N (C'_{\ell m} + P'_{\ell m}) \right] \\ = \sum_{j=\ell+1}^N b_j A'_{j\ell} \rho_{j\ell} + \sum_{\substack{m=1 \\ m \neq \ell}}^N b_m (C'_{m\ell} + P'_{m\ell}) \quad . \end{aligned} \quad (70)$$

Note also that with our definitions,  $C'_{ij} = C'_{ji}$ .

We wish to relate the departure coefficients to the source-function equation in the form of (35), which is the equation that we actually solve. To do this, we note that the equation

$$\frac{b_u}{b_L} (\rho_{uL} + \epsilon_1) = \epsilon_2 \quad (71)$$

is equivalent to

$$S_{uL} = \frac{\bar{J}_{uL} + (1 - \beta) \epsilon_2 B_{uL}}{1 + (\epsilon_1 - \beta \epsilon_2)} \quad , \quad (72)$$

with our previous definition of  $\beta$  (equation 6), which follows from the definition of  $\rho$  (equation 66) and equation (65), which can be expressed as

$$S_{uL} = \frac{2 h \nu_{uL}^3 / c^2}{\frac{b_L}{b_u} e^{h \nu_{uL} / kT} - 1} \quad . \quad (73)$$

For the case of the two-level atom with no continuum, we have

$\epsilon_1 = \epsilon_2 = C_{21} / A_{21}$ , but in general the  $\epsilon$ 's are different and are rather complex functions of the various  $b$ 's,  $A$ 's,  $C$ 's, and  $\rho$ 's of the problem, not including  $b_u / b_L$  or  $\rho_{uL}$ . As an example, let us consider the case of the three-level Mg I problem, with a continuum. The energy-level diagram for this model atom is given in Figure 1 and the statistical-equilibrium equations are

$$b_1 (C'_{12} + P'_{12} + P'_{13}) = b_2 (P'_{21} + C'_{21}) + b_3 (P'_{31}) \quad , \quad (74a)$$

$$b_2 (C'_{21} + C'_{23} + P'_{23} + P'_{21}) = b_3 (A'_{32} \rho_{32} + C'_{32} + P'_{32}) + b_1 (P'_{12} + C'_{12}) \quad , \quad (74b)$$

and

$$b_3 (C'_{32} + P'_{32} + P'_{31} + A'_{32} \rho_{32}) = b_1 P'_{13} + b_2 (C'_{23} + P'_{23}) \quad . \quad (74c)$$

This problem has only one radiative transition, for which we can write equation (71) in two ways: first, from (74b),

$$\frac{b_3}{b_2} \left( \rho_{32} + \frac{C'_{32} + P'_{32}}{A'_{32}} \right) = \frac{C'_{21} + C'_{23} + P'_{23} + P'_{21}}{A'_{32}} - \frac{b_1}{b_2} \left( \frac{P'_{12} + C'_{12}}{A'_{32}} \right) \quad , \quad (75a)$$

and from (67c),

$$\frac{b_3}{b_2} \left( p_{32} + \frac{C'_{32} + P'_{32} + P'_{31}}{A'_{32}} \right) = \frac{C'_{23} + P'_{23}}{A'_{32}} + \frac{b_1}{b_2} \frac{P'_{13}}{A'_{32}} \quad (75b)$$

These two equations yield different values of  $\epsilon_1$  and  $\epsilon_2$  in general, so we will have different forms of equation (72). In practice, we could solve both versions of equation (72) and use some weighted mean of the two solutions as our solution for the next iteration. The weights can be chosen so as to achieve the fastest, most stable convergence to the solution. At convergence, the solution will change very slowly from one iteration to the next, and we will require certain products of the ratios of the b's to approach unity, although the factors are computed independently of each other. For instance,

$$\left( \frac{b_2}{b_1} \right) \left( \frac{b_3}{b_2} \right) \left( \frac{b_1}{b_3} \right) = 1 \quad (76)$$

107-096

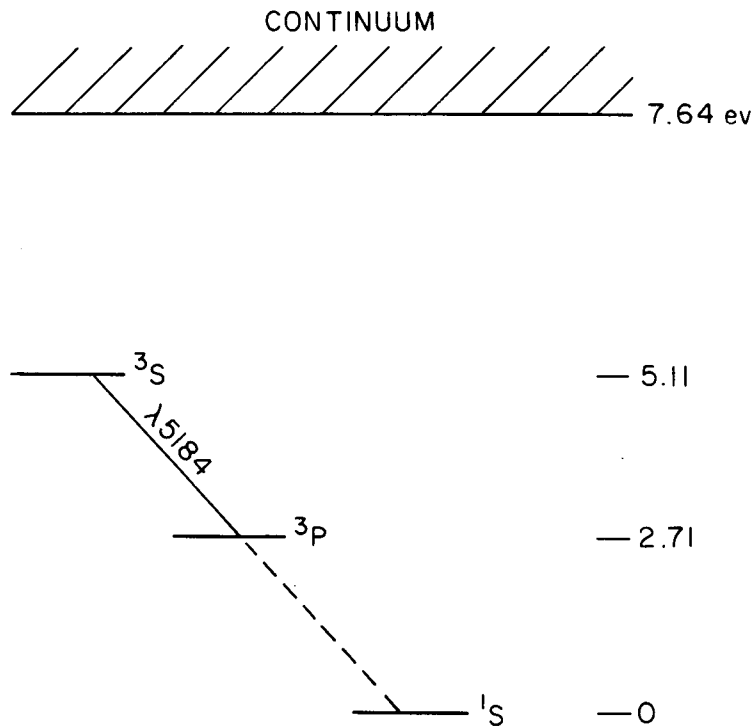


Figure 1. Energy levels for a three-level model Mg I atom.

Alternatively, we can use the N equations (74) for an N-level atom to eliminate all the b's except for the ratio  $b_u/b_L$  for the transition in question. We will find that we can express equation (71) now in such a way that  $\mathbf{\epsilon}_1$  and  $\mathbf{\epsilon}_2$  contain only the P's, C's, A's, and the  $\rho$ 's for other transitions, but do not contain  $\rho_{uL}$  or any b's, as equations (75) do. This method leads to faster and more certain convergence of the equations for the various radiative transitions in question. As an illustration, let us develop this method for the three-level case discussed above. Eliminating  $b_1/b_2$  in equations (75), we have

$$\begin{aligned} & \frac{b_3}{b_2} \left[ \rho_{32} + \frac{1}{A'_{32}} \left( C'_{32} + P'_{32} + \frac{P'_{31} P'_{12} + P'_{31} C'_{12}}{P'_{13} + P'_{12} + C'_{12}} \right) \right] \\ & = \frac{1}{A'_{32}} \left( C'_{32} + P'_{23} + \frac{C'_{21} P'_{13} + P'_{21} P'_{13}}{P'_{13} + P'_{12} + C'_{12}} \right) ; \end{aligned} \quad (77)$$

in this case,

$$\mathbf{\epsilon}_1 = \frac{1}{A'_{32}} \left( C'_{32} + P'_{32} + \frac{P'_{31} P'_{12} + P'_{31} C'_{12}}{P'_{13} + P'_{12} + C'_{12}} \right) \quad (78)$$

and

$$\mathbf{\epsilon}_2 = \frac{1}{A'_{32}} \left( C'_{32} + P'_{23} + \frac{C'_{21} P'_{13} + P'_{21} P'_{13}}{P'_{13} + P'_{12} + C'_{12}} \right) . \quad (79)$$

Note that  $\mathbf{\epsilon}_1$  and  $\mathbf{\epsilon}_2$  do not depend on any b ratios. Since there is only one radiative transition in this case,  $\mathbf{\epsilon}_1$  and  $\mathbf{\epsilon}_2$  do not depend on any  $\rho$  values; iteration is necessary only to determine the optical depth scale, which depends weakly on the  $\rho$ 's. In this respect, we have linearized the basically nonlinear radiative-transfer equation, so we would not expect to obtain an exact solution in one iteration.

The solution for the three-level Mg I case converges in three or four iterations. For the four-level Mg I case, which includes the  $\lambda 2852$  line, rapid convergence is again obtained, since the two lines have no level in common. For the five- and six-level cases, which include all three of the b lines, a straightforward iteration approach leads to oscillations of the  $\rho$ 's rather than to convergence. It is necessary to damp the solutions by averaging the  $\rho$ 's from the last iteration with the current  $\rho$ 's in order to obtain convergence, which occurs within about eight iterations in our cases.

In principle, there is no limit to the number of levels and radiative transitions that can be treated in this way. However, the amount of computing time necessary becomes large when many lines are considered, so we would like to use a model that contains the minimum complexity necessary to produce the desired or observed accuracy and to reproduce the interesting features of the problem.

### 1.3 Some Analytic Solutions

Realistic solutions to physical line-transfer problems require the use of a computer, and even the idealized cases described by Avrett (1965) for homogeneous atmospheres and extended considerably by Hummer (1968) required computer solution because of the complexities of complete frequency redistribution with a Gaussian or Voigt line profile. However, if we use a rectangular or step-function line profile, and if we approximate the  $E_1$  exponential integral function by an exponential, it is possible to derive analytic solutions for a variety of problems. One can include continuous as well as line opacity, and the Planck function may be constant, or it may have one or more discontinuities at specified optical depths. This type of analytic solution has been described by Avrett (1969). We shall solve several cases here and will discuss the implications of these solutions where relevant in later sections. Our first example below, which is the simplest possible case, was solved by Avrett (1969), but the other examples are original.

Consider first the equation

$$S = (1 - \epsilon) \bar{J} + \epsilon B \quad , \quad (80)$$

which is a slightly rewritten form of (17), with

$$\epsilon = \frac{\epsilon}{1 + \epsilon} \quad . \quad (81)$$

If we now consider a rectangular line profile, such that

$$\begin{aligned} \phi_x &= 1 & \text{for} & \quad 0 \leq x \leq 1/2 \quad , \\ &= 0 & \text{for} & \quad x > 1/2 \quad , \end{aligned} \quad (82)$$

which preserves the normalization, and if we approximate the  $E_1$  function by

$$E_1(x) = \frac{b}{2} e^{-bx} \quad , \quad (83)$$

where  $b$  is chosen by some "best-fit" criterion, such as, for example,  $b = \sqrt{3}$ , we can write

$$S(\tau) = (1 - \epsilon) \frac{1}{2} \int_0^{\infty} b e^{-b(|\tau - t|)} S(t) dt + \epsilon B(\tau) \quad . \quad (84)$$

Let us solve first the case of a semi-infinite atmosphere with constant temperature, i. e. , constant  $B(\tau) = B$ . We can express (84) as

$$S(\tau) = (1 - \epsilon) \frac{b}{2} \left[ \int_0^{\tau} e^{-b(\tau - t)} S(t) dt + \int_{\tau}^{\infty} e^{-b(t - \tau)} S(t) dt \right] + \epsilon B \quad , \quad (85)$$

which is differentiated twice, to give

$$S'(\tau) = (1 - \epsilon) \frac{b}{2} \left[ -be^{-b\tau} \int_0^{\tau} e^{bt} S(t) dt + be^{b\tau} \int_{\tau}^{\infty} e^{-bt} S(t) dt \right] \quad (86)$$

and

$$S''(\tau) = (1 - \epsilon) \frac{b}{2} \left[ b^2 e^{-b\tau} \int_0^{\tau} e^{bt} S(t) dt + b^2 e^{b\tau} \int_{\tau}^{\infty} e^{-bt} S(t) dt \right] - b^2 (1 - \epsilon) S(\tau) \quad (87)$$

or, upon substitution of the integrals from (85),

$$S''(\tau) = b^2 [S(\tau) - \epsilon B] - b^2 (1 - \epsilon) S(\tau) \quad (88)$$

$$= b^2 \epsilon [S(\tau) - B] \quad (89)$$

This differential equation has the general solution

$$S(\tau) = A e^{b\sqrt{\epsilon} \tau} + C e^{-b\sqrt{\epsilon} \tau} + B \quad (90)$$

We can set  $A = 0$ , because of the boundary condition requiring that  $S \rightarrow B$  as  $\tau \rightarrow \infty$ , and substitute this expression in (85) to evaluate  $C$ . Upon doing the integrations, we have

$$C e^{-b\sqrt{\epsilon} \tau} + B = (1 + \sqrt{\epsilon}) \left(\frac{C}{2}\right) (e^{-b\sqrt{\epsilon} \tau} - e^{-b\tau}) + (1 - \epsilon) \left(\frac{B}{2}\right) (1 - e^{-b\tau}) + (1 - \sqrt{\epsilon}) \left(\frac{C}{2}\right) (e^{-b\sqrt{\epsilon} \tau} - e^{b\tau}) + (1 - \epsilon) \left(\frac{B}{2}\right) (1 - e^{b\tau}) \quad (91)$$

which, upon equating coefficients of  $e^{-b\tau}$ , yields

$$C = -(1 - \sqrt{\epsilon}) B \quad ; \quad (92)$$

so

$$S(\tau) = B [1 - (1 - \sqrt{\epsilon}) e^{-b\sqrt{\epsilon} \tau}] \quad . \quad (93)$$

This expression contains the correct value for the source function at  $\tau=0$ ,  $S(0) = \sqrt{\epsilon} B$  (see Avrett, 1965). However, our analytic formula predicts that the source function approaches  $B$  at an optical depth of approximately  $\sqrt{\epsilon}^{-1}$  (since  $b \approx 1$ ), whereas exact calculations with a Gaussian line profile give  $S \approx B$  at  $\tau \approx \epsilon^{-1}$ . The difference is caused by the effects of escape of photons in the line wings in the Gaussian case. We have plotted schematically in Figure 2 the source functions for the analytic and exact cases.

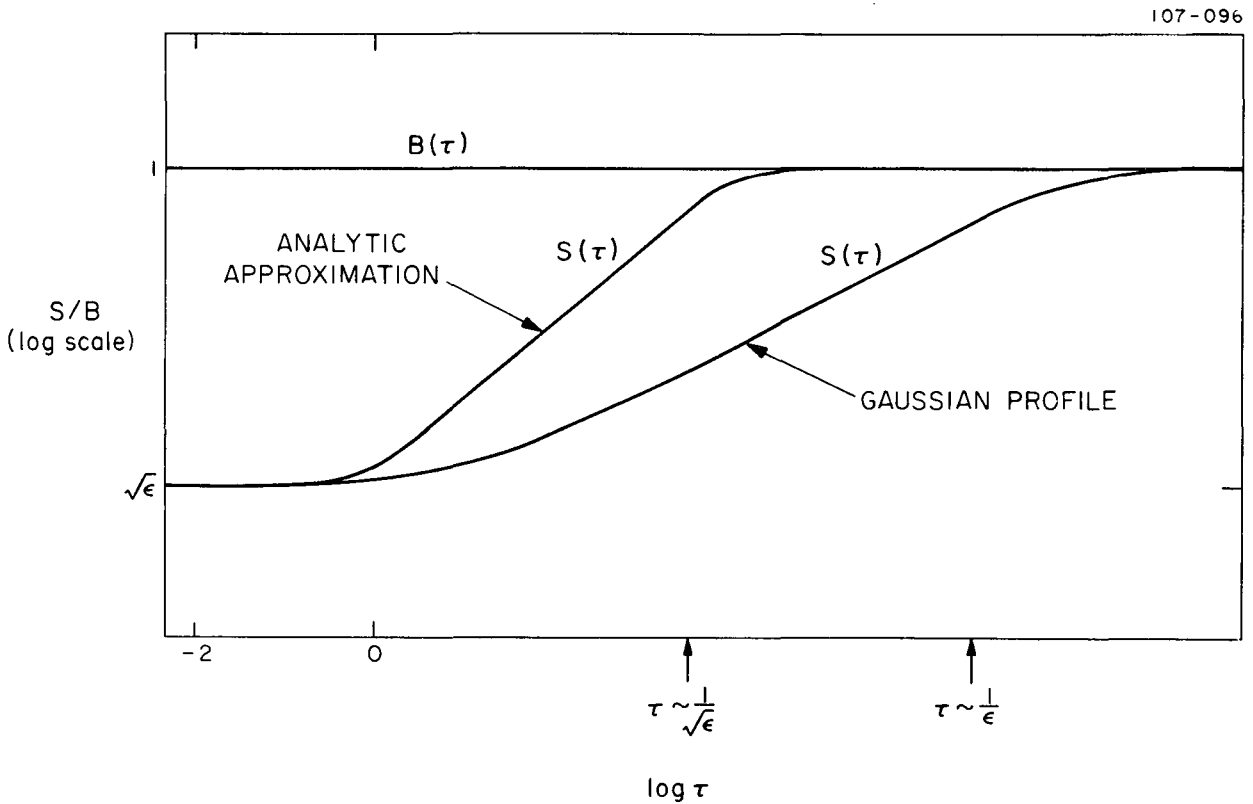


Figure 2. Source functions in two approximations.

In this approximation, we will discuss several problems of some possible application to the various line-transfer problems considered in later sections. In each instance, the general method of solution is the same: double differentiation to convert the original integral equation into a differential equation, for which we find the general solution and substitute back into the integral to evaluate the arbitrary constants, subject to the boundary conditions. We shall not give details of intermediate steps of any further solutions but merely a statement of the problem, an outline of the method, and the final solution.

A case of some interest in connection with several different lines is that of a line formed in an atmosphere with a discontinuity in microturbulent velocity, such that the line profile changes at some depth. Dumont (1966) showed that in semirealistic cases such a situation could result in an increase of the surface value of the source function by a factor of 2 to 5, if  $\Delta\lambda_D$  increases by a factor 4 near  $\tau_0 = 10$ . Consider the diagram in Figure 3. In Figure 3, we show a situation where the profile for  $\tau < \bar{\tau}$  is twice as broad as for  $\tau > \bar{\tau}$ . There is continuous opacity for  $\tau > \bar{\tau}$ , but we set  $r = \kappa_c / \kappa_L = 0$  for  $\tau < \bar{\tau}$ .  $B$  is a constant throughout the atmosphere.

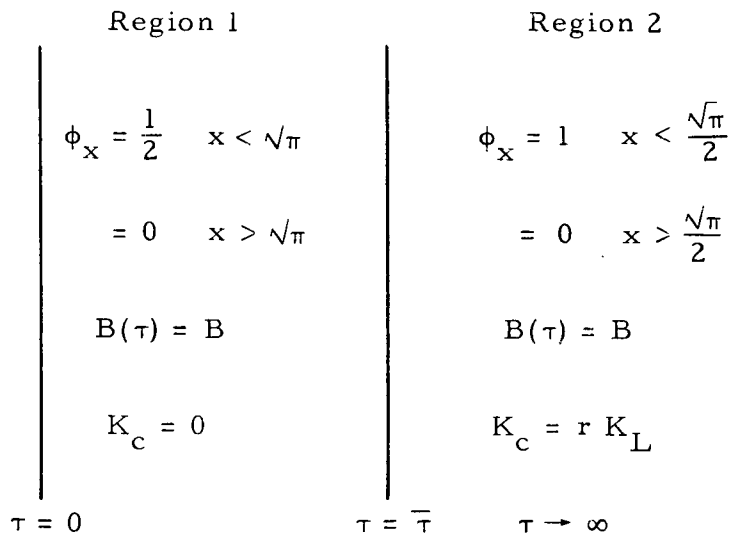


Figure 3. Diagram of profile discontinuity case.

A situation of this sort, if occurring in a real atmosphere, might have the effect of increasing the observed central intensity in the line, without grossly distorting the observed line profile. This is achieved, in effect, by feeding photons absorbed in the wings of the line in the turbulent surface layers into the core of the line. Since the line wings in a thin surface layer will see a radiation field arising from the photosphere equal to  $1/2 B$ , the source function would be expected to rise in the surface layer over the base value of  $\sqrt{\epsilon} B$ . We would expect that as  $\bar{\tau} \rightarrow 0$  and as  $\bar{\tau} \rightarrow \infty$  we would observe an emergent intensity equal to  $\sqrt{\epsilon} B$ , but for intermediate values of  $\bar{\tau}$  we will observe an intensity greater than  $\sqrt{\epsilon} B$ . We shall find the result that  $S(\tau=0)$  approaches  $B/4$  rather than  $\sqrt{\epsilon} B$  as  $\bar{\tau}$  approaches zero, but the observed line-center intensity does indeed reach a maximum. The value of this maximum and the associated value of  $\bar{\tau}$  are of interest.

In what follows let us set  $b$ , the fitting parameter for the  $E_1$  function, equal to 1. This will not change our results materially and will make the algebra a bit easier. Also let us write our previous quantity  $\epsilon$  as  $\epsilon_1$  and define

$$\epsilon_2 = \frac{r}{1+r} \approx r = \frac{\kappa_c}{\kappa_L} \quad . \quad (94)$$

First, consider the situation where we neglect absorption in the surface layer and treat it as a pure scattering line. In this case,  $\epsilon_1 = 0$  in the surface layer. In the surface layer,  $S = \bar{J}$ , and our differential equations for the two layers become

$$S_1'' = 0 \quad (95a)$$

and

$$S_2'' = \epsilon_3 S_2 - \epsilon_3 B \quad , \quad (95b)$$

where

$$\epsilon_3 = \epsilon_1 + \epsilon_2 - \epsilon_1 \epsilon_2 \quad . \quad (96)$$

The general solution in region 1 is

$$S_1(\tau) = A_1 + C_1 \tau \quad , \quad (97a)$$

and in region 2,

$$S_2(\tau) = C_2 e^{-\sqrt{\mathbf{E}}_3 \tau} + B \quad . \quad (97b)$$

Upon substitution into the integral equations for regions 1 and 2, we find for region 1

$$\begin{aligned} 0 = A_1 (-e^{-\tau} - e^{\tau-\bar{\tau}}) + C_1 (e^{-\tau} - \bar{\tau} e^{\tau-\bar{\tau}} - e^{\tau-\bar{\tau}}) + \frac{C_2}{2(1+\sqrt{\mathbf{E}})} e^{\tau-\bar{\tau}-\sqrt{\mathbf{E}} \bar{\tau}} \\ + B e^{\tau-\bar{\tau}} \quad . \end{aligned} \quad (98)$$

In this equation, we can equate coefficients of  $e^{-\tau}$ , with the result

$$C_1 = A \quad . \quad (99)$$

The equation for region 2 yields

$$0 = A_1 \bar{\tau} - \frac{C_2 e^{-\sqrt{\mathbf{E}} \bar{\tau}}}{1-\sqrt{\mathbf{E}}} - B \quad . \quad (100)$$

Now equations (98), (99), and (100) can be solved for  $A_1$  and hence for  $S_1(\tau)$ , and we obtain, omitting terms of order  $\sqrt{\mathbf{E}}$  in comparison with terms of order unity,  $\tau$  and  $\bar{\tau}$ ,

$$S_1(\tau) = B \left( \frac{1+\tau}{4+\tau} \right) \quad . \quad (101)$$

We could see that the value of  $S(0)$  should be  $B/4$  for  $\bar{\tau} = 0$ , since half the line profile at the surface sees directly down to the photosphere, where it sees a brightness  $B$ , diluted by a factor 2. One might expect that some effect such as this could be important in determining the intensities at line centers, since  $B/4 \gg \sqrt{\epsilon} B$ .

In the more general case, we must consider a finite  $\epsilon_1$  in the surface layer. Then the source-function equation in region 1 is

$$S_1(\tau) = (1 - \epsilon_1) \frac{1}{2} \int_0^{\bar{\tau}} e^{-|\tau-t|} S_1(t) dt + \frac{1}{2} (1 - \epsilon_1) \frac{1}{2} \int_{\bar{\tau}}^{\infty} e^{-|t-\tau|} \left[ (1 - \epsilon_2) S_2(t) + \epsilon_2 B \right] dt + \frac{1}{2} (1 - \epsilon_1) \frac{1}{2} \int_{\bar{\tau}}^{\infty} e^{-|t-\tau|} B dt + \epsilon_1 B \quad , \quad (102a)$$

and in region 2 is

$$S_2(\tau) = (1 - \epsilon_1) \frac{1}{2} \int_0^{\bar{\tau}} e^{-|\tau-t|} S_1(t) dt + (1 - \epsilon_1) \frac{1}{2} \int_{\bar{\tau}}^{\infty} e^{-|t-\tau|} \left[ (1 - \epsilon_2) S_2(t) + \epsilon_2 B \right] dt + \epsilon_1 B \quad . \quad (102b)$$

Double differentiation gives

$$S_1'' = \epsilon_1 S_1 - \epsilon_1 B \quad (103a)$$

and

$$S_2'' = (\epsilon_1 + \epsilon_2 - \epsilon_1 \epsilon_2) (S_2 - B) = \epsilon_3 (S_2 - B) \quad . \quad (103b)$$

So the solutions will be

$$S_1(\tau) = A_1 e^{\sqrt{\epsilon_1} \tau} + C_1 e^{-\sqrt{\epsilon_1} \tau} + B \quad , \quad (104a)$$

$$S_2(\tau) = A_2 e^{\sqrt{\epsilon_3} \tau} + C_2 e^{-\sqrt{\epsilon_3} \tau} + B \quad . \quad (104b)$$

We require  $S \rightarrow B$  as  $\tau \rightarrow \infty$ , so  $A_2 = 0$ . We must therefore determine  $A_1$ ,  $C_1$ , and  $C_2$  by substitution into equations (102). In this way, we derive three equations in  $A_1$ ,  $C_1$ , and  $C_2$ :

$$0 = A_1(1 - \sqrt{\epsilon_1}) + C_1(1 + \sqrt{\epsilon_1}) + B(1 - \epsilon_1) \quad , \quad (105a)$$

$$0 = A_1(1 + \sqrt{\epsilon_1}) e^{\bar{\tau}\sqrt{\epsilon_1}} + C_1(1 - \sqrt{\epsilon_1}) e^{-\bar{\tau}\sqrt{\epsilon_1}} - \frac{C_2(1 - \epsilon_1)}{2(1 + \sqrt{\epsilon_3})} e^{-\bar{\tau}\sqrt{\epsilon_3}} \quad , \quad (105b)$$

$$0 = A_1(1 - \sqrt{\epsilon_1}) e^{\bar{\tau}\sqrt{\epsilon_1}} + C_1(1 + \sqrt{\epsilon_1}) e^{-\bar{\tau}\sqrt{\epsilon_1}} - C_2(1 + \sqrt{\epsilon_3}) e^{-\bar{\tau}\sqrt{\epsilon_3}} \quad . \quad (105c)$$

Solving, we find

$$A_1 = \frac{-B(1 + \sqrt{\epsilon_1}) e^{-2\bar{\tau}\sqrt{\epsilon_1}} \gamma}{e^{-2\bar{\tau}\sqrt{\epsilon_1}} \gamma - \frac{1 + \sqrt{\epsilon_1}}{1 - \sqrt{\epsilon_1}}} \quad (106)$$

and

$$C_1 = \frac{B(1 + \sqrt{\epsilon_1})}{e^{-2\bar{\tau}\sqrt{\epsilon_1}} \gamma - \frac{1 + \sqrt{\epsilon_1}}{1 - \sqrt{\epsilon_1}}} \quad , \quad (107)$$

where  $\gamma$  is of order unity and is defined by

$$\gamma = \left[ \frac{2(1 + \sqrt{\epsilon_3})^2 (1 - \sqrt{\epsilon_1}) - (1 + \sqrt{\epsilon_1})^2 (1 - \sqrt{\epsilon_1})}{2(1 + \sqrt{\epsilon_3})^2 (1 + \sqrt{\epsilon_1}) - (1 - \sqrt{\epsilon_1})^2 (1 + \sqrt{\epsilon_1})} \right] . \quad (108)$$

This solution has the expected asymptotic behavior. For  $\bar{\tau}$  very large,  $A_1$  approaches zero, and the first term in the denominator of  $C_1$  becomes negligible, so we find

$$S_1(\tau) = B \left\{ \frac{1 + e^{-\sqrt{\epsilon_1} \tau} (1 + \sqrt{\epsilon_1})}{1 - [(1 + \sqrt{\epsilon_1})(1 - \sqrt{\epsilon_1})]} \right\} = B \left[ (1 - e^{-\sqrt{\epsilon_1} \tau} (1 - \sqrt{\epsilon_1})) \right] . \quad (109)$$

For  $\bar{\tau} \rightarrow 0$ , we expand  $\gamma$  to order  $\sqrt{\epsilon}$ , which yields

$$\gamma = 1 - 6 \sqrt{\epsilon_1} , \quad (110)$$

and for  $\tau = \bar{\tau} = 0$ , we have the same result as before (equation 101), or we can include terms of order  $\epsilon$  in our expansion, and we have

$$S = B \left[ \frac{1 + \tau(1 - 2\sqrt{\epsilon_1}) - 3\sqrt{\epsilon_1} - \bar{\tau}\sqrt{\epsilon_1}}{4 + \bar{\tau}(1 - 6\sqrt{\epsilon_1})} \right] . \quad (111)$$

Thus, if we approximate the emergent intensity by  $S(\tau=1)$ , we find this quantity is a maximum for  $\tau = \bar{\tau} = 1$ , when  $S = 2/5 B$ . As  $\bar{\tau}$  increases, the surface values of the source function fall slowly toward  $\sqrt{\epsilon_1} B$ . In Figure 4, we show schematically a possible case for  $\bar{\tau} \approx 0.2$ .

A third case that is relevant to the C II problem discussed in Section 6 is diagrammed in Figure 5.

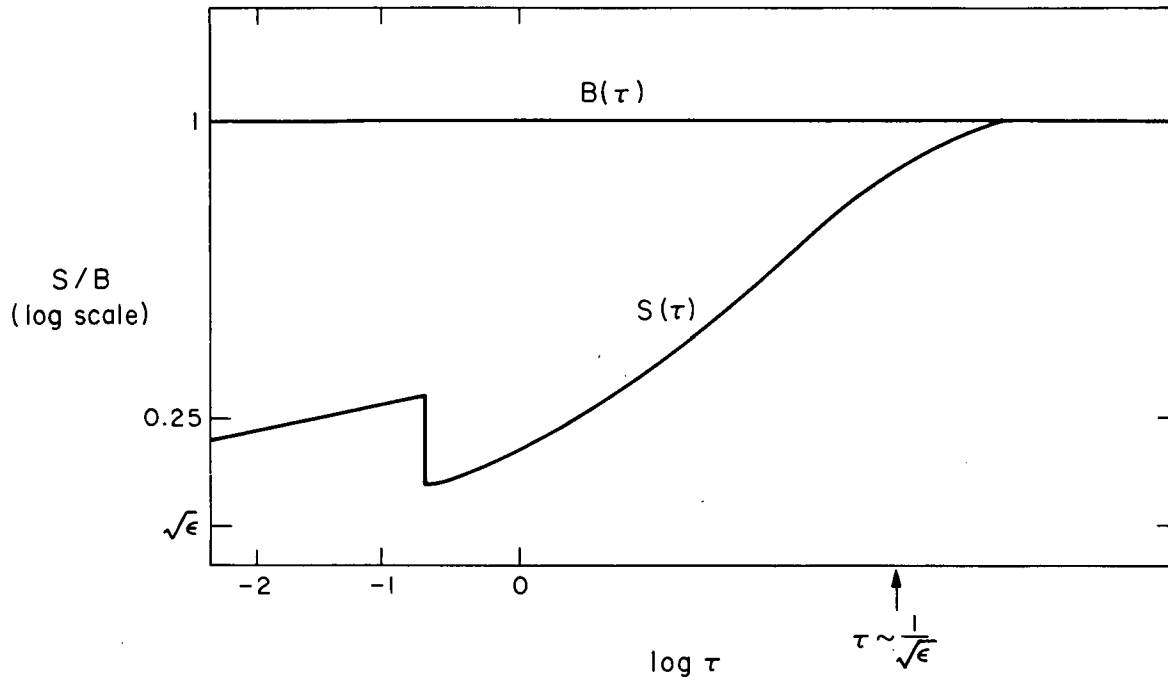


Figure 4. Source function for a turbulent surface layer.

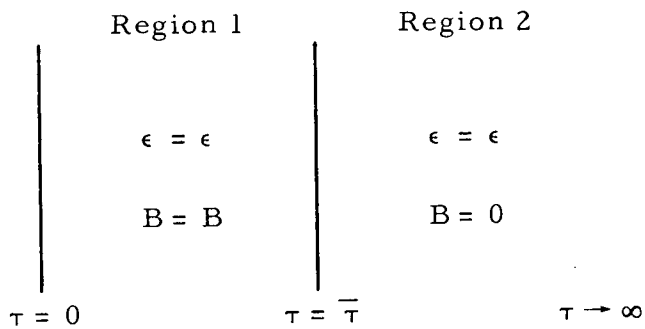


Figure 5. Diagram of hot plateau case.

We envision a hot plateau (region 1), with a much colder underlying atmosphere. The line extends across both regions, and with these boundary conditions, we have  $S \rightarrow 0$  as  $\tau \rightarrow \infty$ . Clearly, the differential equations in both regions will be

$$S'' = \epsilon S - \epsilon B \quad . \quad (112)$$

So, general solutions are

$$S_1(\tau) = A_1 e^{\sqrt{\epsilon} \tau} + C_1 e^{-\sqrt{\epsilon} \tau} + B \quad (113a)$$

and

$$S_2(\tau) = C_2 e^{-\sqrt{\epsilon} \tau} \quad . \quad (113b)$$

The integral equations for regions 1 and 2 are

$$\begin{aligned} S_1(\tau) &= A_1 e^{\sqrt{\epsilon} \tau} + C_1 e^{-\sqrt{\epsilon} \tau} + B \\ &= (1 - \epsilon) \frac{1}{2} \int_0^{\tau} e^{-(\tau-t)} (A_1 e^{\sqrt{\epsilon} t} + C_1 e^{-\sqrt{\epsilon} t} + B) dt \\ &\quad + (1 - \epsilon) \frac{1}{2} \int_{\tau}^{\bar{\tau}} e^{-(t-\tau)} (A_1 e^{\sqrt{\epsilon} t} + C_1 e^{-\sqrt{\epsilon} t} + B) dt \\ &\quad + (1 - \epsilon) \frac{1}{2} \int_{\tau}^{\infty} e^{-(t-\tau)} C_2 e^{-\sqrt{\epsilon} t} dt + \epsilon B \quad , \end{aligned} \quad (114a)$$

and

$$\begin{aligned} S_2(\tau) &= C_2 e^{-\sqrt{\epsilon} \tau} = (1 - \epsilon) \frac{1}{2} \int_0^{\bar{\tau}} e^{-(\tau-t)} (A_1 e^{\sqrt{\epsilon} t} + C_1 e^{-\sqrt{\epsilon} t} + B) dt \\ &\quad + (1 - \epsilon) \frac{1}{2} \int_{\tau}^{\bar{\tau}} e^{-(\tau-t)} C_2 e^{-\sqrt{\epsilon} t} dt \\ &\quad + (1 - \epsilon) \frac{1}{2} \int_{\tau}^{\infty} e^{-(t-\tau)} C_2 e^{-\sqrt{\epsilon} t} dt \quad , \end{aligned} \quad (114b)$$

which yield the equations

$$0 = A_1(1 - \sqrt{\epsilon}) + C_1(1 + \sqrt{\epsilon}) + B(1 - \epsilon) \quad , \quad (115a)$$

$$0 = A_1(1 + \sqrt{\epsilon}) e^{\bar{\tau}\sqrt{\epsilon}} + C_1(1 - \sqrt{\epsilon}) e^{-\bar{\tau}\sqrt{\epsilon}} - C_2(1 - \sqrt{\epsilon}) e^{-\bar{\tau}\sqrt{\epsilon}} + B(1 - \epsilon) \quad , \quad (115b)$$

$$0 = A_1(1 - \sqrt{\epsilon}) e^{\bar{\tau}\sqrt{\epsilon}} + C_1(1 + \sqrt{\epsilon}) e^{-\bar{\tau}\sqrt{\epsilon}} - C_2(1 + \sqrt{\epsilon}) e^{-\bar{\tau}\sqrt{\epsilon}} + B(1 - \epsilon) \quad . \quad (115c)$$

By solving these equations for  $A_1$  and  $C_1$  and substituting into (113a), we have

$$S_1(\tau) = B \left[ 1 - e^{-\sqrt{\epsilon}\tau(1 - \sqrt{\epsilon})} + \frac{e^{-\sqrt{\epsilon}\tau(1 - \sqrt{\epsilon})^2} - e^{\sqrt{\epsilon}\tau(1 - \epsilon)}}{2 e^{\bar{\tau}\sqrt{\epsilon}}} \right] \quad . \quad (116)$$

It can easily be shown that as  $\bar{\tau} \rightarrow 0$ ,  $S_1(0) = \epsilon B$ , and as  $\bar{\tau} \rightarrow \infty$ ,  $S_1(0) = \sqrt{\epsilon} B$ . Note also that as  $\bar{\tau} \rightarrow \infty$ , we have  $S_1(\bar{\tau}) = 1/2 B$ . But our primary interest is in the case analogous to the C II problem, where  $\sqrt{\epsilon}\bar{\tau} \ll 1$ . This is commonly called the "effectively optically thin" case. If we then expand the source-function expression for small  $\tau$  and small  $\bar{\tau}$ , we obtain to lowest order

$$S_1(\tau) = \epsilon B(1 + \bar{\tau} + \tau\bar{\tau}) \quad , \quad (117)$$

which says that over the plateau the source function rises linearly from a surface value of  $\epsilon B(1 + \bar{\tau})$  to an interior value of  $\epsilon B(1 + \bar{\tau} + \bar{\tau}^2)$ . For  $\sqrt{\epsilon}\bar{\tau} \ll 1$ , the maximum in the source function occurs at the interior edge of the hot plateau, but for  $\sqrt{\epsilon}\bar{\tau} \geq 1$ , the source function will reach its maximum near  $\bar{\tau}/2$  and decline both inward and outward. In Figure 6, we plot schematically the form of the source function and Planck function curves for plateaus that are effectively optically thin (case 1) and effectively optically thick (case 2).

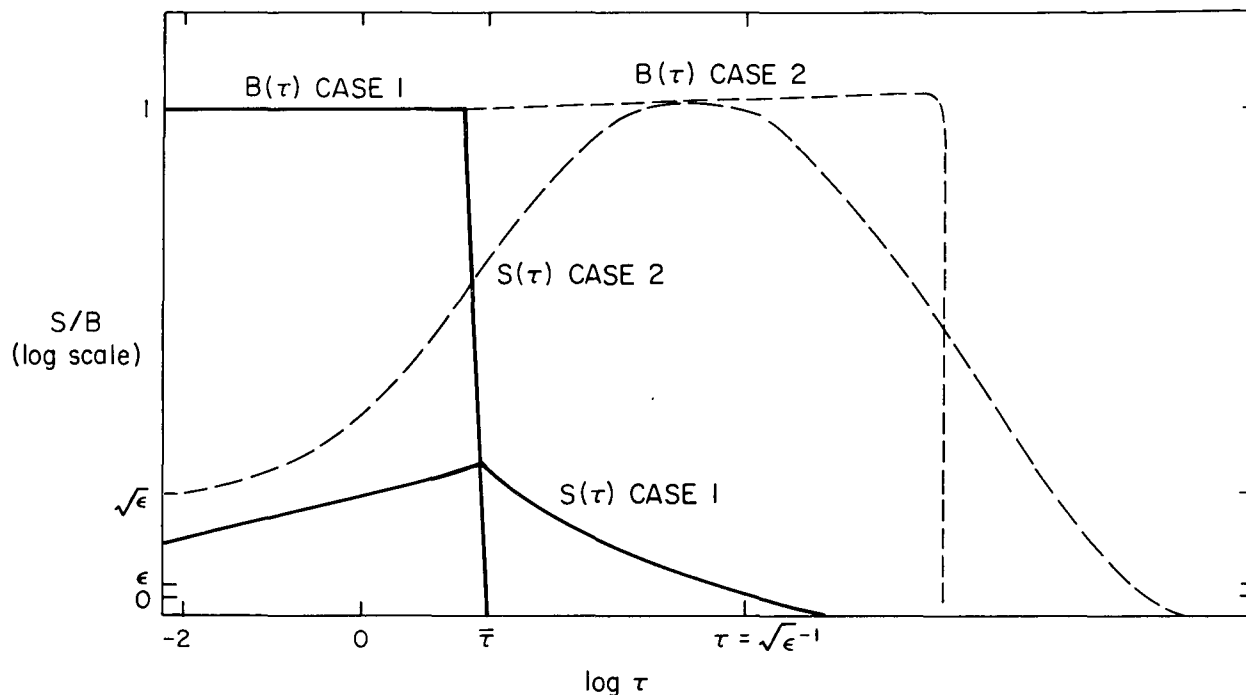


Figure 6. Source functions for two plateau cases.

A last example, somewhat simpler than the preceding, is the case of the radiating finite slab. This case differs from the one just covered in that the atmosphere does not extend below the plateau, so the total optical depth is finite. This case applies to most of the ultraviolet emission lines in the sun, although most of them are so optically thin that the radiative-transfer problem is of little interest. A few lines, like the resonance line of C III, have optical depths of order unity, so it is this sort of line that we are considering here.

We will derive the usual differential equation (112), with the solution as in (113a). However, if we look at the symmetry of the problem, it is apparent that a simpler solution will be of the form

$$S(\tau) = A \left[ e^{\sqrt{\epsilon} \tau} + e^{\sqrt{\epsilon} (\bar{\tau} - \tau)} \right] + B \quad , \quad (118)$$

where  $\bar{\tau}$  is the total optical thickness of the slab. The usual method of solution yields the answer

$$S(\tau) = B \left\{ 1 - \frac{(1 - \epsilon) [e^{\sqrt{\epsilon} \tau} + e^{\sqrt{\epsilon}(\bar{\tau} - \tau)}]}{e^{\bar{\tau} \sqrt{\epsilon}}(1 + \sqrt{\epsilon}) + (1 - \sqrt{\epsilon})} \right\}, \quad (119)$$

which can be shown to have the correct asymptotic properties. If we assume  $\bar{\tau} \sqrt{\epsilon} \ll 1$ , we can reduce (119) to

$$S(\tau) = \epsilon B \left[ \frac{2 + \bar{\tau} - \tau^2 + \tau \bar{\tau} + \sqrt{\epsilon} \left( \bar{\tau} + \frac{1}{2} \tau^2 \right)}{2 + \bar{\tau} \sqrt{\epsilon}} \right] \quad (120)$$

or

$$S(\tau) = \epsilon B \left( 1 + \frac{1}{2} \bar{\tau} - \frac{1}{2} \tau^2 + \frac{1}{2} \tau \bar{\tau} \right). \quad (121)$$

Thus, the source function has minima of  $S = \epsilon B(1 + 1/2 \bar{\tau})$  at  $\tau = 0$  and  $\tau = \bar{\tau}$  and has a rounded maximum in the center of the slab with a value

$$S(\bar{\tau}/2) = \epsilon B \left( 1 + \frac{1}{2} \bar{\tau} + \frac{1}{8} \bar{\tau}^2 \right). \quad (122)$$

These examples should be helpful in analyzing the results of the more exact calculations in later sections. Many of the approximations derived in this section are obeyed surprisingly well by detailed computations.

## 2. ATMOSPHERES

For the most part, we will discuss the details of various models of the solar atmosphere in Sections 4 through 7, where we consider the individual lines. However, it will be found useful to compare some current models outside the context of any particular line, so we shall give here a brief summary of several of the most widely used atmospheric models. We will consider only one-component atmospheres, in spite of the fact that a considerable amount of recent work has been done interpreting line profiles in terms of two-component atmospheres (see, for example, Beebe and Johnson, 1969; Beebe, 1971). We believe that at present most observations do not justify the necessity of interpreting lines in terms of two-component atmospheres. These two-component atmospheres have been devised solely to explain the center-to-limb behavior of the H and K lines of ionized calcium, and it appears unlikely that some of the grossly nonhomogeneous models could satisfactorily reproduce the observed continuum intensities in both the infrared and the ultraviolet, in view of the linear dependence of emission upon temperature in the infrared, and the highly nonlinear relation of these two quantities in the ultraviolet, and in view of the success of one-component models in reproducing both infrared and ultraviolet intensities. In the Appendix, we show that the basic features of even the calcium K line profiles can be explained by a one-component model atmosphere.

All the models described here, with the exception of some of those of Athay and his collaborators, are empirical models in hydrostatic equilibrium. The temperature, pressure, physical height, and, possibly, other parameters are tabulated as functions of some independent variable, usually optical depth at 5000 Å. Hydrostatic equilibrium is assumed, so specifying the values of one variable such as temperature is sufficient to determine the entire atmosphere. Radiative equilibrium is not assumed, although sometimes theoretical radiative equilibrium atmospheres are used as a guide in deeper layers. In the models of Athay (1969), of Athay and Canfield (1970),

and of Linsky and Avrett (1970), an artificial pressure, due to turbulent motions, is added to the usual thermal pressure in the equation of hydrostatic equilibrium.

In this and later sections, we shall generally plot the parameters of model atmospheres as functions of physical height. While it is undoubtedly true that for many purposes optical depth is a more useful independent variable, no one wavelength at which the optical depth is to be defined can be optimally useful over the full height range of an atmosphere. As far upward as the temperature minimum, a wavelength of 5000 Å is satisfactory, but in the low chromosphere, a wavelength at the head of the Lyman continuum is better, since electron scattering affects  $\lambda$  5000 optical depths but does not much affect the overall structure of the atmosphere. At temperatures high enough that hydrogen becomes significantly ionized, both optical depth and height scales are strongly influenced by details of the non-LTE ionization equilibrium of hydrogen, so neither is appreciably more useful than the other. The input of PANDORA uses height as the independent variable for all atmospheric parameters.

One point that should be mentioned in this connection is that the transformation from optical depth to height depends on the assumed He/H ratio, which is poorly defined by observations. The Utrecht Reference Photosphere (see below) used a ratio of 0.20 by number, whereas the Bilderberg Continuum Atmosphere (BCA) and almost all more recent models, and also the earlier model of Thomas and Athay (1961), assume 0.10. Helium acts as an inert gas, which increases pressures, and thus can change the relation between optical depth and physical height.

Many models have been constructed of the photosphere, or that portion of the solar atmosphere below the temperature minimum. We might mention the work of Minnaert (1953) and Böhm-Vitense (1954). In 1955, Athay, Menzel, Pecker, and Thomas (1955) derived an empirical model of the solar chromosphere, based on calibrated eclipse spectra. This material was used again in an improved model by Thomas and Athay (1961); their derived temperature distribution and electron density are shown in Figure 7 along with two others discussed below. The lower portion of Thomas and Athay's model

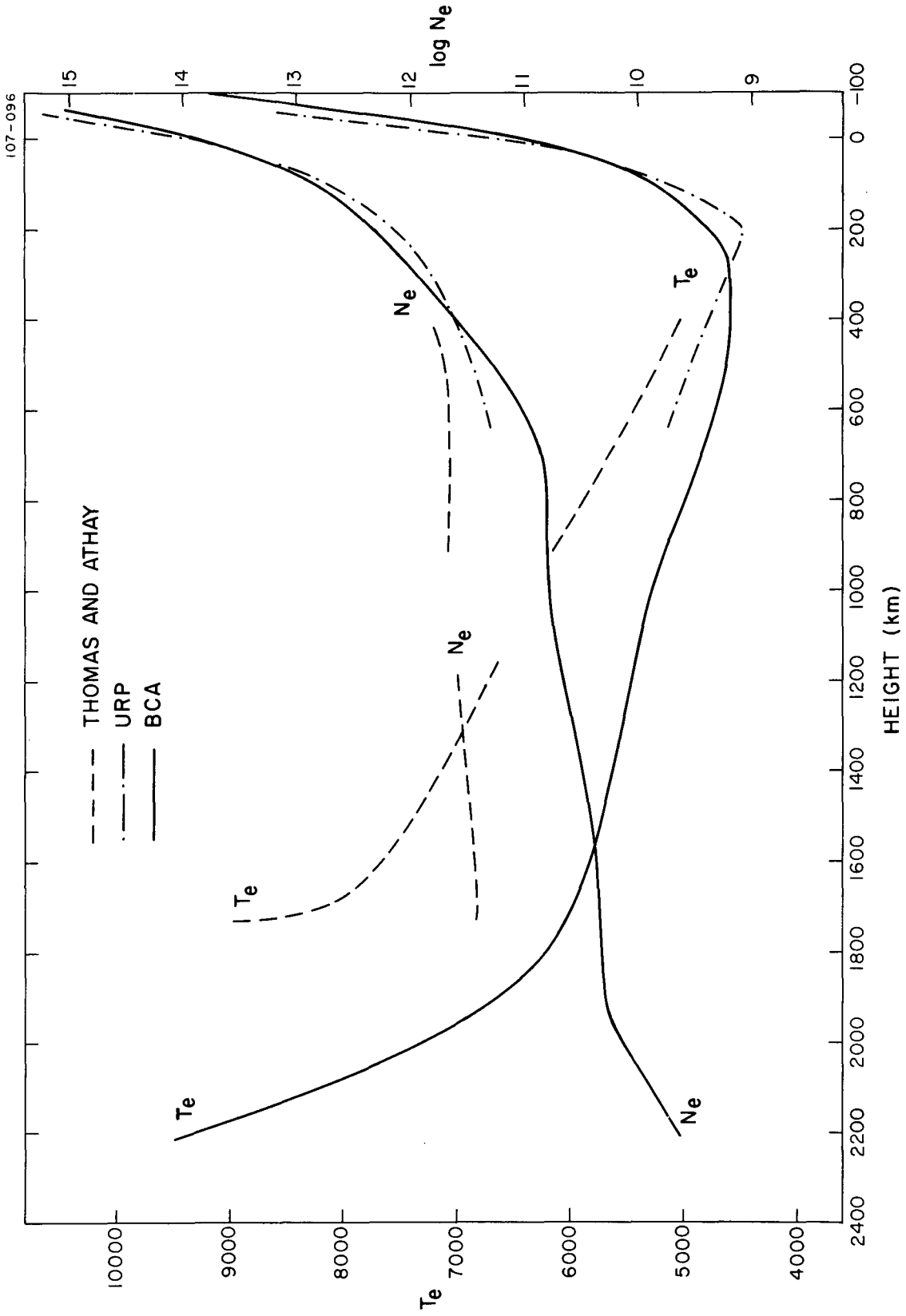


Figure 7. Temperatures and electron densities for three model atmospheres.

atmosphere is an observational upper bound on the temperature, and the zero point of their height scale has been adjusted following Thomas and Gebbie (1971). The analysis utilizes measured intensities, at a series of heights in the chromosphere, at  $\lambda 4700$  and at the head of the Balmer continuum, and hydrostatic equilibrium is assumed through the chromosphere. One can then derive the temperature, and electron and neutral hydrogen density as a function of height. Pottasch and Thomas (1960) have also calculated theoretically the non-LTE formation of the Lyman continuum, with a resulting model similar to that of Thomas and Athay (1961).

A series of models of the solar atmosphere constructed explicitly in hydrostatic equilibrium all the way from the photosphere through the temperature-minimum region to the chromosphere began with the Utrecht Reference Photosphere (URP) (Heintze, Hubenet, and de Jager, 1964). This model had a temperature minimum of  $4500^\circ$ , located at an optical depth  $\tau_{5000} = 0.02$  at a height of 200 km above  $\tau_{5000} = 1.0$ . In Figure 7, we show the temperature and electron density vs. height relations for this model. Soon after the publication of the URP, it became evident that the new ultraviolet and especially infrared data implied that the temperature minimum is at a much smaller optical depth than 0.02. An atmosphere incorporating the new ideas was devised at the Bilderberg Conference in April 1967 and published under the name of the Bilderberg Continuum Atmosphere (see Gingerich and de Jager, 1968). The BCA includes a chromosphere extending up to 2210 km and to a temperature of  $9500^\circ$  as opposed to 635 km and  $5125^\circ$  for the URP, which gives some indication of the large amount of new data that had accumulated in the interim. More importantly, the BCA has a very broad temperature minimum of  $4600^\circ$ , extending from 295 to 440 km, corresponding to an optical-depth range of  $6 \times 10^{-3}$  to  $6 \times 10^{-4}$ . But while the BCA had the best model chromosphere up to that time (in fitting new infrared data), it was somewhat cruder than necessary in its treatment of the photosphere. It does not represent the visible and near-infrared limb darkening well. A revision of the BCA that is better in this respect was published at the same time by Elste (1968). In Figure 7, we show also the temperature-height and electron-density-height relations of the BCA. Elste tabulates his model as a function of optical depth, so it cannot be readily included on this figure.

After the BCA was published, new observations in the far infrared and in the ultraviolet led to changes in the accepted temperature-minimum value. For many years, it had been known that the  $K_1$  minimum of the K line has a brightness temperature of at most  $4400^\circ$ , while continuum observations implied a temperature minimum of  $4600^\circ$ . This discrepancy was usually attributed to the effects of inhomogeneities on the K-line profiles. However, the observations of Mankin and Strong (1969), Eddy, Léna, and MacQueen (1969), and Parkinson and Reeves (1969, 1970) definitely indicated a lower value of the temperature minimum. And on the basis of theoretical calculations, Athay (1970) showed that the boundary temperature of a non-LTE line-blanketed solar model in radiative equilibrium will be  $4330^\circ \pm 150^\circ \text{ K}$ .

In response to these developments an atmosphere with a temperature minimum of  $4200^\circ$ , called the SAO5 Atmosphere, was distributed by Gingerich (1970). This atmosphere also corrected the deficiencies of the BCA model in the photosphere. The SAO5 Atmosphere has a smoothly sloping temperature, falling from  $4600^\circ$  at  $\tau_{5000} = 10^{-2}$  to  $4200^\circ$  at  $\tau_{5000} = 10^{-4}$ , with a height at the temperature minimum of 550 km. Above the temperature minimum, the temperature rises rather rapidly to  $10,000^\circ$  and above.

Linsky and Avrett (1970) derived a model of the solar chromosphere based on their study of the formation of the Ca II H and K lines. In their calculations, Linsky and Avrett have included a turbulent pressure due to microturbulent gas motions, so their model atmosphere is somewhat more extended in height than are most other recent models.

Finally, the most recent atmosphere of this particular type is the Harvard-Smithsonian Reference Atmosphere (HSRA) (Gingerich, Noyes, Kalkofen, and Cuny, 1971). The HSRA differs from the SAO5 only in the upper chromosphere. In this region, the HSRA includes the results of non-LTE analyses of the formation of the Lyman continuum (Noyes and Kalkofen, 1970). The HSRA extends up to a temperature of  $8930^\circ$ , at a height of 1860 km. The total pressure at the highest point is  $0.15 \text{ dyne cm}^{-2}$ , which is within the usually quoted range for the pressure at the base of the corona, of 0.1 to  $0.2 \text{ dyne cm}^{-2}$ . In Figure 8, we plot the temperature-height relation of the BCA, SAO5, Linsky and Avrett, and HSRA atmospheres, taken partially from Gingerich *et al.*

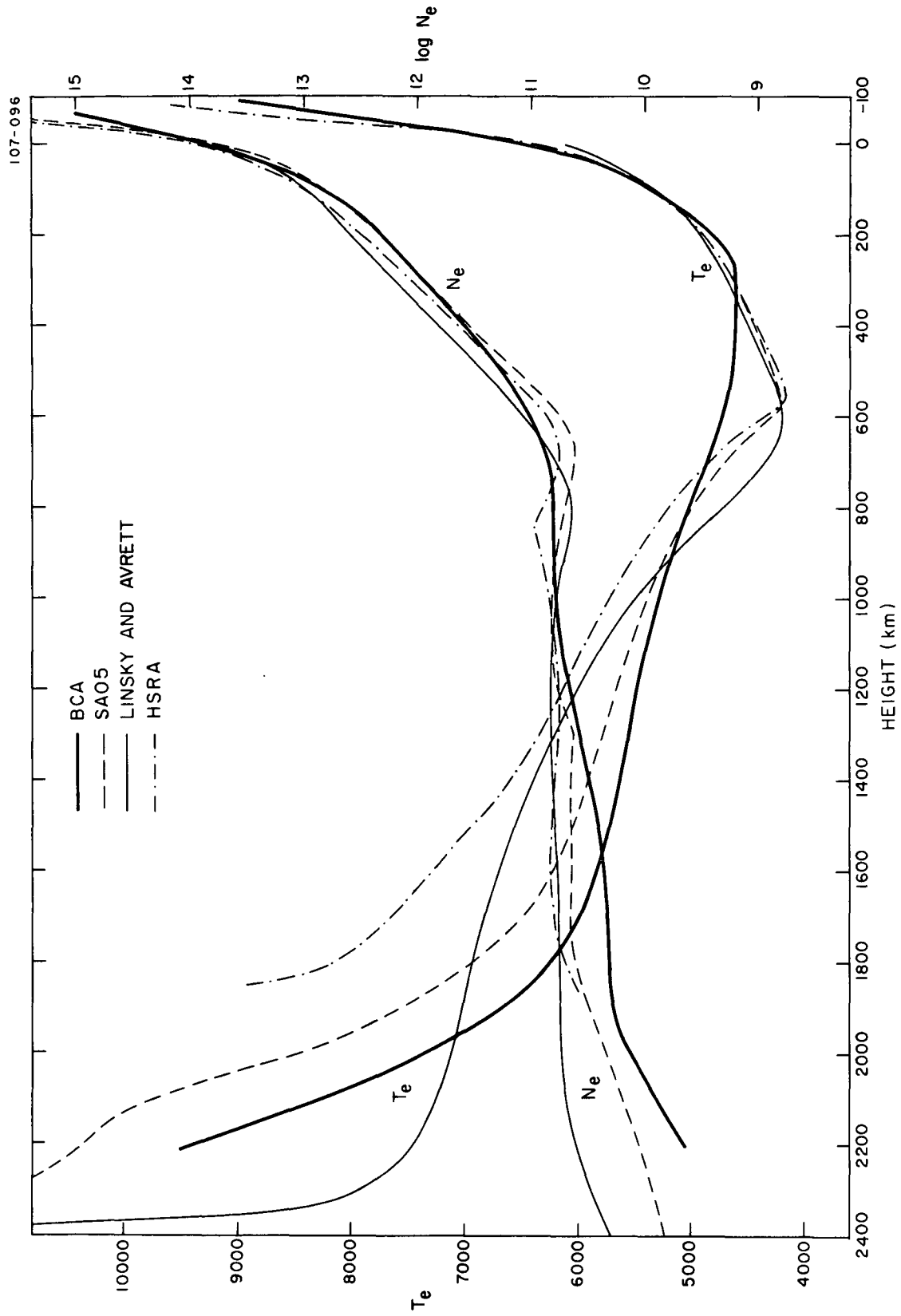


Figure 8. Temperatures and electron densities for four model atmospheres.

(1971). In the photosphere, the temperatures of the SAO5 and HSRA models are indistinguishable.

It is interesting to note, as pointed out by Thomas and Gebbie (1971), that the temperature structures of the models since the BCA have been approaching closer and closer to the early empirical model of Thomas and Athay (1961). Nevertheless, the chromospheric electron density of the HSRA is still a factor of about four smaller than that of the Thomas and Athay model.

As has been pointed out several times (cf. Athay and Canfield, 1969), the intensities in the centers of many strong solar lines could be more easily explained if the region of formation of the line had a greater electron density than is implied by the series of models discussed above. Athay and his collaborators have postulated that turbulence in the solar atmosphere might produce an additional source of pressure, besides the usual thermal pressure. If we include this pressure source, it is possible to produce model atmospheres in hydrostatic equilibrium, which have appreciably greater densities and electron densities in the upper chromosphere than do the BCA and its successors.

In their paper on the Na I and Mg I lines, Athay and Canfield (1969) did not construct a detailed hydrostatic equilibrium atmosphere but merely postulated an electron density rather larger than that given by the BCA. In Figure 9, we show both the temperature and the electron densities for the BCA and for the atmosphere of Athay and Canfield (1969). In the region between  $\tau_{5000} = 10^{-1}$  and  $\tau_{5000} = 10^{-5}$ , the two atmospheres have the same total hydrogen density, but the atmosphere of Athay and Canfield has a considerably higher electron density, greater by approximately a factor of five over most of this region. This difference enabled Athay and Canfield to derive theoretical line profiles that agree well with the observed profiles for Na I and Mg I, at least for the center of the solar disk.

More recently, Athay (1969) has published two model solar atmospheres, one of which includes a turbulent-pressure term. The theory of support of the chromosphere by means of pressure due to turbulent motions in the atmosphere was first put forth by McCrea (1929) and has been considered by many authors since that time. Athay's models include a solution of the non-LTE

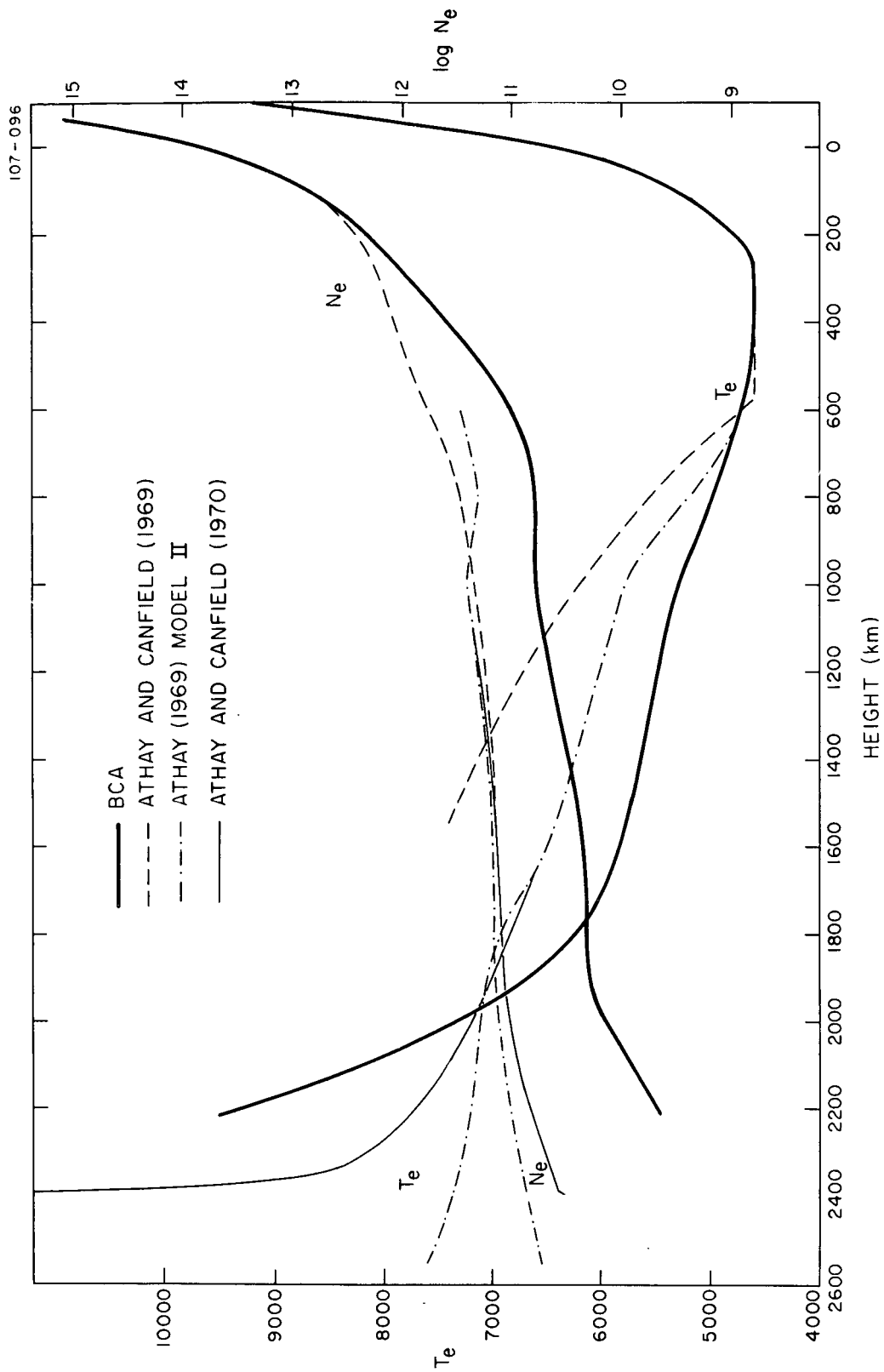


Figure 9. Temperatures and electron densities for four models.

Lyman-continuum transfer problem, but the Lyman- $\alpha$  line in the two-level model hydrogen atom was taken to be in radiative detailed balance. These models are required to fit certain observational constraints, such as the intensity of the Balmer continuum during eclipse, the pressure at the base of the corona, and the Lyman continuum intensity at the solar-disk center. We show Athay's model II, which includes turbulent pressure, in Figure 9. Once again the electron density is everywhere higher than that of the BCA model. Note also that Athay's model has a narrow temperature-minimum region, with a rather higher minimum-temperature value than is assumed in the SAO5 and HSRA atmospheres. Inclusion of a minimum temperature as low as  $4200^\circ$  would reduce all Athay's electron densities. Another model, which we have plotted as Athay and Canfield (1970), was published in connection with a study of the resonance lines of O I. The method and constraints are essentially the same as for Athay's model II discussed above.

It would appear that indeed some nonthermal pressure source does act in the solar atmosphere, but Athay's models do not agree with the latest observations relevant to the temperature-minimum region, and so must be revised. Whether deviations from spherical symmetry in the low chromosphere are small enough that eclipse Balmer continuum emission data are useful in constructing average atmospheres is an unresolved question at the moment. Certainly, it is difficult to construct atmospheres satisfying the eclipse observations.

Almost all the above model chromospheres extend not far beyond  $9000^\circ$ , if that far. This is largely because the Lyman continuum is formed at an electron temperature of approximately  $8500^\circ$ , and the Lyman continuum is formed higher than any other continuum region usually used in atmosphere construction. Conversely, most of the ultraviolet emission lines can be used to derive models of the high-temperature regions of the solar atmosphere, but these models only represent the observations well at temperatures of  $100,000^\circ$  and above (see Dupree and Goldberg, 1967), where the hypothesis of constant conductive flux is valid. Between  $9000$  and  $100,000^\circ$ , radio observations are the only useful continuum intensities, and line observations are not so easy to interpret in this temperature range as above  $100,000^\circ$  since many of the strong lines cannot be assumed to be optically thin. Consequently, few

quantitative models of this region of the solar atmosphere have been published. We will review some of the relevant studies.

Thomas and Athay (1961) pointed out that we should expect one or more temperature plateaus in the high chromosphere, with abrupt changes in temperature between plateaus. These authors placed the plateau associated with H I emission at close to  $11,000^\circ$  and concluded that the He I and He II plateaus might merge at approximately  $60,000^\circ$ . In general, however, their temperature values were rather tentative, and lengthy detailed calculations, such as those reported by Field (1965) and by Defouw (1970), are required to obtain accurate values for the temperature plateaus. Thomas and Athay do not propose a quantitative temperature-height relation for such plateau regions.

It now appears that the region in which the Lyman continuum is formed should be identified with the hydrogen temperature plateau, although it might be that separate plateaus exist, which are associated with hydrogen continuum and line emissions. Observations imply that the Lyman-continuum formation region breaks off with an abrupt temperature rise from  $9000$  to over  $12,000^\circ$  at least. Beyond this there does not seem to be any published indication of observational evidence in favor of any other temperature plateaus. We study this question further in later sections.

Pottasch (1964) quotes an atmosphere from  $10,000$  to  $1,600,000^\circ$  derived from ultraviolet line intensities by Kanno and Tominaga. A value of the product  $N_e T_e = 7 \times 10^{14}$  was assumed, and a thickness of  $17.4$  km in the temperature range  $10,000$  to  $100,000^\circ$  was derived. In Figure 10, we plot this model along with two others mentioned below. We have multiplied the heights by a correction factor to take into account the different electron pressure from that adopted by Athay (1966), who chose  $N_e T_e = 6 \times 10^{14}$ . Athay (1966) made a very careful analysis of the ultraviolet line emission and derived a model from which we have plotted in Figure 10 a curve based on his two lowest points. We have also plotted a curve based on the highest few points of the atmosphere tabulated by Athay and Canfield (1970), based on their study of the O I ultraviolet resonance lines. These atmospheres, which we have plotted, show no evidence of any temperature plateau and give only an order-of-magnitude idea of the physical thickness of the solar atmosphere between  $10,000$  and  $100,000^\circ$ . We can probably do no better than this without

performing detailed calculations for individual lines, taking into account radiative-transfer effects and density-dependent ionization equilibrium effects. This fact is apparent from an inspection of Athay's (1966) Figure 3 and of Dupree and Goldberg's (1967) Figure 3, where for temperatures around  $60,000^\circ$ , we find points differing from one another by almost two orders of magnitude.

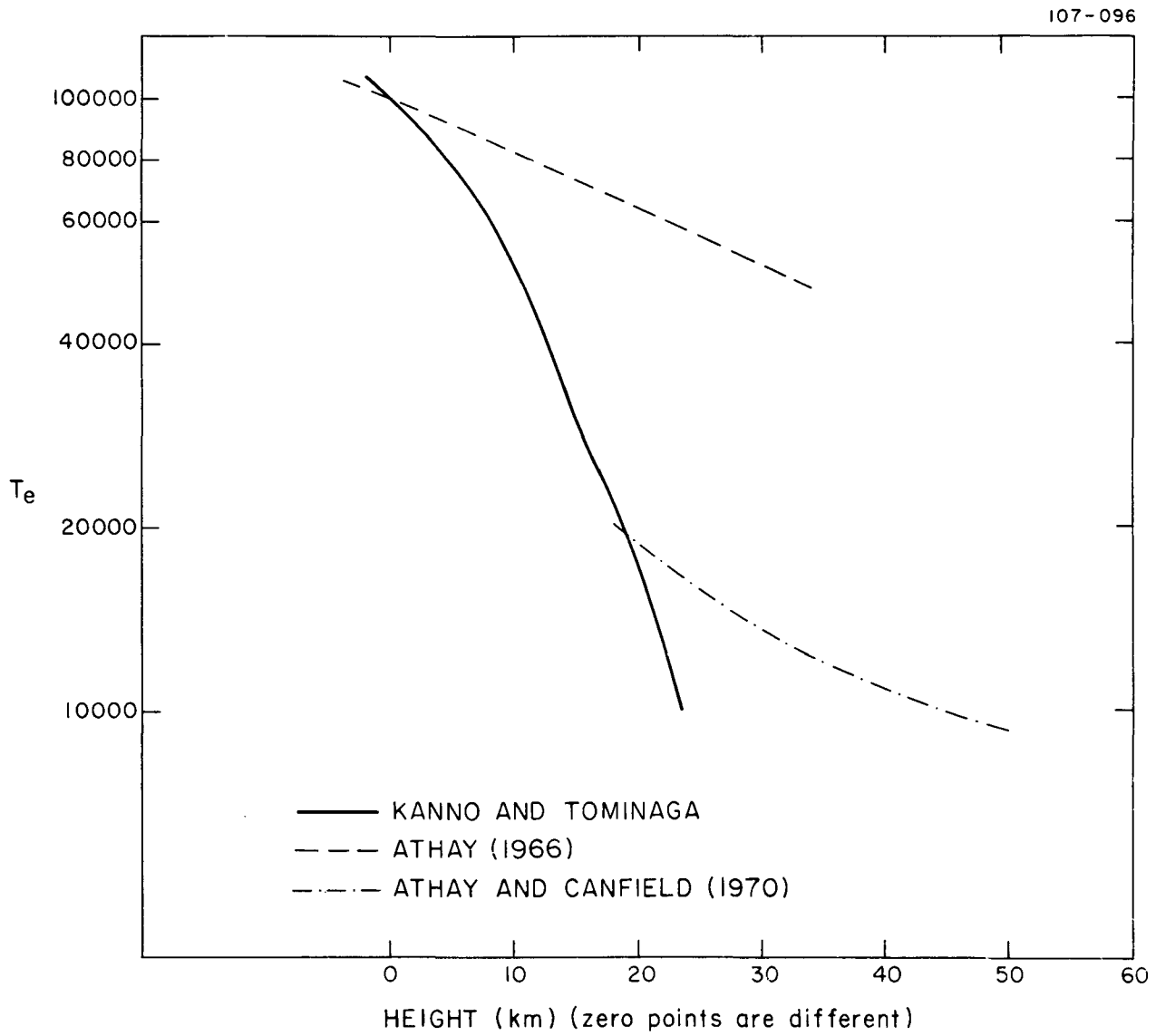


Figure 10. Models of the upper chromosphere.

In our final few sections, we study in detail several lines formed completely or partially in the temperature region 10,000 to 100,000°. In view of the problems mentioned in connection with the methods of Athay and of Dupree and Goldberg, we may not be justified in making firm conclusions based on the lines of only two or three ions. A completely satisfactory study should treat about four stages of ionization of at least three ions and would be very time-consuming. In this work, we make a start in this direction.

### 3. ATOMIC PARAMETERS

In the sections dealing with individual lines, we will present most of the data on atoms and ions, but it will be advantageous to outline here some basic points. We will discuss the way in which the various atomic quantities are input into PANDORA as well as some general formulas and large tabulations of data, which are useful in relation to many atomic species.

#### 3.1 Abundances

First, let us consider the question of the elemental abundances to be used. We have in each case used the photospheric abundances of Goldberg, Müller, and Aller (1960). These abundances have been changed only by small amounts by more recent work, except for the case of iron. Since we do not discuss any iron lines, we can reasonably use GMA abundances for all our lines. There has been some uncertainty as to whether photospheric, chromospheric, and coronal abundances are truly identical for all elements or whether significant variations exist for some elements; but no definite evidence of abundance variations exists hitherto, so we have used photospheric abundances in analyzing lines that are formed in the chromosphere or chromosphere-corona transition region. In PANDORA, we specify the abundances relative to the total hydrogen density, as is conventional.

#### 3.2 Radiative Bound-Bound Rates

Our radiative transition rates have been obtained from a number of different sources, both experimental and theoretical. In general, experimental values have been preferred over theoretical ones. For Mg II, we adopted values from Corliss and Bozman (1962), who used a wall-stabilized arc in their A-value determinations. For O I and C II, there are available experimental A-value determinations by the phase-shift method, by Parkes, Keyser, and Kaufman (1967) for O I and by Lawrence and Savage (1966) for C II. This

method offers the possibility of great accuracy in A-value determinations in comparison with other methods using arcs, furnaces, or shock tubes. We found the National Bureau of Standards compilations of theoretical results by Wiese, Smith, and Glennon (1966) and by Wiese, Smith, and Miles (1969) useful for comparison with experimental results in the above cases. For the case of C III, since we could find no experimental work, we have used the A values given by Wiese et al. (1966) for the two strong lines, and that computed by Garstang and Shamey (1967) for the intercombination line.

### 3.3 Radiative Bound-Free Rates

A few of the bound-free continuum cross sections have been measured experimentally, but usually we must use theoretical results. One useful list of cross sections is that of Henry (1970), who used Hartree-Fock wavefunctions for the ground configuration states and close-coupled wavefunctions for the continuum states of several abundant atoms and ions. We employed his data for the carbon ion continua, as discussed in Sections 6 and 7. In several other cases, we have used cross sections derived by using the general formula based on the quantum defect method of Burgess and Seaton (1960) as revised by Peach (1967). For situations where the phase factors appearing in the formulas of the quantum defect method are not close to zero, the accuracy of this method should be within approximately a factor of two.

PANDORA allows a variety of forms in which we can specify the photoionization rates in each continuum. If we know in advance the numerical values of the photoionization rate and photorecombination rate in a given continuum at each depth point in the atmosphere, we can input these rates explicitly. Alternatively, we can specify the photoionization cross section at one or more frequency points in the continuum. PANDORA will interpolate linearly to determine the cross section between frequency points up to the last, highest frequency point, and from this point on a  $\nu^{-3}$  frequency dependence of the cross section is assumed. Then we must determine the radiation field in the continuum. Once again we have two alternatives: We can specify

a "radiation temperature" for each photoionization continuum at each depth point in the atmosphere, in which case, a blackbody radiation field is assumed and the integration of intensity times cross section over frequency is performed automatically; or, if we so desire, PANDORA will internally compute the radiation field at each of the specified frequency points for each depth in the atmosphere. In so doing, the radiative-transfer equation must be solved for each frequency point, since we include pure scattering by electrons and Rayleigh scattering, pure absorption in LTE by the important metals, and non-LTE absorption by hydrogen and by certain metals (e. g., neutral carbon). For the computation of the non-LTE continuum opacity due to hydrogen, we must in general input the densities at each depth point of neutral hydrogen, protons, electrons, and of neutral hydrogen in the  $n=2$  level, plus possibly other higher levels. After computing the radiation field at each frequency point, the integration of intensity times cross section is performed as before, with the assumption that the radiation temperature remains constant between the highest specified frequency point and infinite frequency.

Depending on the individual situations, we use all these various input possibilities. Internal computation of intensities requires a considerable amount of computer time, and beyond the Lyman continuum, that is, shortward of approximately  $\lambda 500$ , the opacity sources that are taken into account are insufficient (as of this writing the He I opacity has not been added). In some cases, we can perform the photoionization computations once and input the rates explicitly for other cases with the same atom and only slightly different atmospheres. For continua that fall at short wavelengths, we simply specify the radiation temperatures, based on published data on ultraviolet intensities.

### 3.4 Collisional Bound-Bound Rates

Probably the most uncertain, and often the most important, atomic parameters are the collisional bound-bound rates, or equivalently, the collisional excitation cross sections. Experimental results relevant to these cross sections are rare, so we are generally forced to use theoretical calculations,

or even approximate general formulas. For allowed transitions, Van Regemorter (1962) has derived a general formula for the calculation of approximate collisional transition rates. He expresses the deexcitation rate from level  $j$  to level  $i$  as

$$C_{ji} = 20.6 \lambda^3 N_e T_e^{-1/2} A_{ji} P\left(\frac{E_{ij}}{kT_e}\right) , \quad (123)$$

with  $\lambda$  expressed in centimeters. The quantity  $P(E_{ij}/kT_e)$  is a tabulated function, equal to the averaged Gaunt factor  $\bar{g}$  used by Seaton (1964). The corresponding excitation rate is

$$C_{ij} = 13.7 \lambda N_e T_e^{-1/2} f_{ij} P\left(\frac{E_{ij}}{kT_e}\right) \exp\left(-\frac{E_{ij}}{kT_e}\right) . \quad (124)$$

This formula must be used with care, however. Blaha (1968, 1969) has found that for highly ionized ions the Gaunt factors are 0.4 to 0.6 or even higher, rather than the value of 0.2 given by Van Regemorter's table of  $P(E_{ij}/kT_e)$ . In addition, for neutral atoms at large values of  $E_{ij}/kT_e$ , Van Regemorter's formula gives rates that are extremely low — probably unrealistically so. We discuss this point in the section on O I.

For purposes of comparison with the results of other workers, such as Athay and Canfield (1969, 1970), we would like to know how to convert from excitation cross sections, taken as constant above threshold, to rates given by equation (124). To do this, we express the excitation rate as

$$C_{ij} = \int_{v=v_{\min}}^{\infty} Q_{ij} \pi a_0^2 N_e(v) v dv , \quad (125)$$

where  $Q_{ij}$  is the excitation cross section in units of the Bohr cross section. We equate expressions (124) and (125), using the known Maxwellian distribution of electron velocities, to obtain

$$Q_{ij} = 2.51 \times 10^{11} \frac{\lambda P \left( \frac{E_{ij}}{kT_e} \right) f_{ij}}{T_e \left[ \left( \frac{E_{ij}}{kT_e} \right) + 1 \right]} . \quad (126)$$

In PANDORA, collisional excitation rates are expressed in terms of a parameter  $CE_{ij}$ , by the formula (for excitation)

$$C_{ij} = CE_{ij}(T_e) N_e \exp\left(-\frac{E_{ij}}{kT_e}\right) . \quad (127)$$

For each transition, we input a table of values of  $CE$ , corresponding to a preset table of temperatures. Subsequently, at each atmosphere point PANDORA linearly interpolates in the table of  $CE$  values to derive a value for the temperature at that atmosphere point.

To convert between cross sections expressed in terms of  $Q_{ij}$ , the  $CE_{ij}$ 's and equation (124), we can use

$$CE_{ij} = 5.45 \times 10^{-11} Q_{ij} T_e^{1/2} \left[ \left( \frac{E_{ij}}{kT_e} \right) + 1 \right] \quad (128)$$

and

$$CE_{ij} = 13.7 \lambda P \left( \frac{E_{ij}}{kT_e} \right) f_{ij} T_e^{-1/2} . \quad (129)$$

If we input negative  $CE$ 's, PANDORA will insert the number density of neutral hydrogen, rather than the electron density, in equation (127). This is usually useful for fine-structure transitions in ions that produce lines formed in the photosphere and the low chromosphere. For cases where excitation by electrons, hydrogen atoms, and protons are all important in different parts of the atmosphere, we compute the rates in advance and then adjust the  $CE_{ij}(T_e)$  table to yield the correct rates, using either  $n_e$  or  $n_{HI}$  as a factor.

Several calculations of individual collisional cross sections have been published and are discussed in later sections. Bahcall and Wolf (1968) have

published a rather extensive treatment of fine-structure transitions, which includes general methods of computing rates for excitation by protons and hydrogen-atom collisions.

### 3.5 Collisional Ionization Rates

Collisional ionization rates are important in determining the ionization equilibria for atoms and ions of interest. Experimental measurements of collisional ionization cross sections are rare, and detailed calculations for individual ions have been done for very few cases. On the other hand, it is sometimes claimed that general formulas are more accurate for collisional ionization rates than for any other atomic process and that an error of a factor of two is unlikely. We have used extensively the formula of House (1964), based on work of Allen (1961):

$$C_{J, J+1} = 1.15 \times 10^{-8} \left( 3.1 - \frac{1.2}{Z_J} - \frac{0.9}{Z_J^2} \right) \frac{\zeta_J^{1/2} T_e^{1/2} N_e}{\chi_J^2} \exp\left(-\frac{\chi_J}{kT_e}\right) \quad (130)$$

where

$\chi_J$  = ionization potential in ev,

$\zeta_J$  = number of electrons in the outer shell, and

$Z_J$  = ionic charge after ionization.

The input of PANDORA for collisional ionization rates is similar to that for collisional excitation. The rates are expressed in terms of a parameter  $CI_{JK}(T_e)$ , according to

$$C_{JK} = CI_{JK}(T_e) N_e \exp\left(-\frac{\chi_J}{kT_e}\right) \quad (131)$$

The CI's are tabulated for a preset list of temperatures, and, unlike the case for excitation, only positive CI's, corresponding to ionization by electron collision, are allowed.

### 3.6 Broadening Constants

The absorption profile of a line subject to Doppler broadening as well as to radiative, Stark, and Van der Waals damping is given by the previously mentioned Voigt profile:

$$\phi_x(\tau) = \frac{a(\tau)}{\pi^{3/2}} \int_{-\infty}^{+\infty} \frac{e^{-z^2} dz}{[a(\tau)]^2 + \left[ z - \frac{\langle \Delta\nu_D \rangle x}{\Delta\nu_D(\tau)} \right]^2}, \quad (131)$$

where

$$x = \frac{\Delta\nu}{\langle \Delta\nu_{\text{Doppler}} \rangle} = \frac{\Delta\lambda}{\langle \Delta\lambda_{\text{Doppler}} \rangle}, \quad (132)$$

and

$$a = \frac{\Delta\nu_{\text{Damping}}(\tau)}{\Delta\nu_{\text{Doppler}}(\tau)} = \frac{\Delta\lambda_{\text{Damping}}(\tau)}{\Delta\lambda_{\text{Doppler}}(\tau)}. \quad (133)$$

The Doppler width is given by

$$\Delta\lambda_D = \frac{\lambda}{c} \sqrt{\frac{2kT}{M} + \xi^2}, \quad (134)$$

where

$M$  is the mass of the atom or ion, and

$\xi$  is the microturbulent velocity.

The damping is

$$\Delta\lambda_{\text{Damping}} = \Delta\lambda_{\text{Radiative}} + \Delta\lambda_{\text{Stark}} + \Delta\lambda_{\text{Van der Waals}}. \quad (135)$$

The radiative damping depends only on the sum of the Einstein A values for downward transitions from the two levels of the line. We have

$$\frac{\Delta\lambda_{\text{Rad}}}{\lambda} = \frac{\Delta\nu_{\text{Rad}}}{\nu} = \frac{\Sigma A}{4\pi\nu} \quad (136)$$

or

$$\Delta\lambda_{\text{Rad}} = \frac{\lambda^2 \Sigma A}{4\pi c} \quad (137)$$

Stark broadening is caused by collisions with electrons and will vary with depth in the atmosphere. In PANDORA, we use the expression

$$\Delta\lambda_{\text{Stark}} = \Delta\lambda_0 \left( \frac{N_e}{10^{12}} \right)^q \quad (138)$$

For each line, we specify  $\Delta\lambda_0$  and the value of  $q$  (usually 1.0) to be used in the calculation. In most cases, the Stark broadening widths were available in the tables of Griem (1964). We chose  $\Delta\lambda_0$  for an "average" temperature of formation of each of our lines and thereafter neglected the temperature dependence of  $\Delta\lambda_0$ . This is a reasonable approximation since  $\Delta\lambda_0$  is not strongly dependent on  $T_e$  and since Stark broadening is not the dominant broadening mechanism for any of our lines at any point.

The Van der Waals broadening is also treated by Griem (1964). The damping is proportional to  $N_{\text{HI}}$ ; we will compute  $\Delta\lambda_{\text{vdw}}$  for a standard value of  $10^{16} \text{ cm}^{-3}$ . Griem gives (1964, p. 100)

$$\Delta\nu_{\text{vdw}} = \pi N_{\text{HI}} \left( \frac{9\pi\hbar^5 R_a^2}{16 m_e E_p^2} \right)^{2/5} \frac{1}{\nu^{3/5}} = 5.10 \times 10^{-13} N_{\text{HI}} R_a^2 \frac{2/5}{\nu^{3/5}}, \quad (139)$$

where

$$\overline{R}_a^2 = \frac{1}{2} \frac{E_H}{E_\infty - E_a} \left[ 5 \frac{Z^2 E_H}{E_\infty - E_a} + 1 - 3l_a (l_a + 1) \right], \quad (140)$$

where

$E_H$  = the ionization potential of hydrogen,

$E_\infty$  = the ionization potential of the atom of interest,

$E_a$  = the excitation potential of the upper level of the line in question,

$l_a$  = the orbital quantum number of the upper level of the line in question,

$Z$  = the effective charge of the atom ( $Z = 1$  for a neutral atom),

and

$v$  = the thermal velocity of the perturbing hydrogen atoms, and

$E_p$  = the excitation energy of the resonance line of the perturbing atom ( $E_p = 10.2$  ev in the case of hydrogen, considered here).

As for Stark broadening, we evaluate  $\Delta\lambda_{vdw}$  at some "average" temperature and thereafter neglect the temperature dependence but not the density dependence.

In our initial calculations for each line, we used broadening constants given by the above formulas, but for some lines it was necessary to use different damping constants in order to fit the observed line wings. We generally adjusted the Van der Waals broadening constant, since this is usually the dominant source of broadening, and the theory of Van der Waals broadening is not very highly developed, so that the values given by equation (139) are at best only approximations.

## 4. THE MAGNESIUM II H AND K LINES

4.1 Introduction

The H and K lines of Mg II, which occur at  $\lambda 2795$  and  $\lambda 2802$ , are very similar in many ways to the H and K lines of Ca II, which we discuss in the Appendix. Hence, much of the work done on the Ca II lines is applicable in some degree to the Mg II lines as well. Several workers have studied the formation of the Mg II H and K lines, including most notably Dumont (1967a, b) and Athay and Skumanich (1968a). Since these workers have treated the subject in considerable detail, we do not intend to repeat very much of their work here. We plan to investigate only three points:

1. The computed Mg II H and K profiles that arise from calculations using the Harvard-Smithsonian Reference Atmosphere (Gingerich et al., 1971).

2. The effects, if any, of a chromospheric temperature plateau, such as we discuss in Sections 5 and 6, upon the Mg II line profiles.

3. The effects upon the line profiles of a steeply rising microturbulent velocity near 1500 km, similar to that considered in Sections 5 and 6 and in the Appendix.

The primary discrepancy between the observed and computed line profiles, as found by Dumont and by Athay and Skumanich, is that computed profiles tend to have central intensities considerably lower than observed. In Figures 11 and 12, we reproduce the comparison between observation and theory for an example by Dumont (1967b, Figure 18) and an example by Athay and Skumanich (1968a, model 3). Model 5 of Athay and Skumanich shows a somewhat higher central intensity than does their model 3, but the atmosphere of model 5 has an extremely rapid chromospheric temperature rise. The relatively good fit of the computed profile of Athay and Skumanich is partly due to the fact that the computed profiles have been matched to the observations at the  $K_2$  peak and at  $\Delta\lambda = 1 \text{ \AA}$ .

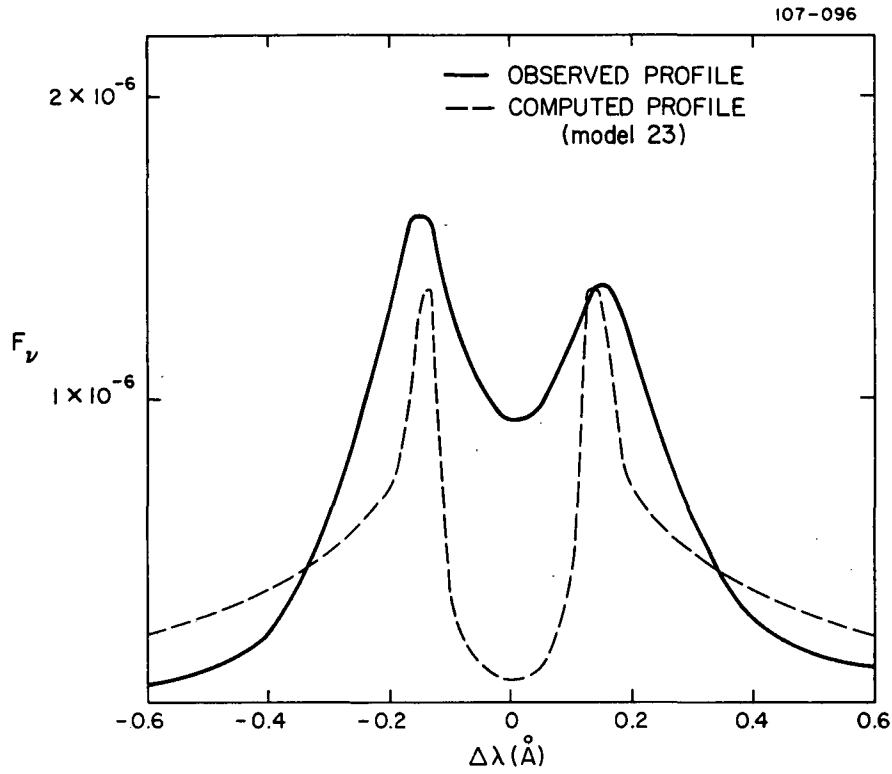


Figure 11. Computed and observed magnesium II K line profiles from Dumont (1967b).

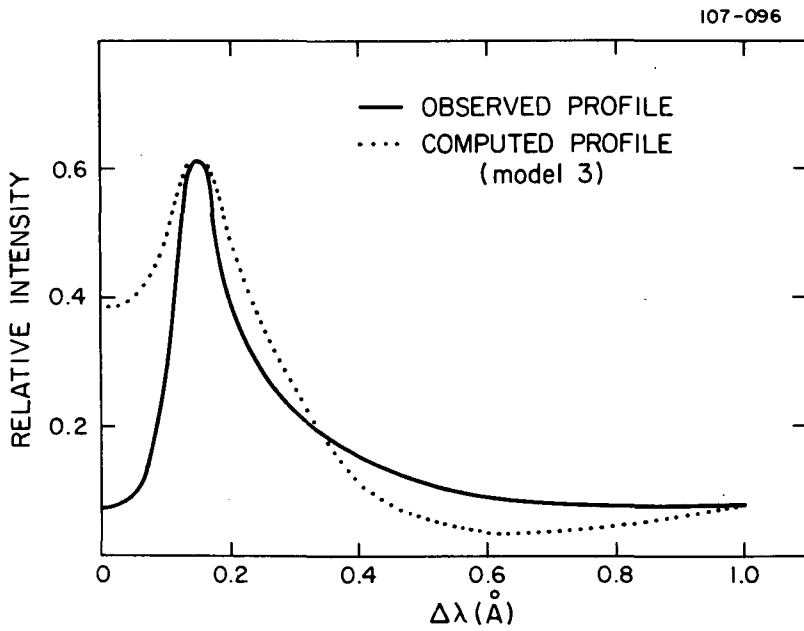


Figure 12. Computed and observed magnesium II K line profiles from Athay and Skumanich (1968a).

## 4.2 Observations

The profiles of the Mg II H and K lines used by Dumont were observed by Purcell, Garrett, and Tousey (unpublished) and reduced by Goldberg (1965). This K line profile is shown in Figures 11 and 12. The profile is an average over the whole solar disk, which led Athay and Skumanich to conclude that it is probably affected by active regions and therefore does not represent very accurately the profile of quiet regions of the solar disk. However, more recently, Lemaire (1969) has obtained stigmatic spectra of the Mg II doublet, which allow us to distinguish between active and quiet regions. The profile in a quiet region near the center of the solar disk would appear to resemble quite closely that of Goldberg (1965). Lemaire has also given a profile from a quiet region near the solar limb, but uncertainties due to instrumental transmission variations and to stray light make an accurate comparison between limb and disk-center profiles difficult. We have attempted an absolute calibration of Lemaire's profiles, based on Goldberg's calibration, which we plot in Figure 13. In this reduction we have averaged the red and blue wings of the line. We estimate the value of  $\mu$  for Lemaire's limb profiles to be 0.30.

## 4.3 Atomic Parameters

For the sake of simplicity, and because it should not greatly influence any of the effects that we wish to investigate, we have chosen to use a three-level model atom, as shown in Figure 14. We compute the formation of both the H and the K lines but shall discuss primarily the K line, the stronger of the two.

In Table 1, we have tabulated the various transition rates and line broadening constants. We have defined the rates in terms of the CE's, CI's, CRD's, and CVW's mentioned in Section 3. These quantities are tabulated for a temperature of  $5000^\circ$ , and they vary slowly with temperature. The exact temperature variation is taken into account in our calculations. We have put the level numbers in parentheses after the spectroscopic designations. In the table itself, we have used the convention of putting exponents in parentheses. We used a log abundance of 6.40, as found by Goldberg et al. (1960).

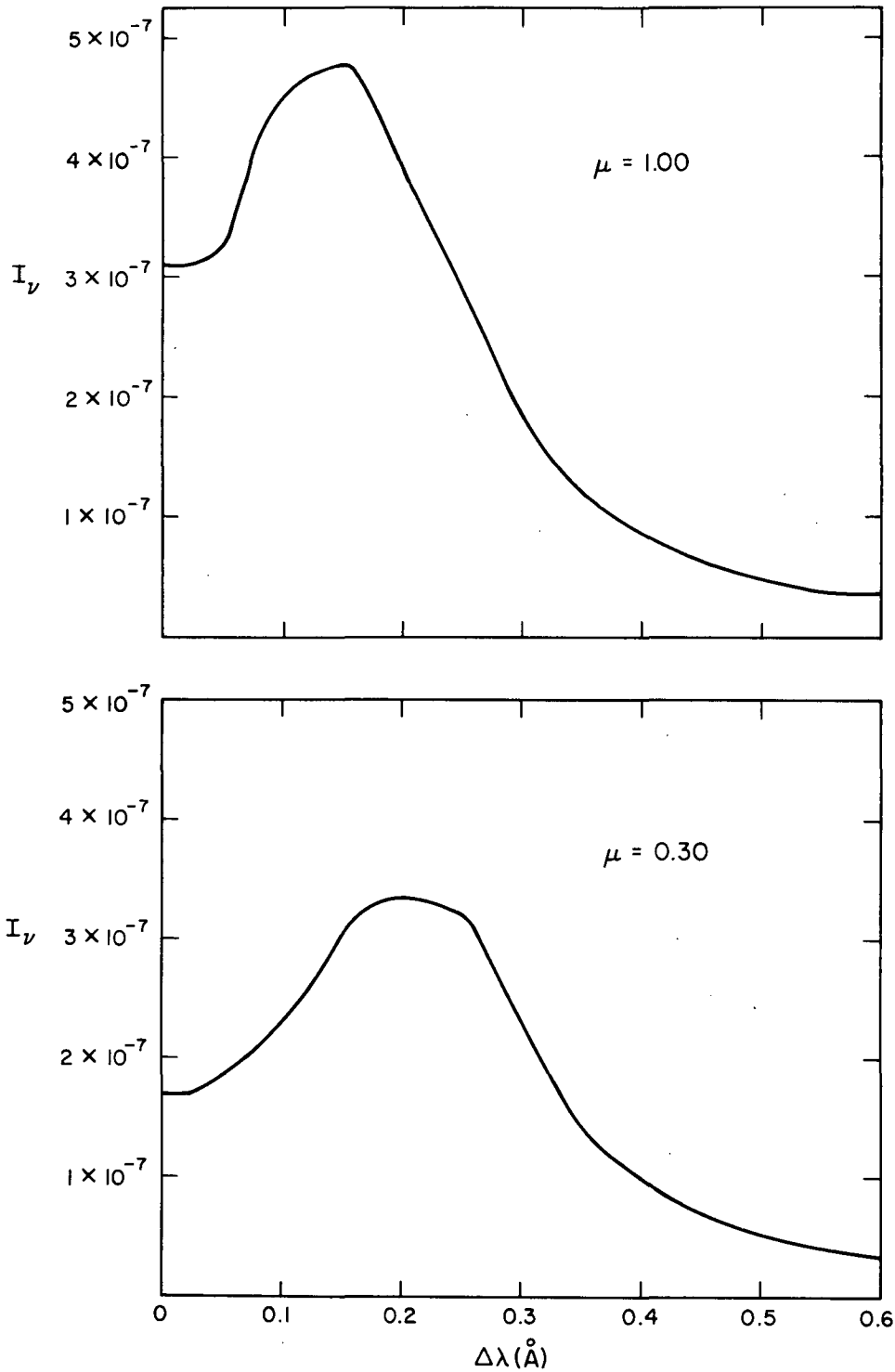


Figure 13. Magnesium II K line profiles observed by Lemaire (1969). Units for  $I_\nu$  are  $\text{ergs cm}^{-2} \text{sec}^{-1} \text{ster}^{-1} \text{Hz}^{-1}$ .

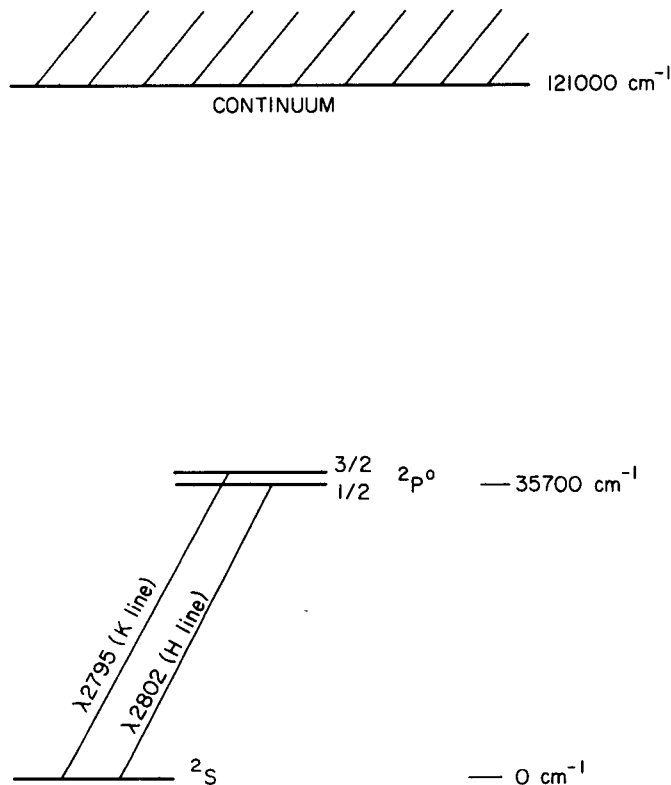


Figure 14. Three-level Mg II model atom.

The A values were taken from the compilation by Wiese *et al.* (1969). These values agree well with the experimental results of Corliss and Bozman (1962). The damping constants were calculated by using the formulas that we have developed in Section 3.

The collisional rate CE 3-2, between the fine-structure levels, was calculated by using the approximations of Bahcall and Wolf (1968). We included collisions with electrons, protons, and neutral hydrogen atoms. For electron collisions, we used an estimated collision strength of 1.0. We find that hydrogen-atom collisions dominate below 7000°, while above this point proton collisions are the most important. Electron collisions are about one-quarter as important as proton collisions.

Table 1. Atomic parameters for Mg II (standard temperature = 5000°).

		Upper Level	
		$2P^{\circ}_{1/2}(2)$	$2P^{\circ}_{3/2}(3)$
		Continuum	
	$2S_{1/2}(1)$	CE = 1.37 (-6) A = 2.66 (+8) CRD = 2.60 (-5) CVW = 1.67 (-4) CSK = 0	CE = 6.87 (-7) A = 2.68 (+8) CRD = 2.60 (-5) CVW = 1.67 (-4) CSK = 0 CI = 1.66 (-8) a = 1.71 (-17)
Lower Level	$2P^{\circ}_{1/2}(2)$		CE = 3.83 (-6) CI = 1.66 (-8) a = 2.35 (-17)
	$2P^{\circ}_{3/2}(3)$		CI = 1.66 (-8) a = 2.35 (-17)

We considered the possibility that transitions between the two  $^2P$  fine-structure levels might occur as rapidly via indirect two-step processes as by direct collisions. After doing the calculations reported as case 4 in the following section, we compared the rates for two different processes for two different heights in the atmosphere. Direct collisional rates between the  $^2P_{1/2}$  and  $^2P_{3/2}$  levels at heights of 1050 and 1800 km were  $2.79 \times 10^9$  and  $7.05 \times 10^5 \text{ cm}^{-3} \text{ sec}^{-1}$ , respectively. These heights mark the maxima in the source functions and the point at which the K line opacity equals unity. The dominant path for transitions between the  $^2P$  fine-structure levels via  $^2D$  is absorption from one  $^2P$  level to  $^2D_{3/2}$ , followed by decay into the other  $^2P$  level. This rate is restricted by the weak  $^2D_{3/2} - ^2P_{3/2}$  line, which has an A value of  $7.83 \times 10^7$ , so the total rate for transitions  $^2P_{3/2} - ^2P_{1/2}$  is given by  $n(^2D_{3/2}) \times A(^2D_{3/2} - ^2P_{3/2})$ . In order to evaluate this rate, we made a computation similar to case 4 below, in which we included only the ground state, the  $^2P_{1/2}$  level, and the  $^2D_{3/2}$  level, with the two lines joining these levels. The values calculated for  $n(^2D_{3/2})$  yield  $^2P_{3/2} - ^2P_{1/2}$  rates of  $8.4 \times 10^7$  and  $8.3 \times 10^4 \text{ cm}^{-3} \text{ sec}^{-1}$  at 1050 and 1800 km. A comparison with the direct rates shows that this process is smaller by a factor 10 to 30 than direct collisions and does not contribute significantly toward the total  $^2P_{3/2} - ^2P_{1/2}$  rate.

The choice of photoionization cross sections proved to be somewhat difficult. The general formula of Burgess and Seaton (1960) yields values of  $\alpha = 1.36 \times 10^{-19} \text{ cm}^2$  and  $\alpha = 4.32 \times 10^{-19} \text{ cm}^2$  at the heads of the  $^2S$  and  $^2P$  ionization continua, respectively, while the formula for photorecombination rates quoted by House (1964), which is derived from the general formula for photoionization cross sections of Elwert (1952), yields values of  $\alpha = 1.71 \times 10^{-17} \text{ cm}^2$  and  $\alpha = 2.35 \times 10^{-17} \text{ cm}^2$ , approximately 100 times as large.

We have chosen to use the larger values from House's formula, and we therefore compute ionization equilibria for Mg II/Mg III similar to those computed by House (1964) and by Jordan (1969). According to Jordan, dielectronic recombination from Mg III to Mg II is not very important, so House's and Jordan's calculations agree quite closely. If we were to use the lower photoionization cross sections, we would find a considerably higher Mg III/Mg II

ratio in the upper chromosphere than we actually do compute, but it is doubtful whether any of our results would be significantly different. Some calculations using the lower photoionization cross sections of Burgess and Seaton show changes of less than 15% at line center, and smaller changes elsewhere.

#### 4.4 Results

We shall discuss the points raised in Section 4.1 and present line profiles for the various cases. Four different cases were necessary in order to resolve the associated questions.

Case 1. A run was made with an atmosphere similar to the Harvard-Smithsonian Reference Atmosphere (HSRA), except that a temperature plateau of temperature 18,500 K, width 50 km, and electron density  $3.15 \times 10^{10}$  has been added on top of the steep temperature rise above 10,000 K. This atmosphere is shown in Figure 26, where the  $T_e$  curve is labeled (HSRA). The microturbulent velocity was assumed to rise gradually to a value of  $5 \text{ km sec}^{-1}$  at a height of 1150 km, and above this point was taken as constant at  $5 \text{ km sec}^{-1}$ . In Figure 15 we show this microturbulent velocity variation.

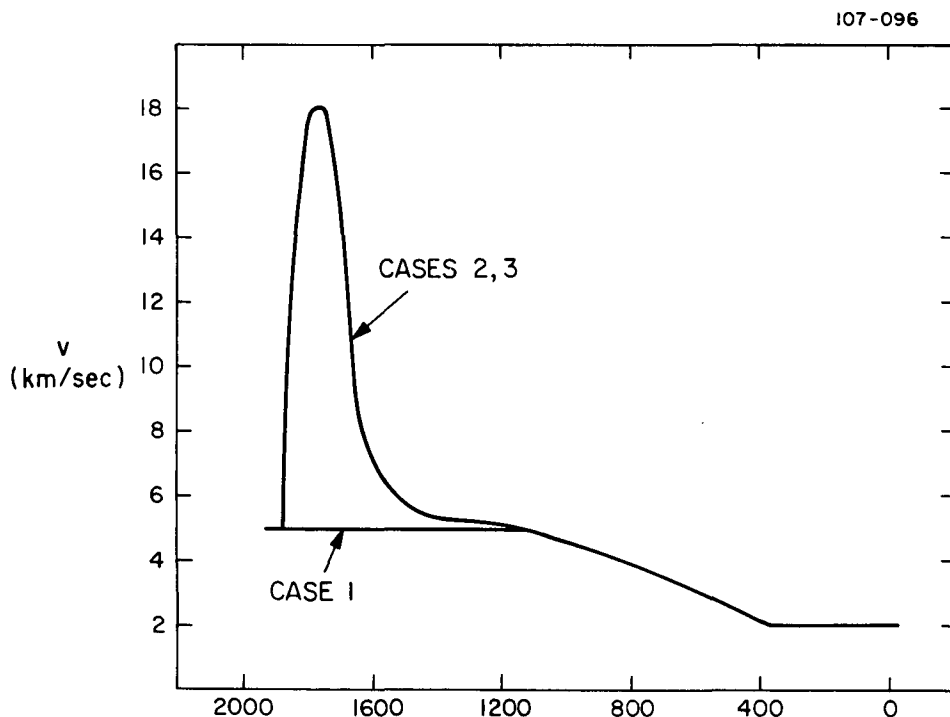


Figure 15. Microturbulent velocities for Mg II calculations.

The line profile for the K line at  $\mu = 1.0$  is shown in Figure 16, in comparison with the observation of Lemaire; the profiles for  $\mu = 0.3$  are shown in Figure 17. Although the total amount of emission, at least for  $\mu = 1.0$ , in the computed line is approximately equal to that observed, the computed peak intensity is considerably too great, while the computed central intensity is too small. This problem is discussed under case 2, below. The peak intensity is calculated to be  $8.66 \times 10^{-7}$ , while the peak in the source function is  $1.18 \times 10^{-6}$ , which occurs at 1100 km, where  $T_e = 5900^\circ$  and the line-center optical depth =  $1.8 \times 10^3$ .

With reference to point 2 mentioned in Section 4.1, we find that the chromospheric temperature plateau has a negligible effect upon the Mg II lines. Although we find that 0.5 of the Mg in the plateau region is singly ionized, the source function does not rise significantly above that at lower heights, so no effect of the plateau is observed. The Mg II lines at  $\lambda 2800$  are affected by the plateau far less than are the O I and C II lines near  $\lambda 1300$ , primarily because the Planck function is a much weaker function of temperature at the longer wavelength.

The lack of effect of the plateau and the fact that the peak in the source function occurs so deep in the atmosphere are the two primary reasons why the exact photoionization cross sections are not critical in determining the main features of the formation of the Mg II H and K lines.

Case 2. A second run was made with the same atmosphere as for case 1, except that a rapid increase in microturbulent velocity near 1650 km was assumed. In Figure 15, we show this velocity variation. Note that in this case, the rapid increase in  $v$  occurs at a height almost 100 km greater than shown for O I in Figure 28 (case 9). The heights of the increases in  $v$  depend on the optical depth scales in the lines, so any change in our adopted abundances, A values, or ionization equilibria might resolve this difference. Alternatively, the difference might indicate that the true situation is far more complex than can be dealt with in our model and that height-dependent isotropic microturbulence is an oversimplification.

The line profiles for the K line at  $\mu = 1.00$  and  $\mu = 0.30$  for this case are plotted in Figure 16 and Figure 17. The central intensity and intensity at

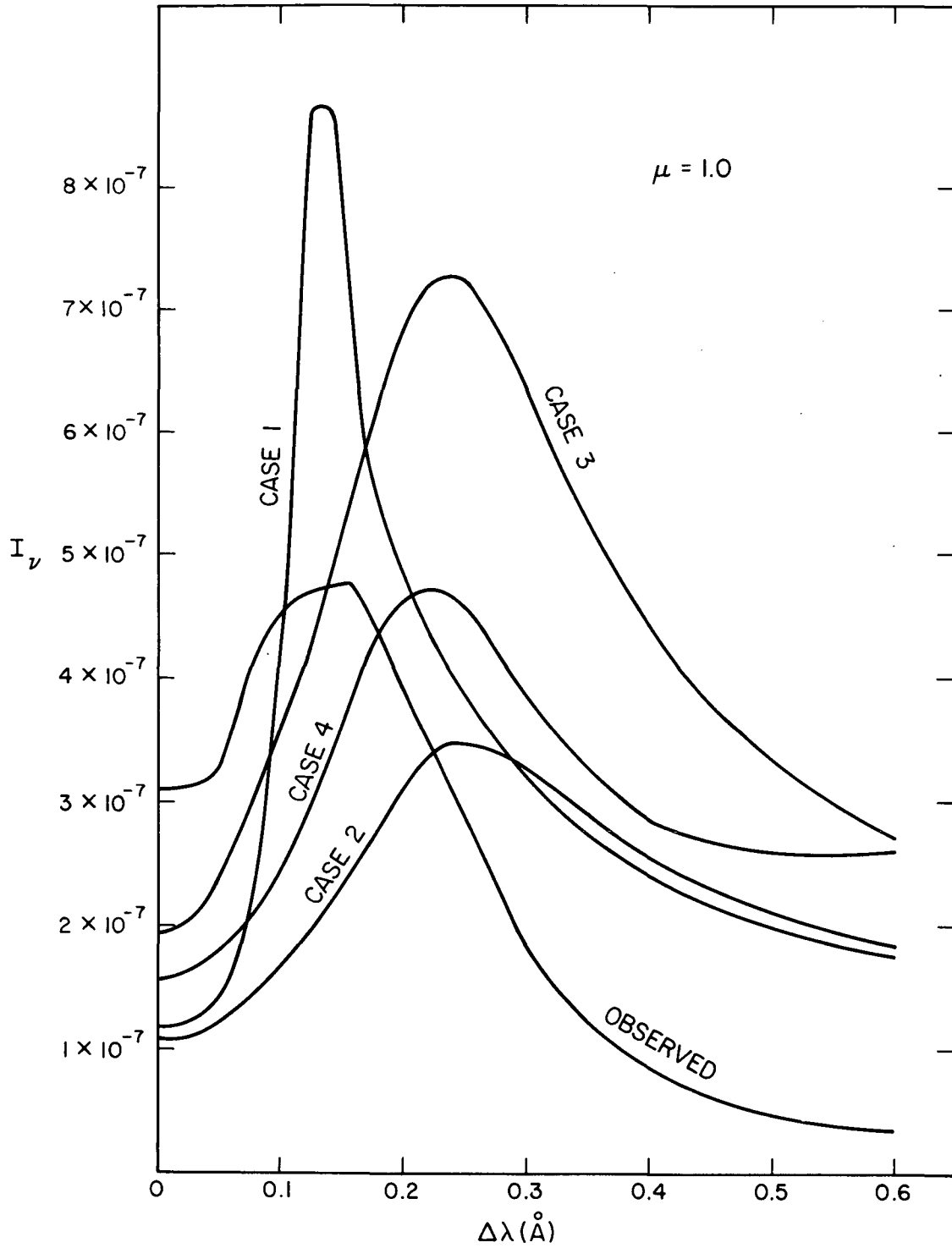


Figure 16. Observed and computed profiles for Mg II K at  $\mu = 1.0$ .

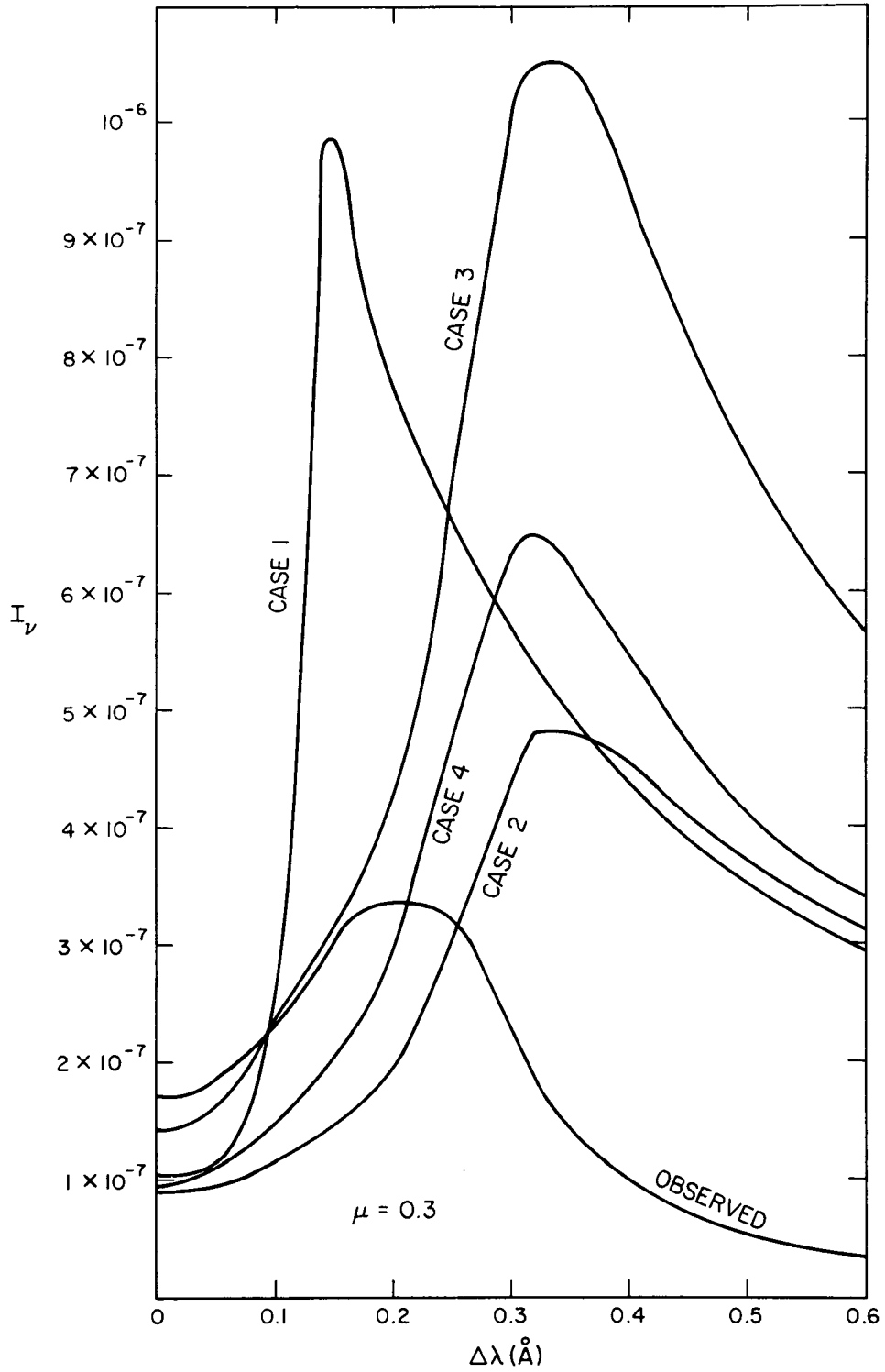


Figure 17. Observed and computed profiles for Mg II K at  $\mu = 0.3$ .

$\Delta\lambda = 0.6 \text{ \AA}$  are very similar to case 1, but the intensity in the peak region is much reduced, to the extent that at  $\mu = 1.0$  the computed peak intensity is smaller than that observed. The peak occurs at  $\Delta\lambda = 0.24 \text{ \AA}$ , rather than at  $0.14 \text{ \AA}$  as is observed, and the intensity for  $\Delta\lambda = 0.6 \text{ \AA}$  is considerably greater than the observations imply. None of our calculations yields an intensity for  $\Delta\lambda = 0.6 \text{ \AA}$  as low as the observations imply; this is due to the fact that the radiation temperature of the observed intensity is only  $3900^\circ$ , while the HSRA model atmosphere has a temperature minimum of  $4170^\circ$ .

Case 3. This case is identical to case 2, except that we have increased the assumed temperature of the atmosphere near 1200 km, as shown by the higher  $T_e$  curve in Figure 26. The general features of the line profiles are similar to those for case 2, but the intensities are greater by approximately a factor of two, and therefore the peak intensity exceeds that observed.

Case 4. In an effort to determine the importance of the line broadening, we experimented with several calculations wherein we set the Van der Waals and Stark broadening equal to zero and adjusted the radiative damping half-widths. For half-widths of  $10^{-5} \text{ \AA}$ , we computed the profiles plotted as case 4, with the same temperature-height relation as for case 3. At  $\mu = 1.00$ , case 4 would appear to show better agreement with the observations than do any of our other cases.

In order to show the effects of a steep microturbulent velocity gradient upon the contribution function for the emergent intensity, we have plotted in Figure 18 the contribution function for  $\Delta\lambda = 0.3 \text{ \AA}$  in the K line at  $\mu = 1.0$  as a function of line-center optical depth. The microturbulent velocity increase causes the contribution function to divide into two peaks, with a deep minimum between. For the case plotted, the optical depth of the first peak at  $\Delta\lambda = 0.3 \text{ \AA}$  is 0.205. If we were to consider smaller values of  $\Delta\lambda$ , we would find the first peak increasing in height and optical depth with the height of the second peak diminishing, and conversely for larger values of  $\Delta\lambda$ . As a result, there is no value of  $\Delta\lambda$  for which the region  $1.1 \leq \log \tau_c \leq 2.5$  contributes significantly to the emergent intensity. And one cannot really speak of a "depth where the

emission peaks are formed, " since it is precisely at wavelengths near the emission peaks that the most complete split into two contributing regions occurs.

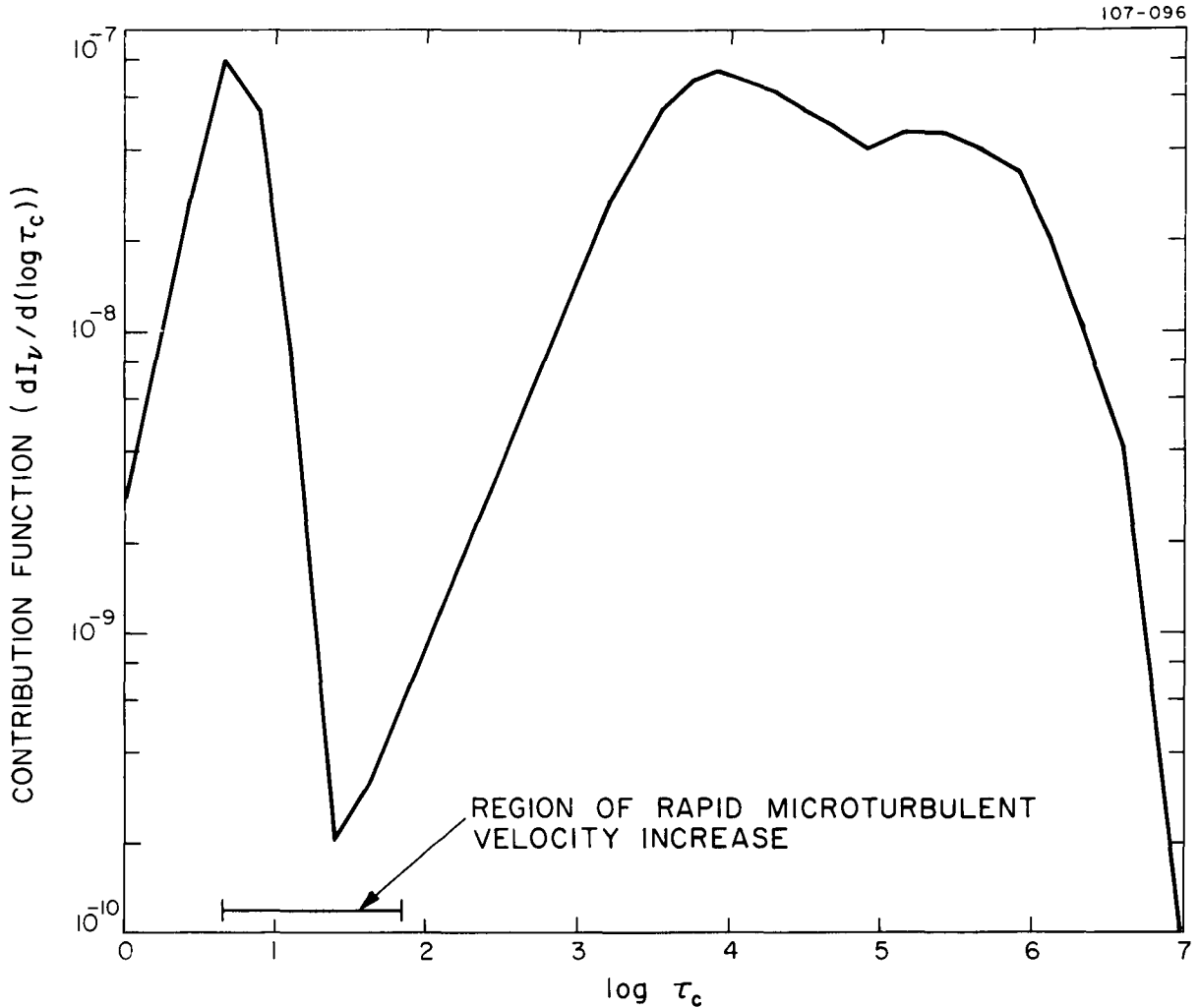


Figure 18. Contribution function versus  $\log \tau_c$  (line center) for  $\Delta\lambda = 0.3 \text{ \AA}$  in the Mg II K line at  $\mu = 1.0$  for case 4.

4.5 General Remarks

Our cases 2, 3, and 4 show poorer agreement for the peak intensity value of  $\Delta\lambda$  than do the calculations of Dumont, Athay, and Skumanich or of our case 1; on the other hand, the qualitative appearances of the line profiles, especially for case 4, are very similar to the observed profiles. The rapid increase in microturbulent velocity has little tendency to increase the computed central intensities, but the peak intensities can be considerably reduced. At  $\mu = 0.3$ ,

none of our calculated cases shows good agreement with the observations; possibly an analysis similar to that which we do for the Ca II K line in the Appendix would solve this problem. However, since the calibration of the limb-profile observations is very questionable, one should not base any conclusions on these profiles for the present.

## 5. THE OXYGEN I RESONANCE LINES

### 5.1 Comment on Ultraviolet Emission Lines

We wished to study some lines formed in the upper chromosphere and the chromosphere–corona transition region. After some investigation, it was decided to study in detail the resonance triplet of O I near  $\lambda$  1304, the resonance doublet of C II near  $\lambda$  1335, and the two strong lines of C III, which occur at  $\lambda$  977 and  $\lambda$  1176. These lines were chosen for several reasons:

1. As we conclude in Sections 5 to 7, the temperatures at which these lines are primarily formed are quite distinctly separated. We find the O I lines are formed mostly near  $7000^\circ$ , the C II lines at about  $18,000^\circ$ , and the C III lines at  $60,000^\circ$ , so we can study a wide range of regions of the solar atmosphere.

2. All these lines fall within the wavelength range observed by the OSO 4 satellite, so we can obtain limb-brightening curves for these lines and use photoelectric line intensities.

3. The O I and C II lines have large optical thicknesses ( $> 100$ ), so that their analysis uses the capabilities of the PANDORA program. The C III  $\lambda$  977 line is one of the most optically thick lines formed in its temperature region; it might contain information that cannot be obtained from optically thin lines. Also, we wished to compare our more elaborate analysis of this line with that of Withbroe (1970a).

4. Profiles of the C II lines  $\lambda$  1334 and  $\lambda$  1336 and of the O I lines  $\lambda$  1302,  $\lambda$  1304, and  $\lambda$  1306 have been observed by means of rockets (see Berger, Bruner, and Stevens, 1970; Bruner, Jones, Rense, and Thomas, 1970).

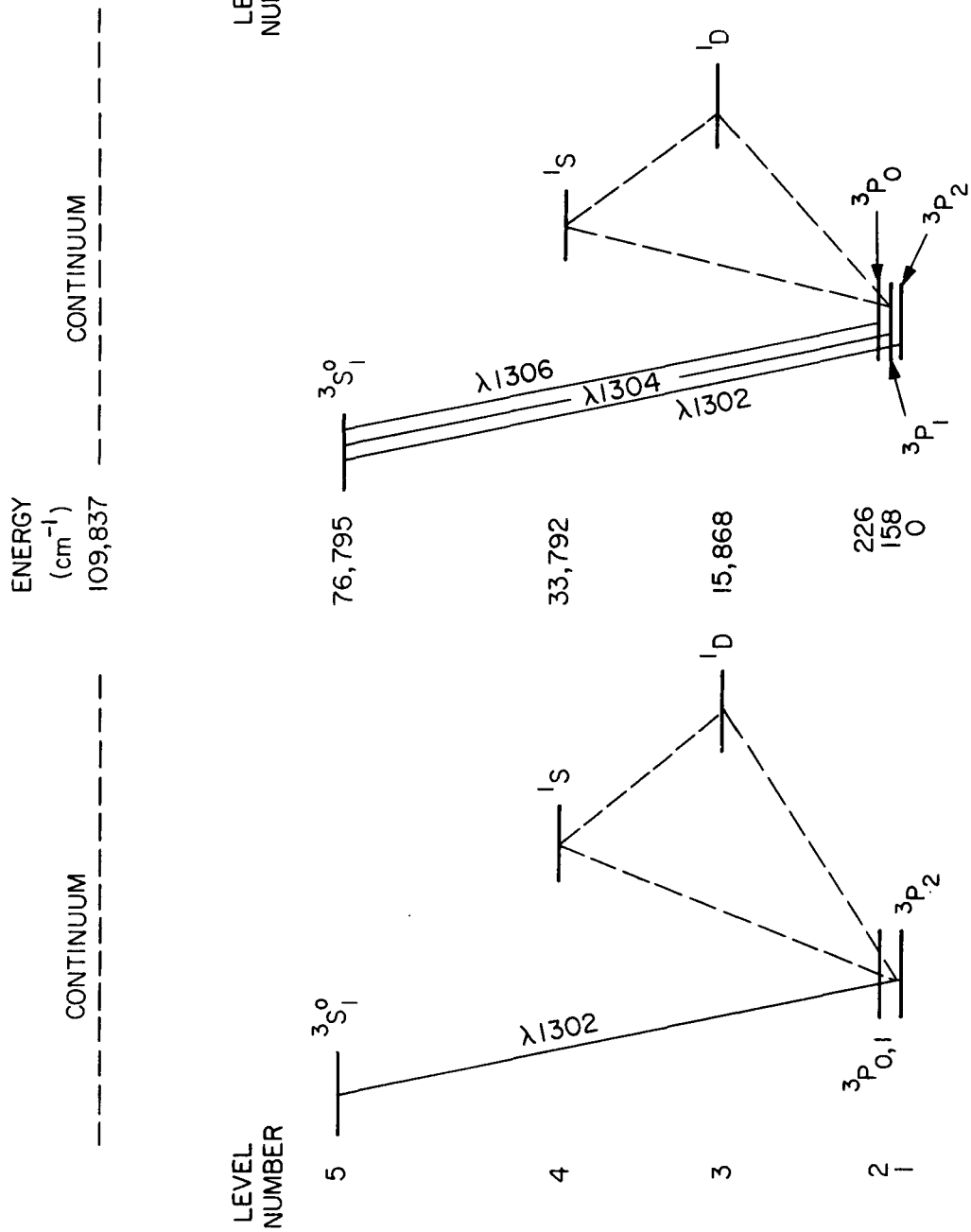
### 5.2 The O I Lines – Introduction

The three lines of O I, at  $\lambda$  1302.17,  $\lambda$  1304.87, and  $\lambda$  1306.03, are very prominent in emission in the solar ultraviolet spectrum. These lines arise

from transitions between the ground  $^3P_{0,1,2}$  levels and the  $^3S^0$  excited level. Figure 19b is an energy-level diagram for the six levels that were considered to be most important in the formation of the  $\lambda 1302$ ,  $\lambda 1304$ , and  $\lambda 1306$  resonance triplet (Moore, 1949). In order to use a minimum of computer time, some of our preliminary calculations were made using a simplified model atom, which includes only one radiative transition. The energy-level diagram for this model is shown in Figure 19a. On Figures 19a and 19b, we indicate by solid lines those transitions for which both radiative and collisional processes are included and by dashed lines those for which only collisions are important.

The O I resonance triplet has been observed with a high-resolution spectrograph carried in a rocket, as reported by Bruner and Rense (1969) and Bruner et al. (1970). These authors corrected the observed line profiles for absorption by atomic oxygen in the earth's atmosphere and found some uncertainty in the resulting profiles, due to the lack of precision in the model of terrestrial residual oxygen, which must be assumed in the correction process. For two different models of the earth's upper atmosphere, Bruner et al. (1970) derived emission lines with rounded peaks and no central absorption, and emission lines with a distinct central absorption, giving a central intensity of order 90% of the maximum intensity. This uncertainty should be resolved by profiles observed from satellites. The full width at half maximum for the lines was found to be approximately  $0.2 \text{ \AA}$ , and the distance between the emission peaks, if these peaks in fact exist, was found to be  $0.11 \text{ \AA}$ .

The profiles published by Bruner and Rense (1969), which indicated definite central absorption, were used as a basis for a theoretical study of the O I lines by Athay and Canfield (1970). Athay and Canfield could explain quite naturally what they took for the observed total intensities of the O I lines, but their computed line profiles show a large degree of central absorption, which is not observed. The model atmosphere chosen by Athay and Canfield rises gradually from the temperature minimum to about  $9000^\circ$  and then rises very rapidly, within less than 50 km, to temperatures above  $30,000^\circ$ . This



(a) Five-level model atom

(b) Six-level model atom

Figure 19. Five- and six-level models of the O I atom.

model is very different from the sort of model considered in Section 6 below, wherein a "temperature plateau" extending over about 100 km is found to exist at a temperature between 15,000 and 18,000°. We wished to determine whether a model atmosphere with such a temperature plateau would imply a smaller degree of central absorption than was found by Athay and Canfield.

Other observed quantities are the line intensities and the limb-brightening behavior. The published observations of the three O I resonance line intensities are few and somewhat incomplete. Pottasch (1964) quotes an NRL result that yields intensities for the  $\lambda 1302$ ,  $\lambda 1304$ , and  $\lambda 1306$  lines of 190, 295, and 365 ergs cm<sup>-2</sup> sec<sup>-1</sup> ster<sup>-1</sup>, respectively. This would imply that the line with the largest A value,  $\lambda 1302$ , is the weakest of the three, which might seem unlikely, and yet some of our best computations yield a similar result (see cases 5 and 6 below). In the plate published by Bruner and Rense (1969), the lines  $\lambda 1302.17$  and  $\lambda 1306.04$  have been mislabeled for one another, which can be seen by comparing the spacings and wavelengths, since the dispersion is linear. Therefore, the  $\lambda 1302.17$  line appears to be definitely weaker than the other two, or at least its intensity in the observed maxima is lower. Dupree and Reeves (1971) list an intensity of 398 ergs cm<sup>-2</sup> sec<sup>-1</sup> ster<sup>-1</sup> at the solar center for  $\lambda 1302$ , and 718 for the sum of the  $\lambda 1304$  and  $\lambda 1306$  lines, with an absolute accuracy of at least within a factor two. There are two factors that would tend to make the actual O I line intensities smaller than those tabulated by Dupree and Reeves, but neither should change their results by more than a few percent. First, the OSO 4 spectrometer had a bandpass of 3 Å, so the tabulated intensities include a certain amount of continuum radiation besides the lines. But the continuum intensity is only about 2% that of the lines, so this effect should be small. Second, there is a line of Si II,  $\lambda 1304.37$ , that falls within the O I triplet. This Si II line is, however, so weak that it barely appears at the limits of detection on the spectrogram published by Bruner and Rense (1969), while the O I lines are well exposed. So we will use Dupree and Reeves' values as published. Dupree and Reeves' result would indicate that the  $\lambda 1302$  line is by a small margin the strongest of the three. At any rate, it seems clear that the intensities are not in the ratio of the A values, which we might expect for an optically thin emitting region. Optically thin conditions would give an intensity ratio of 5:3:1 for the three lines,  $\lambda 1302$ :  $\lambda 1304$ :  $\lambda 1306$ . Apparently, Athay and Canfield (1970)

made an arithmetic error of a factor of four in converting from flux at the earth's orbit to intensity at the sun, as they derive intensities of 37 for each of the lines. The correct factor, for a line with a flat limb-brightening behavior, is

$$\frac{I(\mu = 1)}{F_{\oplus}} = 1.47 \times 10^4, \quad (141)$$

so that the flux of 0.01 adopted by Athay and Canfield should correspond to an intensity of 147.

The limb brightening, involving a relative rather than an absolute measurement, is somewhat easier to determine. Using the data from the OSO 4 satellite (Reeves and Parkinson, 1970a), we have constructed an average limb-brightening curve for the combined flux from the  $\lambda$  1304 and  $\lambda$  1306 lines, in the way described by Withbroe (1970b). All data points lying between solar latitudes  $\pm 10^\circ$  were used, except for a few that were rejected after a visual inspection. The rejected points are portions of active regions that extend into the equatorial region. This limb-brightening curve is shown in Figure 20, along with that computed for case 9, below. The peak of the limb-brightening curve appears to fall near  $I(\mu)/I(\mu = 0) = 1.15$ , except for one point of rather low weight, which is near 1.30. The best value probably falls between 1.15 and 1.20.

### 5.3 Atomic Constants

We denote the levels of our model atoms by a level number, shown on Figures 19a and 19b. In Tables 2 and 3, we tabulate the various adopted atomic constants for the two models. We shall proceed to discuss the sources of data and the notations used in these tables.

The level designations, energies, and statistical weights were taken from Moore (1949). The photoionization cross sections from the  $^3P$ ,  $^1D$ , and  $^1S$  states were derived from the calculations reported by Henry (1970), while the photoionization cross section from the  $^3S$  state was computed by using the tables of Peach (1967). We tabulate the cross sections at the head of the continua, and in Figure 21 we display the wavelength dependence of the

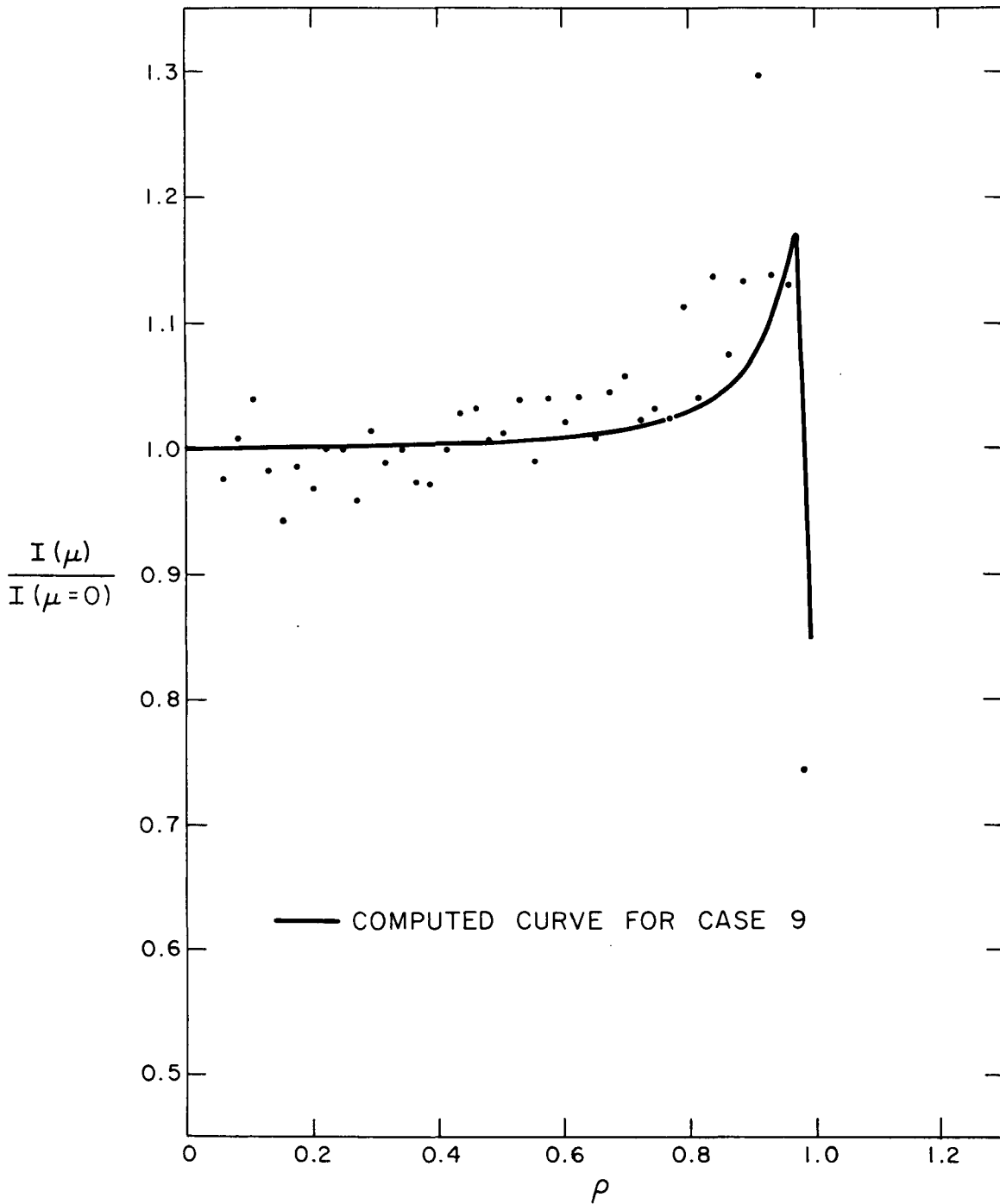


Figure 20. O I  $\lambda$  1305 limb brightening from OSO 4 data and one theoretical curve.

Table 2. Constants for the six-level model atom.

	Level number					
	1	2	3	4	5	6
Designation	$2p^4\ ^3P_2$	$2p^4\ ^3P_1$	$2p^4\ ^3P_0$	$2p^4\ ^1D$	$2p^4\ ^1S$	$2p^3\ 3s\ ^3S^o$
Energy ( $\text{cm}^{-1}$ )	0	158	226	15867	33792	76795
Statistical weight	5	3	1	5	1	3
Photoionization cross section	2.94 (-18)	2.94 (-18)	2.94 (-18)	4.64 (-18)	7.65 (-18)	1.12 (-20)
Collisional ionization parameter ( $8000^\circ$ )	2.22 (-8)	2.22 (-8)	2.22 (-8)	3.03 (-8)	4.63 (-8)	6.32 (-8)

	Transition		
	6-1	6-2	6-3
Wavelength	1302.17 A	1304.87 A	1306.03 A
A value	2.10 (+8)	1.26 (+8)	4.20 (+7)
Radiative damping	1.50 (-5)	1.50 (-5)	1.50 (-5)
Stark damping ( $N_e = 10^{12}$ , $T_e = 8000^\circ$ )	7.0 (-8)	7.0 (-8)	7.0 (-8)
Van der Waals damping ( $N_{HI} = 10^{16}$ , $T_e = 8000^\circ$ )	5.0 (-5)	5.0 (-5)	5.0 (-5)
Collisional-rate parameter ( $T_e = 8000^\circ$ for $Q = 1$ )	7.25 (-8)	7.25 (-8)	7.25 (-8)

Transition	Collisional-rate parameter (at $8000^\circ$ )
5-4	1.63 (-9)
5-3	2.89 (-10)
5-2	2.89 (-10)
5-1	2.89 (-10)
4-3	2.82 (-9)
4-2	2.82 (-9)
4-1	2.82 (-9)
3-1 (electrons)	negligible
3-1 (protons)	1.10 (-8)
3-1 (H atoms)	1.50 (-9)
3-2 (electrons)	negligible
3-2 (protons)	1.10 (-8)
3-2 (H atoms)	1.50 (-9)
2-1 (electrons)	negligible
2-1 (protons)	1.10 (-8)
2-1 (H atoms)	1.50 (-9)

Table 3. Constants for the five-level model atom.

	Level number					
	1	2	3	4	5	Continuum
Designation	$2p^4 3P_2$	$2p^4 3P_{0,1}$	$2p^4 1D$	$2p^4 1S$	$2p^3 3s 3S^0$	$2p^2 4S^0$
Energy ( $\text{cm}^{-1}$ )	0	175	15867	33792	76795	109837
Statistical weight	5	4	5	1	3	4
Photoionization cross section	2.94 (-18)	2.94 (-18)	4.64 (-18)	7.65 (-18)	1.12 (-20)	
Collisional ionization parameter ( $8000^\circ$ )	2.22 (-8)	2.22 (-8)	3.03 (-8)	4.63 (-8)	6.32 (-8)	

		Transition
		5-1
Wavelength		1302.17 A
A value		1.375 (+8)
Radiative damping		1.50 (-5)
Stark damping	( $N_e = 10^{12}$ ) ( $T_e = 8000^\circ$ )	7.0 (-8)
Van der Waals damping	( $N_{HI} = 10^{16}$ ) ( $T_e = 8000^\circ$ )	5.01 (-5)
Collisional-rate parameter	( $T_e = 8000^\circ$ for $Q = 1$ )	7.25 (-8)

Transition		Collisional-rate parameter (at $8000^\circ$ )
4-3		1.63 (-9)
4-2		2.89 (-10)
4-1		2.89 (-10)
3-2		2.82 (-9)
3-1		2.82 (-9)
2-1	(electrons)	negligible
2-1	(protons)	1.10 (-8)
2-1	(H atoms)	1.50 (-9)

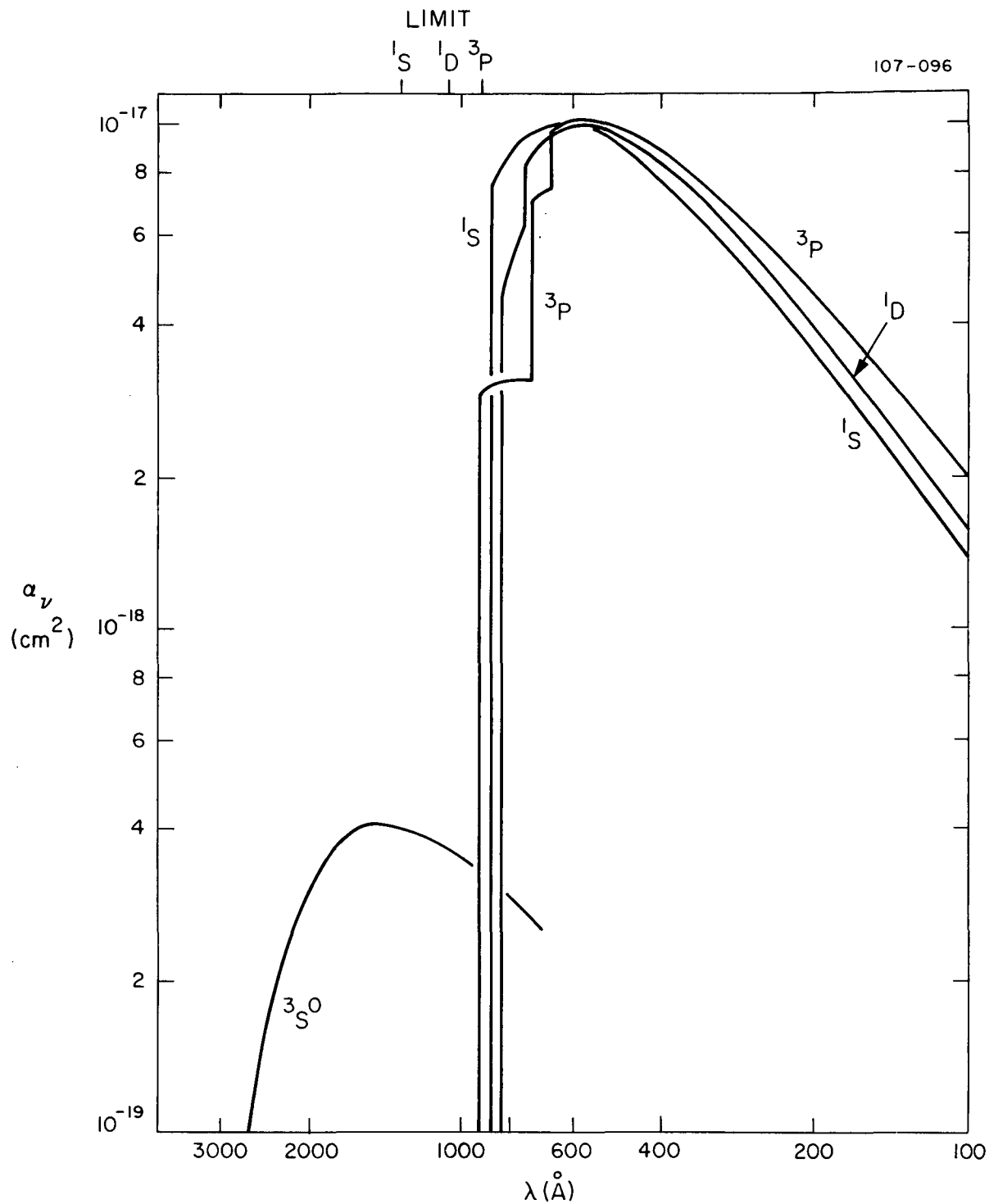


Figure 21. Photoionization cross sections for O I.

various continua. The detailed wavelength behavior of the photoionization cross sections was used in our computations. The collisional ionization rates were calculated according to the formula of House (1964). We tabulate the parameter  $C I$  defined in equation (131) for each transition at  $8000^\circ$ . Here also the exact temperature variation of  $C I$  was used.

The  $A$  value was derived from the experimental result of Parkes *et al.* (1967), who found  $f = 0.021 \pm 0.003$  for each of the three lines of the oxygen resonance triplet. The three damping parameters were calculated from the work of Griem (1964) and are expressed as (half) half-widths in angstroms. The collisional rates for the transitions between the terms  $^3P$ ,  $^1D$ , and  $^1S$  were adopted from the calculations of Henry and Williams (1968). Again we tabulate the parameters  $CE$  at  $8000^\circ$  but use the exact temperature variation.

For collisional transitions between the fine-structure levels of the  $^3P$  ground state, Bahcall and Wolf (1968) found that electron collisions are unimportant in comparison with proton and neutral-hydrogen atom collisions. Since  $\Delta E \ll kT$ , we have used their high-temperature approximations for fine-structure transitions induced by protons and by hydrogen atoms. According to the calculations of Dalgarno and Degges (1968), the electron collision rates are not negligible but are comparable to the proton collision rates. In any case, the rates are large enough that the population ratios of the  $^3P^o$  levels are always close to the ratios of the statistical weights. More recently, Wofsy, Reid, and Dalgarno (1971) have calculated cross sections for two of the fine-structure transitions due to collisions with neutral hydrogen atoms. They find a strong oscillatory behavior in the cross sections for small relative energies.

The collisional cross section for excitation of the  $^3S^o$  level, which is the upper level of the resonance triplet, is important for the solution of this problem but was not accurately known when our computations were made. Athay and Canfield (1970) have used cross sections of both  $0.1 \pi a_0^2$  ( $Q = 0.1$ ) and  $Q = 0.4$ . Stauffer and McDowell (1966) have computed the cross section by using an impact-parameter method. Judging from their curves, the most probable cross section is between  $Q = 0.5$  and  $Q = 2.0$ . On the other hand,

if we evaluate the cross section by using Van Regemorter's formula (equation 123), we find, at  $8000^\circ$ , that  $Q = 1.03 \times 10^{-2}$ . This extremely low value always yields insufficient emission in computed profiles and must be an underestimate of the cross section. Recently, Stone and Zipf (1971) have measured total excitation cross sections for the  $^3S^0$  level of O I. They find values somewhat higher than those predicted by Stauffer and McDowell and conclude that excitation of  $^3S^0$  via cascade from higher levels is important. In our later cases below, we use values close to those found by Stone and Zipf.

It turns out that under many conditions, the reaction  $O + H^+ \leftrightarrow H + O^+$  can be the dominant factor in the ionization equilibrium of oxygen (see Field and Steigman, 1971). The hydrogen ionization equilibrium will be little affected by this reaction, owing to the relatively low abundance of oxygen. The general effect of this reaction will be to drive the ionization equilibrium of oxygen to practically the same degree of ionization as we have for hydrogen (except for statistical weight factors), whatever that degree may be.

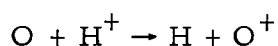
As an example, consider a situation such as that of the chromospheric plateau near  $20,000^\circ$ , where we can take

$$\begin{aligned} N_e &= 3 \times 10^{10}, \\ N_{H^+} &= 3 \times 10^{10}, \\ N_{HI} &= 3 \times 10^8, \\ T_e &= 2 \times 10^4. \end{aligned}$$

Then, using House's formula for ionization rate from the ground state of O I, we have, for collisional ionization,

$$C_{1K} = 0.40 \text{ sec}^{-1},$$

whereas the rate for a given oxygen atom of the reaction



is, according to Field and Steigman,

$$C_{\text{O-H}^+} = 63 \text{ sec}^{-1} .$$

So for ionization, this charge-exchange reaction is the most important by a factor of order 100. A similar calculation for recombination gave a photo-recombination rate of  $5.0 \times 10^{-3}$ , with a rate for  $\text{O}^+ + \text{H} \rightarrow \text{H}^+ + \text{O}$  of 0.6, or once again an enhancement of order 100.

Because of the dominance of this reaction, we can compute the ratio of optical depth in the center of the  $\lambda 1302$  line of O I to that in the head of the Lyman continuum, assuming only an abundance of oxygen and a line-broadening temperature. Using an abundance  $6.0 \times 10^{-4}$ ,  $T_e = 20,000$  K, and an  $A$  value for  $\lambda 1302$  of  $1.375 \times 10^8$ , we find

$$\frac{\tau(911)}{\tau_c(\lambda 1302)} = 1.2 .$$

This is important, since the optical depth of the chromospheric plateau in the Lyman continuum is strictly limited by the observations. Vernazza, Avrett, and Loeser (1971) find an optical depth at the head of the Lyman continuum for their models of the formation of the hydrogen spectrum of slightly less than 0.1. We should therefore expect optical depths in  $\lambda 1302$  of approximately 0.05 in the chromospheric temperature plateau if this plateau is indeed important in the formation of the O I resonance lines.

As explained in Section 3.3, PANDORA has a variety of forms in which one can specify the photoionization and radiative recombination rates. For O I, we made an initial calculation of these rates using the photoionization cross sections of Figure 21 and the opacity routines contained in PANDORA. The actual non-LTE radiation intensities in the Lyman continuum are thus taken into account, since the opacity routines use the specified electron densities and ground-state neutral-hydrogen densities that were taken from the HSRA (Gingerich et al., 1971). For later calculations, we input these known photoionization and recombination rates rather than calculate them afresh

for each case. As pointed out below, we sometimes increased the recombination rates by a constant factor, to partially take into account dielectronic recombination.

#### 5.4 Calculations and Results

Our first series of calculations was made by using a model atmosphere that consisted of the Harvard-Smithsonian Reference Atmosphere (Gingerich *et al.*, 1971), on top of which was fitted a high-temperature "plateau" region of 15,000 to 19,000°. Several different cases were computed in which we varied some atomic parameters and used different models of the plateau region. We will discuss some of these results but should point out in advance that no reasonable combination of parameters and atmospheric model was found that could yield good agreement between theory and observation of line intensities, line profiles, relative intensities of the three lines, and limb-brightening behavior. The only way in which we could obtain computed intensities equal to those observed was to hypothesize that most of the line emission arises in the plateau region, but in this case the line relative intensities and the limb-brightening behavior would not agree with the observations. In general, for the portion of the line formed at temperatures below 10,000°, our results agreed closely with those of Athay and Canfield (1970). That is, the line intensity is only weakly dependent on the excitation cross section, and in the wings of the line, the line profile depends strongly on the Van der Waals broadening half-width that we adopted. To a first approximation, the line intensity is proportional to the square root of the excitation cross section, which is what we expect for the surface value of the source function of an optically thick line. We shall describe some cases illustrating the points just made.

Case 1. A run was made using a model atmosphere with a plateau at 15,000° and a five-level atom. We used rather conservative values for the collisional excitation rates and for the Van der Waals broadening constant, as follows:

$$CE\ 5-1 = 1.56 \times 10^{-8} \quad (Q = 0.22)$$

and

$$\text{CVW } 5-1 = 5.01 \times 10^{-5} \text{ \AA} \quad \text{for } N_{\text{H}} = 10^{16} \quad (= \text{Griem's value})$$

(see Section 3 for the definitions of CE and CVW). In addition, the adopted recombination rate in the plateau was probably somewhat low, in that we did not take into account the effects of dielectronic recombination or charge-exchange collisions with hydrogen. We used rates calculated directly from the cross sections of Figure 21 and found a degree of ionization in the plateau of about 0.96, with an optical depth in  $\lambda 1302$  in the plateau of  $\sim 0.05$ .

In Figure 22, we plot  $T_e$ ,  $N_e$ ,  $N_{\text{H}}$ , and  $N_{\text{HI}}$  for this atmosphere. Below 1500 km, the atmosphere is the HSRA, plotted in Figure 26. In Figure 23, we plot  $S$  and  $B_\nu$ ; the microturbulent velocity is shown in Figure 28. In Figure 24, we show the line profile at disk center and at  $\mu = 0.3$ . In Figure 24 and later figures in which we plot line profiles, we show two possible observed profiles in the line core, denoted by a solid line and a dashed line. These profiles correspond to the two possible profiles for each line published by Bruner *et al.* (1970). Note the filled-in character of the core of the calculated line profile, which is caused by emission in the plateau. This emission allows a good agreement between observed and computed line-profile shapes, but not intensities. The intensity calculated is 33, similar to the value 37 of Athay and Canfield. For this case, we calculated the maximum degree of limb brightening to be 1.40, taking the instrumental spatial resolution into account. Part of this limb brightening is caused by the  $1/\mu$  brightening of the intensity contribution from the chromospheric plateau, so we might conclude that the observed limb brightening of 1.15 or so implies that the contribution from the plateau must be small. Of course, inhomogeneities might well affect the limb-brightening behavior of this line, so we will not attempt to match exactly the number 1.15. Another portion of the limb brightening is due to the large increase in strength of the line wings for  $\mu = 0.3$ . This increase depends on the adopted Van der Waals broadening constant. We discuss below the comparison between limb brightening in the  $\lambda 1302$  line, which is what we calculate in our cases with five-level atoms, and the limb brightening in the sum of the

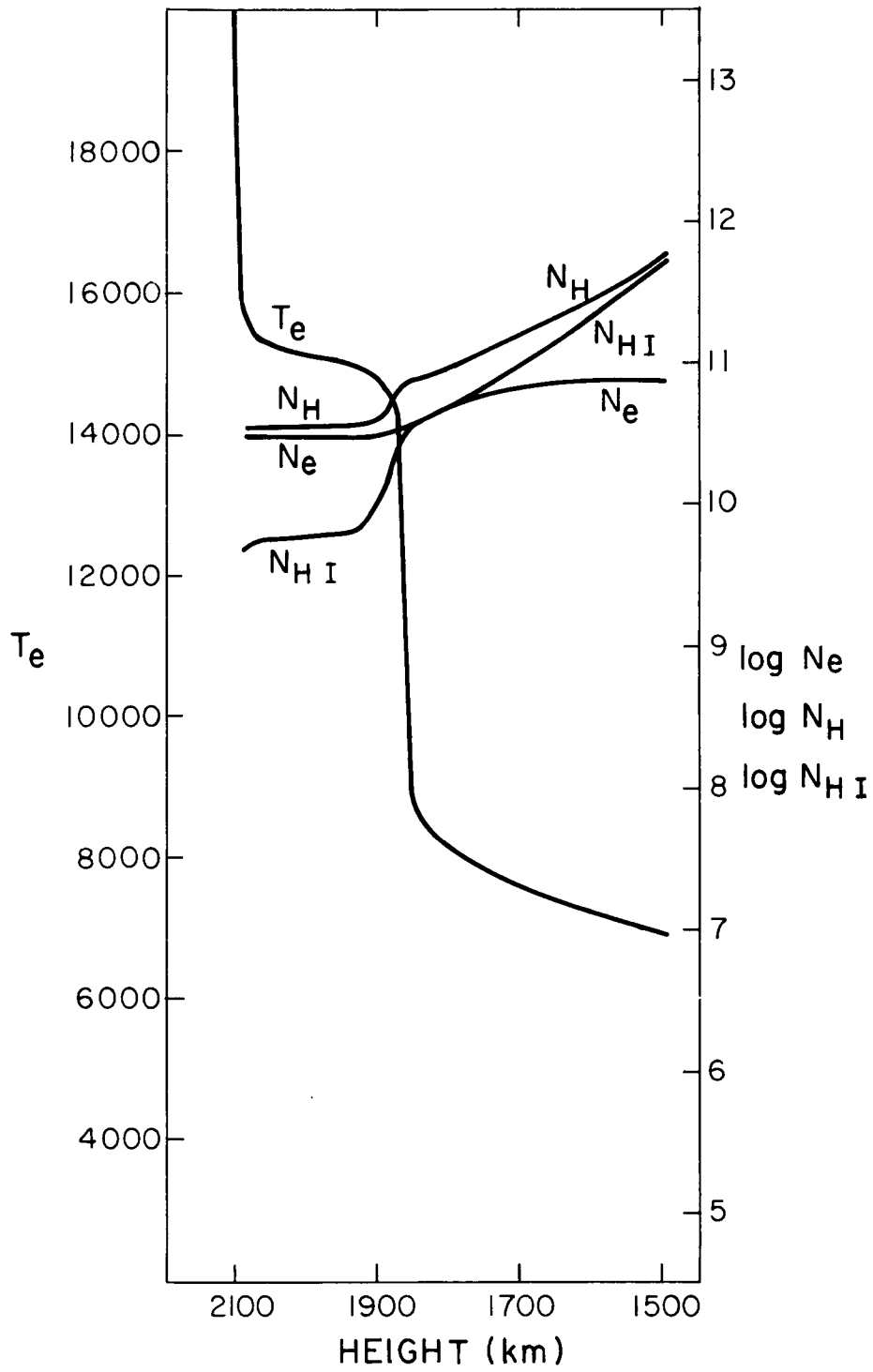


Figure 22. Atmosphere for case 1.

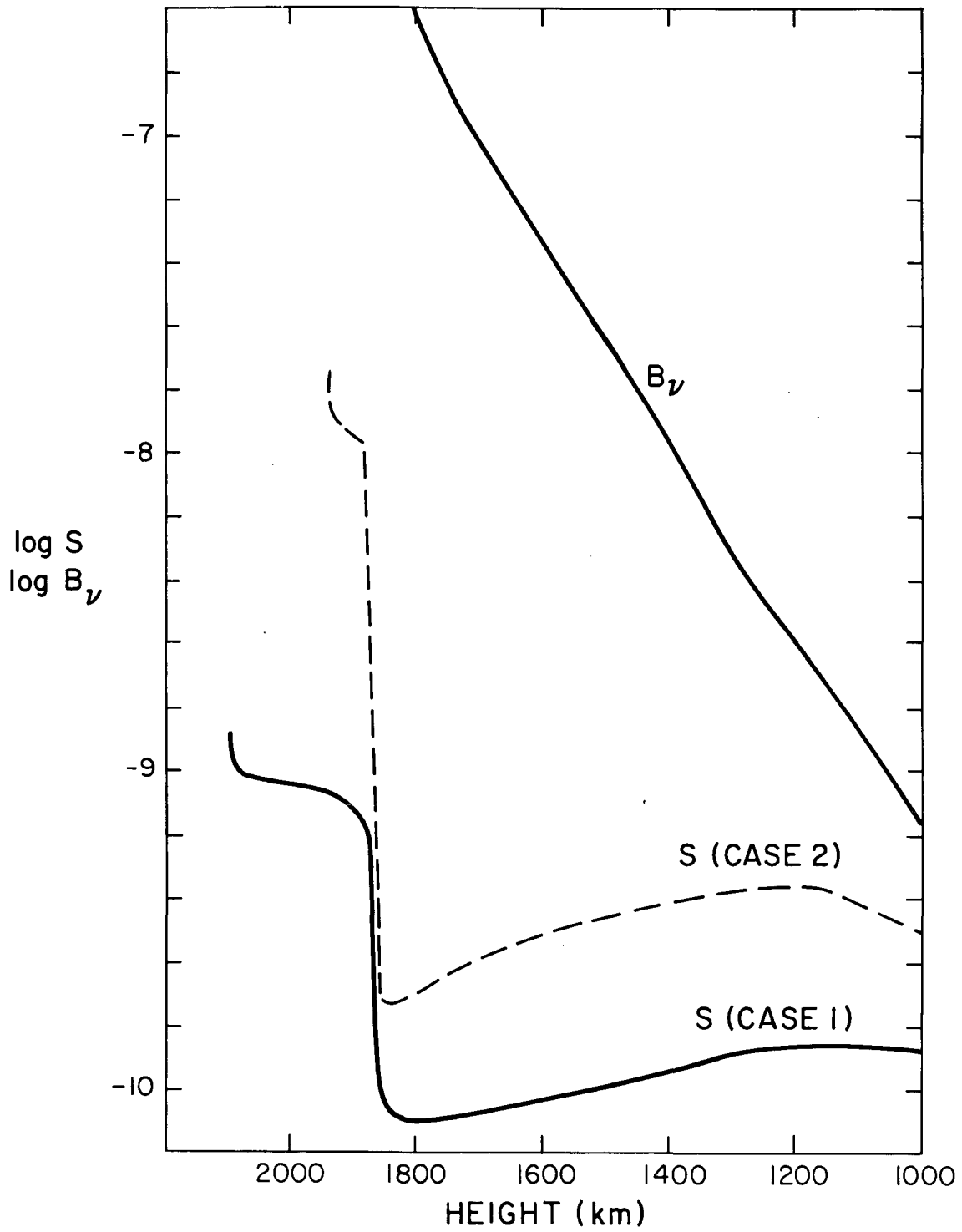


Figure 23. S and  $B_v$  versus height for cases 1 and 2.

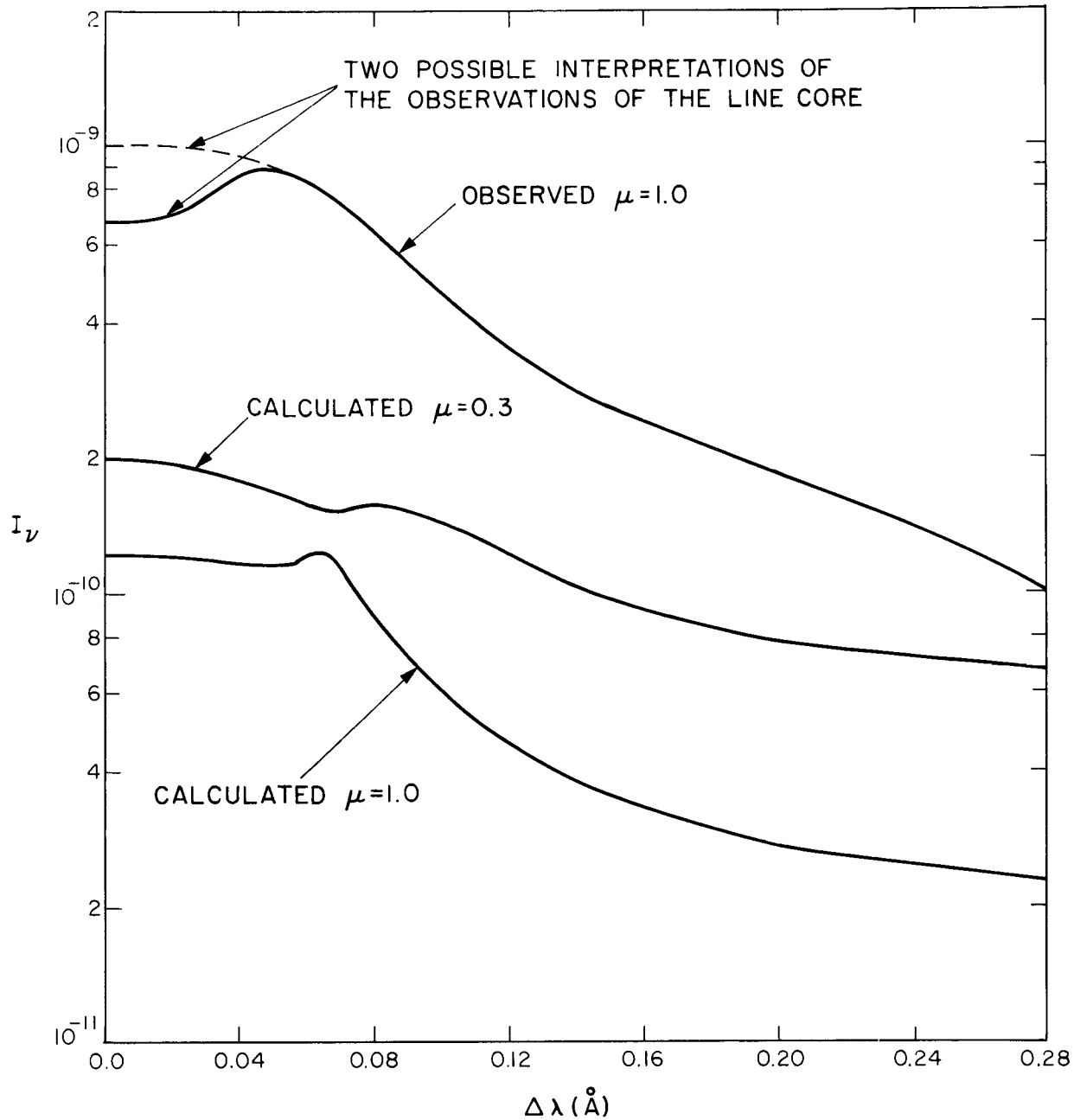


Figure 24. Profiles for  $\lambda 1302$ , case 1, at  $\mu = 1.0$  and  $\mu = 0.3$ .

$\lambda$  1304 and  $\lambda$  1306 lines, which is the quantity observed by the OSO 4 satellite. For our cases for which we use a six-level model atom, we can compute both these limb-brightening curves and compare them.

Case 2. Since the computed line strength is so small for case 1, we computed another case in which we used considerably higher values of CE 5-1 and CVW 5-1 in order to obtain a greater computed line intensity. We wished to determine whether it was possible that the low computed intensities for case 1 were due to an underestimate of the excitation and broadening parameters. We therefore chose the following parameters, enhanced by factors of 8 and 10 over those of case 1:

$$\text{CE 5-1 } (\lambda 1302) = 1.34 \times 10^{-7} \quad (\text{at } T_e = 8000^\circ)$$

$$\text{CVW 5-1 } (\lambda 1302) = 5.0 \times 10^{-4} \times \frac{N_{\text{HI}}}{10^{16}}$$

This value of CE 5-1 corresponds to  $Q = 1.85$ . In this case, we have used a slightly different model atmosphere from that used in case 1. We used a model that is based on the HSRA below 1850 km height but that rises to a plateau whose temperature is  $18,500^\circ$  and has a width of 50 km, at a density of  $N_e = 3.15 \times 10^{10}$ . The higher temperature of the plateau, in comparison with case 1, was suggested by the work of Vernazza *et al.* (1971) and is similar to our last example for C II in Section 6. This higher temperature makes the computed fractional ionization so great that the plateau plays a smaller role in the computed line profiles and intensities for this particular case than it does for case 1. In accordance with the last example in Section 6, we have used a new variation of microturbulent velocity with height, such that  $v = 0$  in the chromospheric plateau. This is why the emission peaks in the core of  $\lambda$  1302, as shown in Figure 25, are so narrow.

In Figure 23, we have plotted the source function for this case alongside the source function for case 1. It will be noted that in the vicinity of the local maximum near 1300 km, the source function is enhanced over that of case 1 by a factor of approximately three, which is  $\sqrt{9}$ ; this increase is due primarily to the higher value of CE 5-1 and shows the relative insensitivity of the line intensity to the collisional excitation cross section. In Figure 25, we show

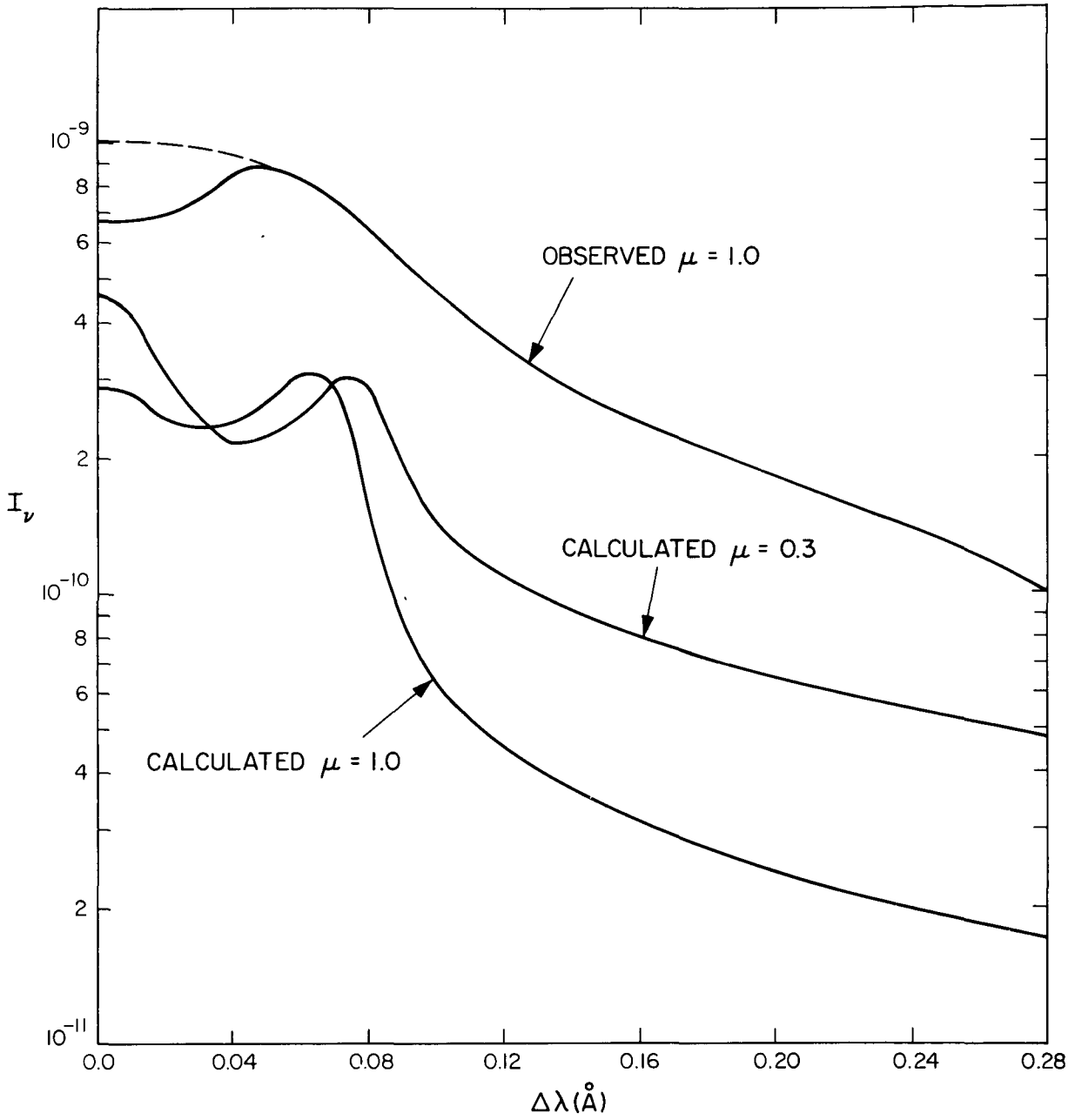


Figure 25. Profiles for  $\lambda 1302$ , case 2, at  $\mu = 1.0$  and  $\mu = 0.3$ .

the profiles of the  $\lambda 1302$  line for case 2 at  $\mu = 1.0$  and  $\mu = 0.3$ . The intensity of this line at  $\mu = 1.0$  is computed to be 84, while the limb-brightening curve for this line reaches a maximum value of 1.13. This lower value of the limb brightening is due mainly to the smaller amount of emission by the chromospheric plateau.

Case 3. However, even with our very high choice of CE 5-1 and CVW 5-1 in case 2, we still compute an intensity for  $\lambda 1302$ , which is a factor 4 to 5 too small. We are led to conclude that the adopted atmosphere has a temperature that is too low, particularly near the height 1300 km. At this height, a relatively small change in temperature can cause a large change in  $B_\nu$ , the Planck function, and a similarly large change in the line source function. We therefore made some calculations using a modification of the HSRA, in which the temperature has been increased by up to  $700^\circ$  near 1300 km. In Figure 26, we plot  $T_e$ ,  $N_e$ ,  $N_{HI}$ , and  $N_H$  for this model, as well as for the standard HSRA model for case 2.

Our new model atmosphere is not truly self-consistent, in that we have not computed a new hydrostatic equilibrium atmosphere but have simply increased  $T_e$  at certain heights. This avoids certain problems in the comparison between various models, but of course a complete study would require the recalculation of a new atmosphere for each temperature distribution.

It should be noted that a temperature increase of this magnitude is incompatible with the microwave observations plotted by Gingerich et al. (1971, their Figure 2). The HSRA predicts an intensity curve that goes through the tops of the microwave intensity error bars, and a  $700^\circ$  increase would raise the predicted curve even more. Using a self-consistent atmosphere in hydrostatic and ionization equilibrium would not improve the agreement, since although the temperature increase would be smaller, the increased electron densities would cause radiation at a given wavelength to be emitted at a higher point in the atmosphere, so the intensity increase would probably correspond to at least  $500^\circ$ . Probably only a two-component atmosphere can produce good agreement with both the ultraviolet and the radio observations.

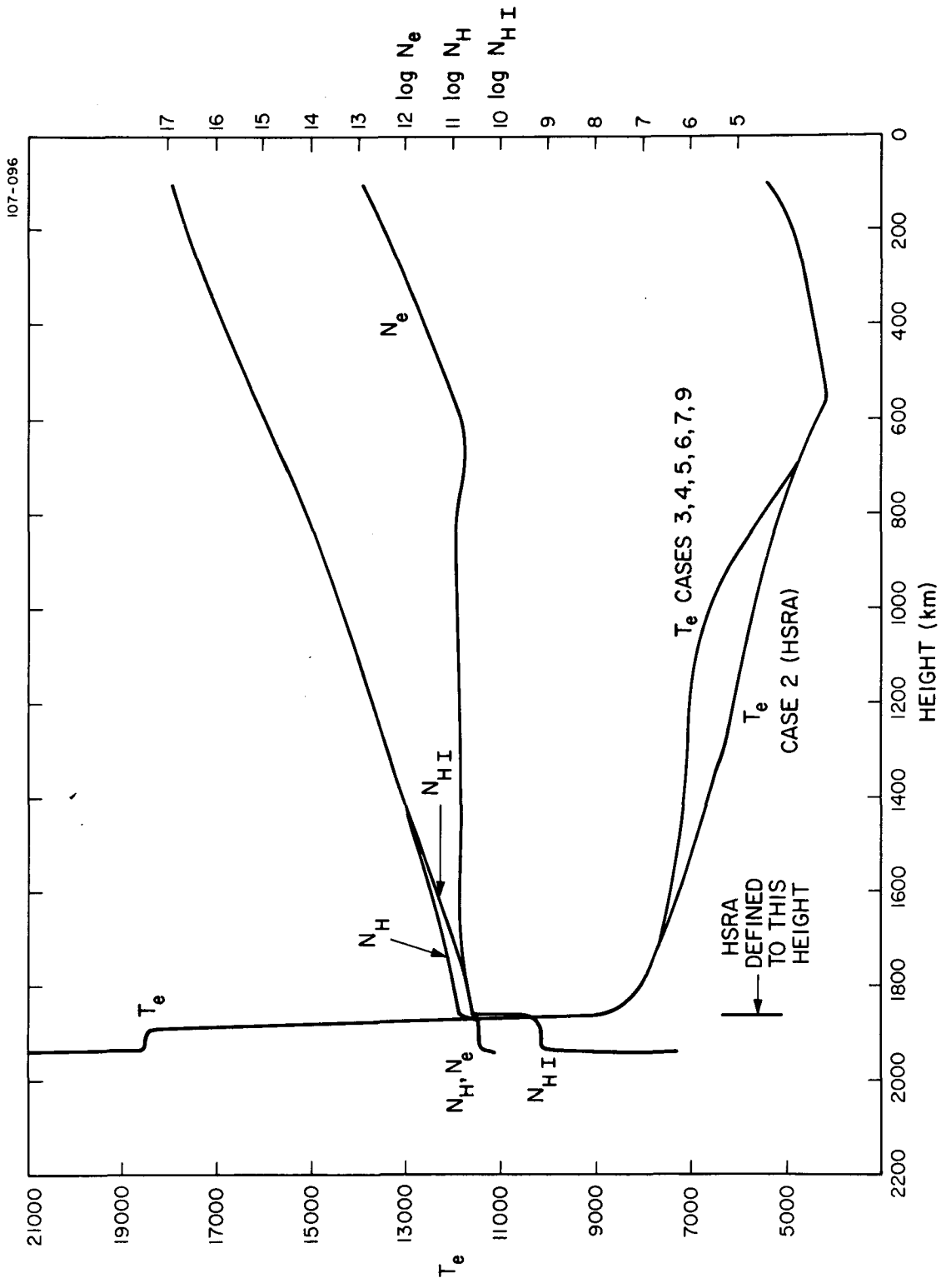


Figure 26. Model atmospheres for cases 2, 3, 4, 5, 6, 7, and 9.

In our cases 1 and 2, note that the maximum in the line profile for  $\mu = 1.0$  occurs at  $\Delta\lambda = 0.065$ , whereas the observed maximum occurs at approximately  $\Delta\lambda = 0.050$ . In order to improve the agreement with this quantity, we have found it necessary to reduce the microturbulent velocity, especially near 1000 to 1300 km. In Figure 28, we also plot the velocities used in case 3, along with an indication of those in case 2. The values of CE 5-1 and CVW 5-1 used for case 3 were the same as for case 2.

This change in the atmospheric model does in fact increase the source function significantly. The maximum near 1200 km becomes  $3.0 \times 10^{-9}$ , an increase by a factor 6.7 above case 2. In Figure 27, we show the profiles of  $\lambda 1302$  for this case. The computed intensity at  $\mu = 1.0$  is 298, while at  $\mu = 0.3$ , we compute an intensity of 445, as compared with Dupree and Reeves' (1971) value of 398. From an inspection of Figure 27, we can see that in this case the brightening of  $\lambda 1302$  toward the limb is due to a broadening of the distance between the two emission peaks, which accounts for an increase of approximately 10%, and to the great increase in strength of the wings of the line. Even for the very large Van der Waals broadening constant that we have used in this case, our computed strength of the line wings at  $\mu = 1.0$  is too low. Our total line intensity is reasonably close to the observed value, so we feel this is a better approximation to the solar temperature distribution than that given by the HSRA. The limb-brightening parameter is computed to be 1.20 for the  $\lambda 1302$  line alone.

Case 4. Clearly, the profiles of case 3 show too much central absorption. One way of improving the ratio of central to peak intensity is to hypothesize the existence of a region of very high microturbulent velocity, which falls around 1800 km, where the line source function is lower than its peak value around 1100 km. We therefore computed one case in which we used such a velocity distribution, which rises to  $9 \text{ km sec}^{-1}$  at 1800 km and decreases toward greater and lesser heights. We have plotted this velocity curve in Figure 28. Except for this change, all other parameters are the same as for case 3.

This change does indeed alter the line profiles, although the difference is not very great. In Figure 27, we show the line profiles at  $\mu = 1.0$  and

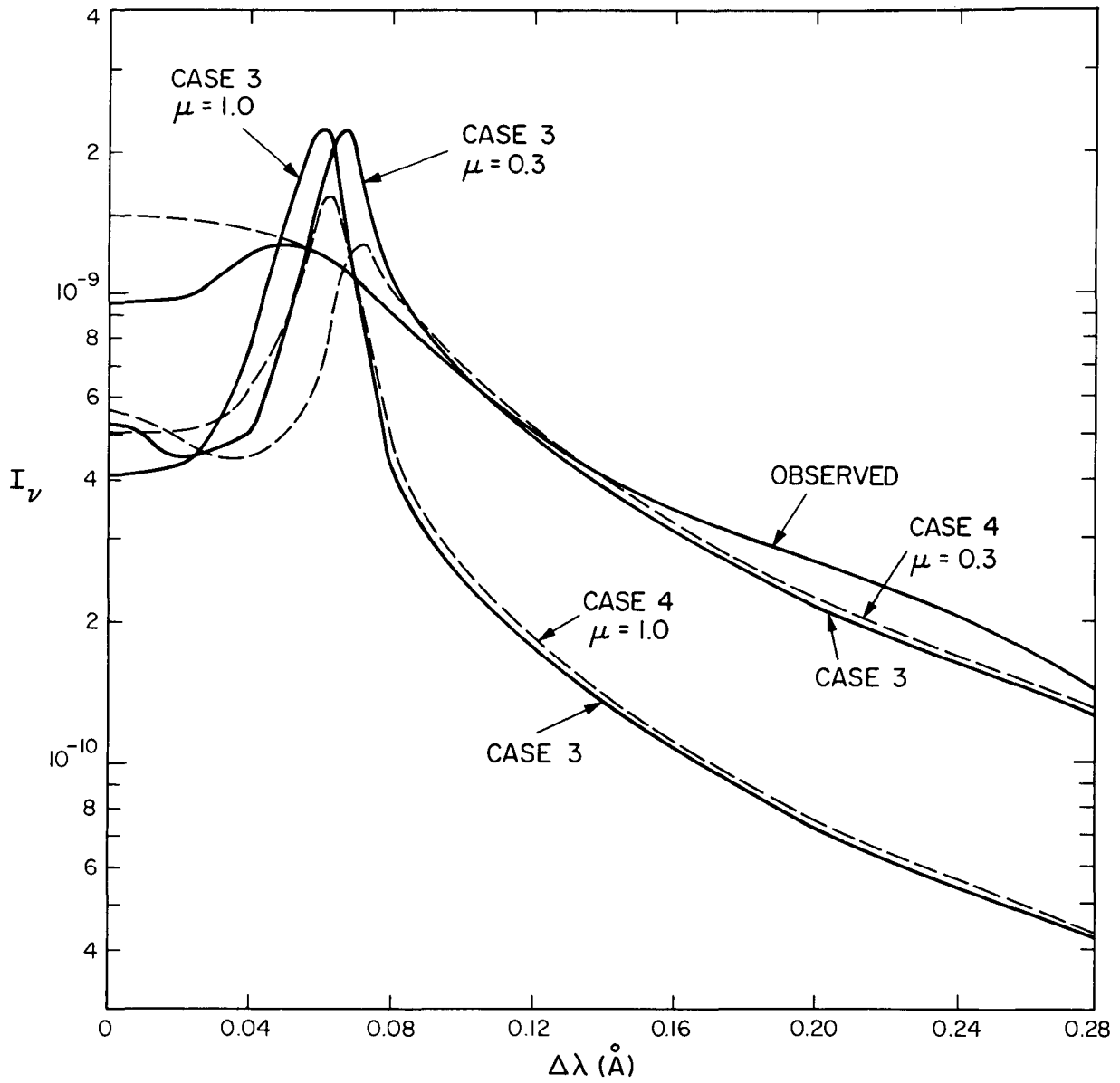


Figure 27. Profiles of  $\lambda 1302$  at  $\mu = 0.1$  and  $0.3$  for cases 3 and 4.

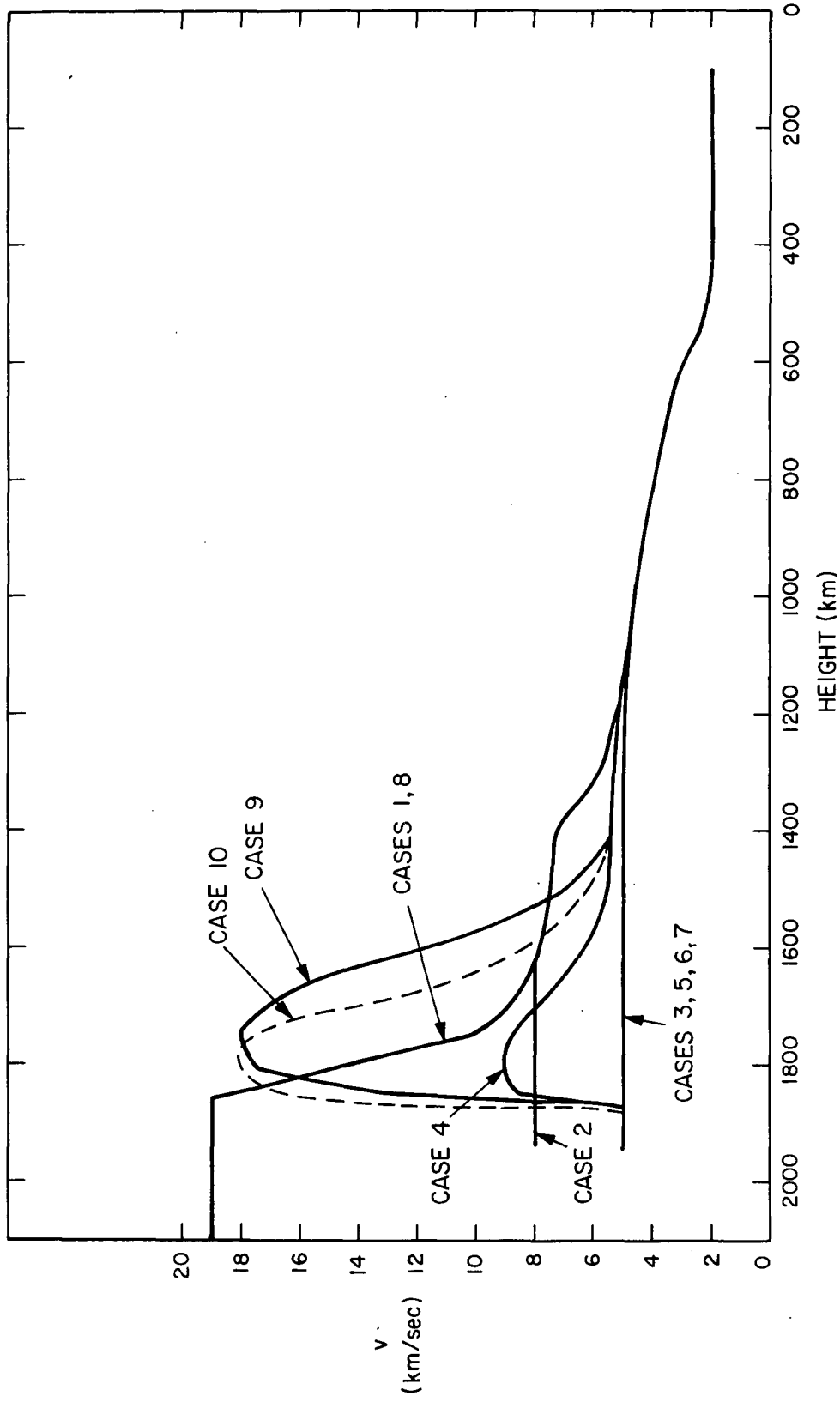


Figure 28. Microturbulent velocity versus height for various models.

$\mu = 0.3$ . The central intensities are increased over case 3 by about 25%, and the peak intensities are decreased by a similar amount. The peak/center ratio at  $\mu = 1.0$  is decreased from 5.5 for case 3 to 3.2 for case 4. Nevertheless, the agreement with observation is still unsatisfactory. Apparently, more emission by the chromospheric plateau, or a microturbulent velocity around 1800 km somewhat greater than  $9 \text{ km sec}^{-1}$ , or both are required to reconcile theory with observation. The intensity of the  $\lambda 1302$  line at  $\mu = 1.0$  for case 4 is computed to be 290, while the limb-brightening parameter is 1.07. We thus see that this microturbulent-velocity distribution considerably reduces the amount of limb brightening.

Case 5. Cases 5, 6, and 7 are closely related, in that they use exactly the same atmospheric model and almost identical atomic constants. In these cases, we have varied the rate of recombination to the ground state of O I, and thus the amount of neutral oxygen in the plateau region, in order to investigate the effects of different amounts of emission in the chromospheric plateau.

For case 5, we used an atmospheric model much like that of cases 3 and 4; the temperatures near 1100 km are slightly different, as shown in Figure 26. We used a six-level model atom, in which we include all three of the O I resonance lines. The atomic constants used are those tabulated in Table 2, with the exception of the following:

As in cases 2, 3, and 4, we continued to use  $\text{CE } 6-1 = 1.34 \times 10^{-7}$ . Note that  $\text{CE } 6-3 = \text{CE } 6-2 = \text{CE } 6-1$ . We also continued to use  $\text{CVW} = 1.0 \times 10^{-4}$  in all three resonance lines. For case 5, we use recombination rates computed directly from the photoionization cross sections of Figure 21, neglecting effects of the resonance reaction with hydrogen, and neglecting any dielectronic recombination effects. This choice results in a very high fractional ionization in the plateau, approximately 0.998, and consequently a small amount of emission in the plateau, and a plateau optical depth in  $\lambda 1302$  of only  $2 \times 10^{-3}$ . In Figure 29, we have plotted the profile of the  $\lambda 1302$  line at  $\mu = 1.0$ . The intensities of the three lines at  $\mu = 1$  are tabulated in Table 4.

Case 5 is very similar to case 3, the differences being caused almost entirely by the effects of the two lines that have been added to the calculation.

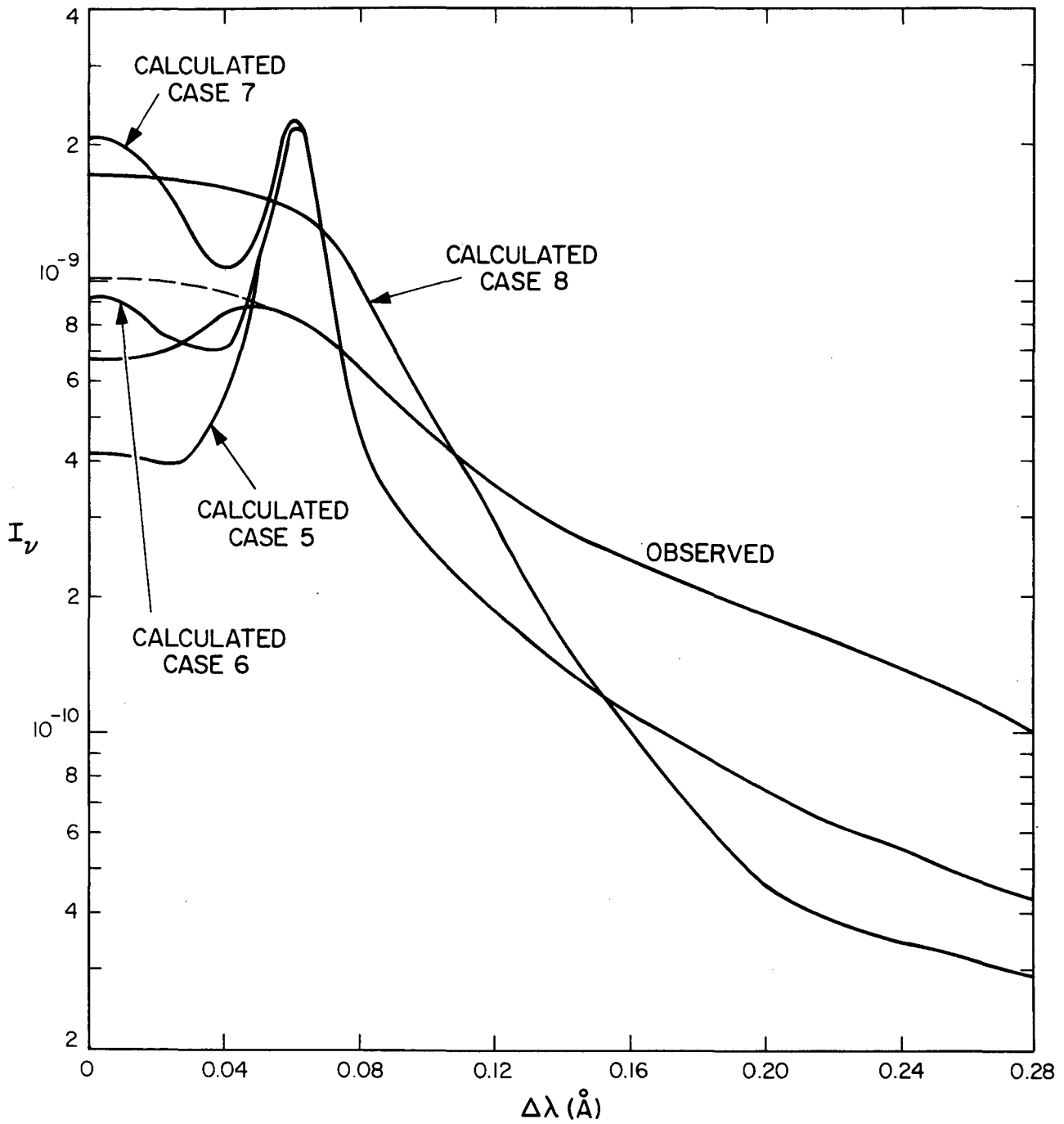


Figure 29.  $\lambda 1302$  profiles for four cases at  $\mu = 1.0$ .

Table 4. Intensities and limb brightening for the O I calculations.

Case	$\lambda 1302$ $\mu = 1$	$\frac{\text{Intensity}}{\lambda 1304}$ $\mu = 1$	$\lambda 1306$ $\mu = 1$	$\frac{\lambda 1304 + \lambda 1306}{\lambda 1302}$	$\lambda 1302$ limb brightening	$\lambda 1304 + \lambda 1306$ limb brightening
1	33	-	-	-	1.40	-
2	84	-	-	-	1.13	-
3	298	-	-	-	1.20	-
4	290	-	-	-	1.07	-
5	295	298	351	2.20	1.30	1.10
6	339	326	343	1.97	1.52	1.22
7	485	445	405	1.75	1.73	1.40
8	503	338	154	0.98	1.51	1.97
9	267	221	231	1.69	1.40	1.17
10	515	373	354	1.41	1.80	1.60
OSO 4	398	718		1.80	-	$\sim 1.18$

Case 6. For this case, we have increased the recombination rate to the ground state in the plateau by a factor 10 over case 5 and have thus considerably reduced the fractional ionization, which falls to 0.98. Similarly, the  $\lambda 1302$  optical depth in the plateau is increased to  $2.0 \times 10^{-2}$ , which is probably more realistic. Thus, we have more plateau emission than for case 5; in Figure 29, we plot the  $\lambda 1302$  profile at  $\mu = 1.0$ ; and in Figure 30, we plot the profiles of all three lines at  $\mu = 1.0$ . The source function is shown in Figure 31. Note the surprising fact that indeed the "weaker"  $\lambda 1304$  and  $\lambda 1306$  lines are more intense than  $\lambda 1302$ , at least in the line cores. This is apparently because the self-absorption of the central part of the line is stronger in  $\lambda 1302$ . Case 6 is a reasonably good fit to all the observations and is probably our most realistic model, excepting perhaps case 9 below.

Most of our calculations reported in this chapter were made with only two iterations on the radiative-transfer solution. For the cases that include only one line, this is quite sufficient for good convergence, but for the cases with three lines, we wished to check the effects of doing more iterations. For case 6, we did four iterations and found that the intensities of the  $\lambda 1304$  and  $\lambda 1306$  lines changed by up to 10% from the second to the fourth iteration, while the limb-brightening parameter increased by about 2%. Accuracy of this order is sufficient for our purposes, so we have not run four iterations in the other cases.

Case 7. This is similar to cases 5 and 6, but we have increased the recombination rate in the plateau by a factor four over case 6, and the chromospheric emission becomes very important. This case probably exaggerates the chromospheric emission; nevertheless, the line profiles are of some interest. In Figure 29, we show the  $\lambda 1302$  profile at  $\mu = 1.0$ , while in Table 4, we tabulate some data on intensities and limb brightening. Note that the limb brightening is much greater than is observed.

The source function for this case, and for case 5 as well, is almost identical with that for case 6, plotted in Figure 31. The amount of chromospheric plateau emission does not affect the source function very much, as the major effect is simply to change the optical depth as a function of height, near  $\tau = 10^{-2}$ .

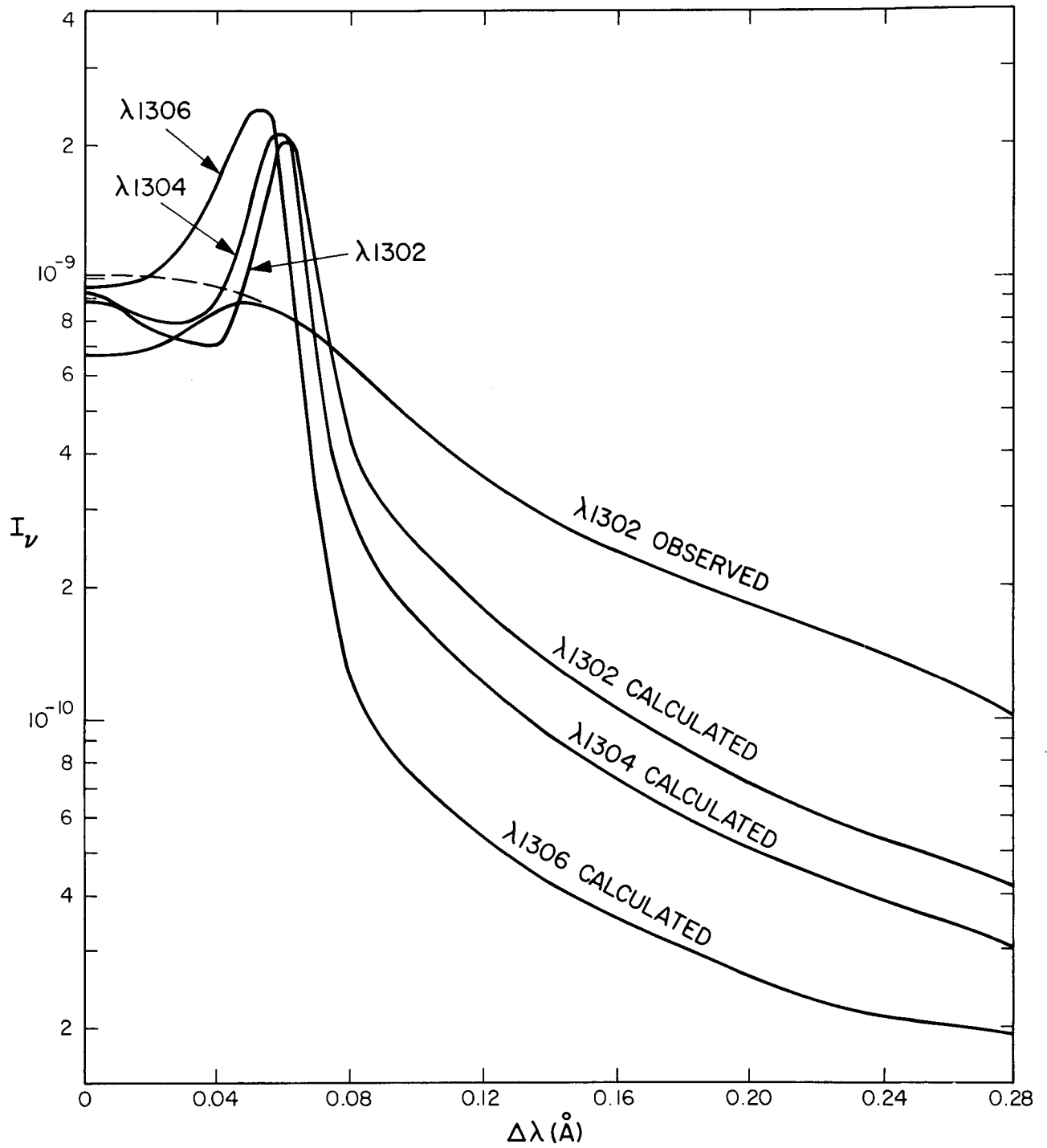


Figure 30. Profiles of the three O I resonance lines for case 6 at  $\mu = 1.0$ .

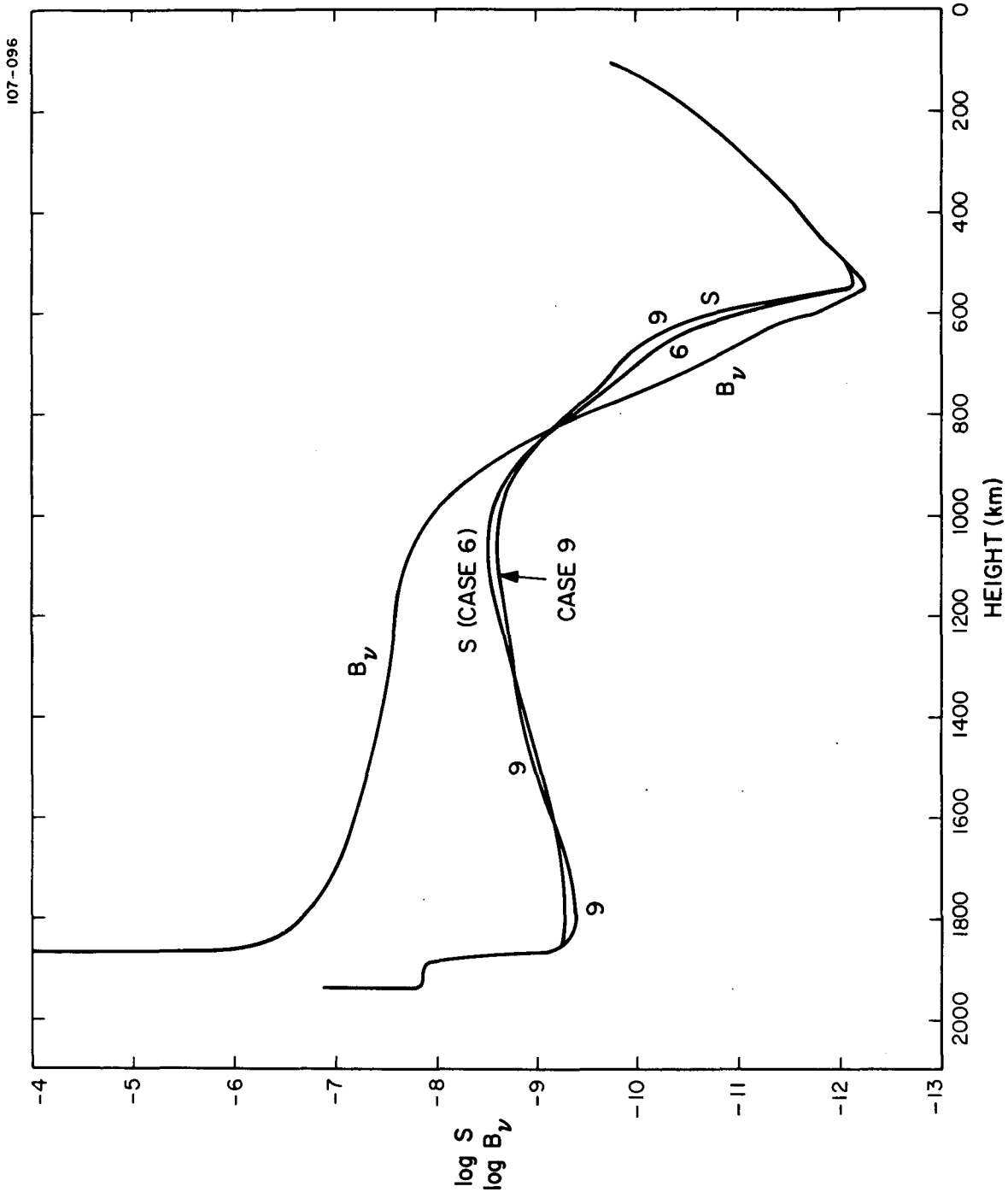


Figure 31. Source functions and Planck function versus height for two cases.

Case 8. This is a totally unrealistic case, which was included only to show the effects of extreme plateau emission. The recombination rate has been increased to the point where the fractional ionization is only about 0.60. As we can see from Table 4, in this case the line intensities approach the 5:3:1 ratio that we would expect for an optically thin gas. In Figure 29, we show the nonreversed  $\lambda 1302$  profile computed for this case, but we would not expect such profiles to appear on the quiet sun. The broadening is caused by a large microturbulent velocity, shown in Figure 28. In Figure 32, we have plotted the limb-brightening parameter in  $\lambda 1302$  versus that in the sum of  $\lambda 1304 + \lambda 1306$  for the five cases with increasing quantities of chromospheric emission. We can use this curve to estimate the limb brightening in  $\lambda 1304 + \lambda 1306$  for cases 1 to 4, having calculated that in  $\lambda 1302$ , and we find that cases 2, 3, and 4 show too little limb brightening.

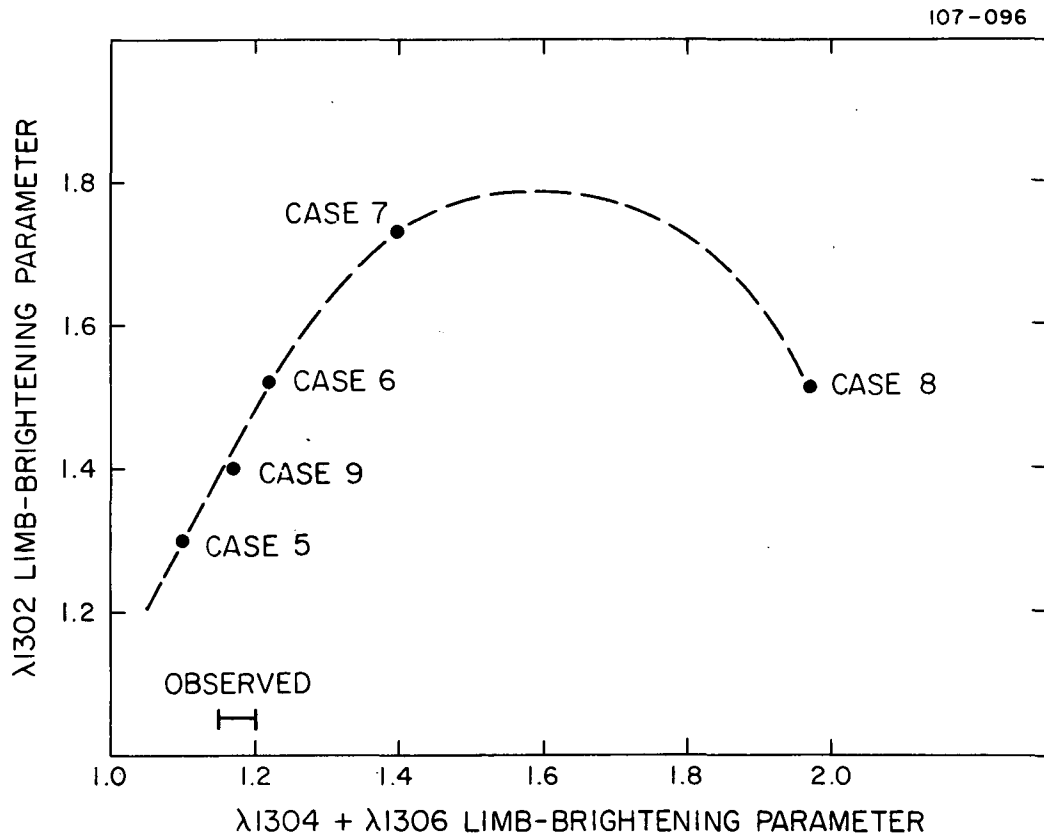


Figure 32. Limb-brightening parameters in various lines for five cases.

Case 9. In Section 6 and in the Appendix, we conclude that the micro-turbulent velocity could well reach values as high as  $18 \text{ km sec}^{-1}$  in the chromosphere. We therefore felt it might be instructive to make one run in which we have a very high microturbulent velocity in the height range 1500 to 1800 km, as shown by the curve in Figure 28. The other atmospheric quantities and the atomic constants are the same as for case 6, except that we have multiplied the plateau recombination by a factor 1.5 over that of case 6, in order to improve the agreement of the limb brightening and the line profiles. In Figure 33, we show the profiles of the three lines at  $\mu = 1.0$  for case 9, and we tabulate the other data in Table 4. In Figure 20, we show the limb-brightening curve for this case. The source function, shown in Figure 31, is very similar to that of cases 5, 6, and 7.

This case shows the best agreement of all with the observations, although the absolute intensities are slightly low. The degree of central reversal is very different for the three lines, varying from strong central emission in  $\lambda 1302$ , to weaker central emission in  $\lambda 1304$ , to central absorption in  $\lambda 1306$ .

Case 10. In cases 1 through 9 we have used A values for the O I triplet based on the results of Parkes et al. (1967). More recently, Lawrence (1969) has shown that the f value for this transition is 0.046, rather than 0.021 as found by Parkes et al. We have made calculations for one case, similar to case 9, in which we have used the new, higher A values and correspondingly higher radiative damping. In order to produce acceptable profiles, we must also use a different microturbulent velocity distribution, which we show in Figure 28. This velocity variation is very similar to the one we finally adopted for Mg II (Figure 15, cases 2 and 3). The profiles for the three lines at  $\mu = 1.0$  are plotted in Figure 34, and the intensity and limb-brightening data are tabulated in Table 4. Note that the intensities are slightly higher than observed, while the limb brightening is considerably too great. Apparently the emission calculated from the chromospheric plateau is somewhat too large, and the increase in microturbulent velocity should be placed at a height greater by approximately 40 km. These changes would improve the agreement of the  $\lambda 1302$  peak separation, the limb brightening, and the intensities.

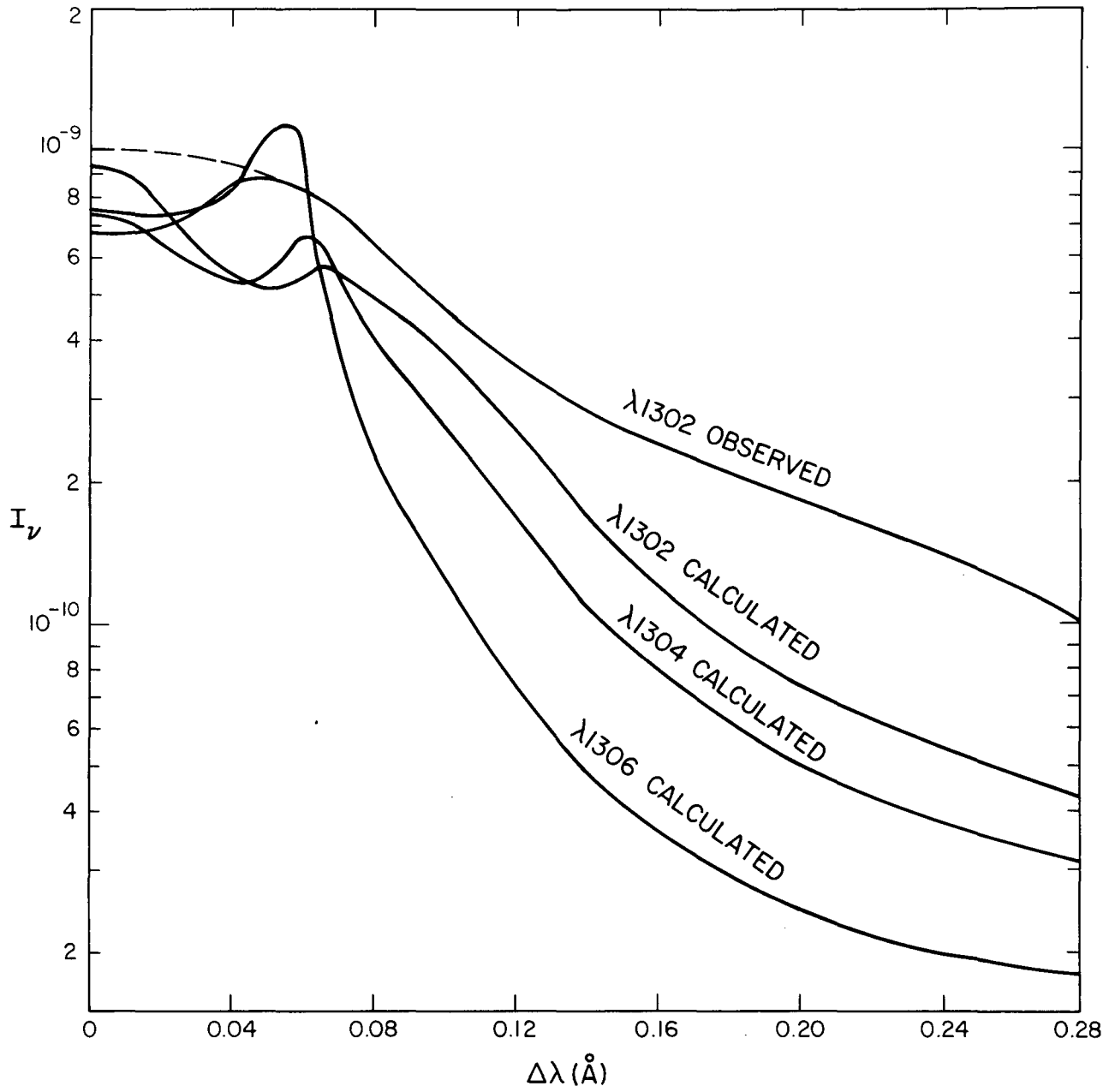


Figure 33. Profiles of the three O I resonance lines at  $\mu = 1.0$  for case 9.

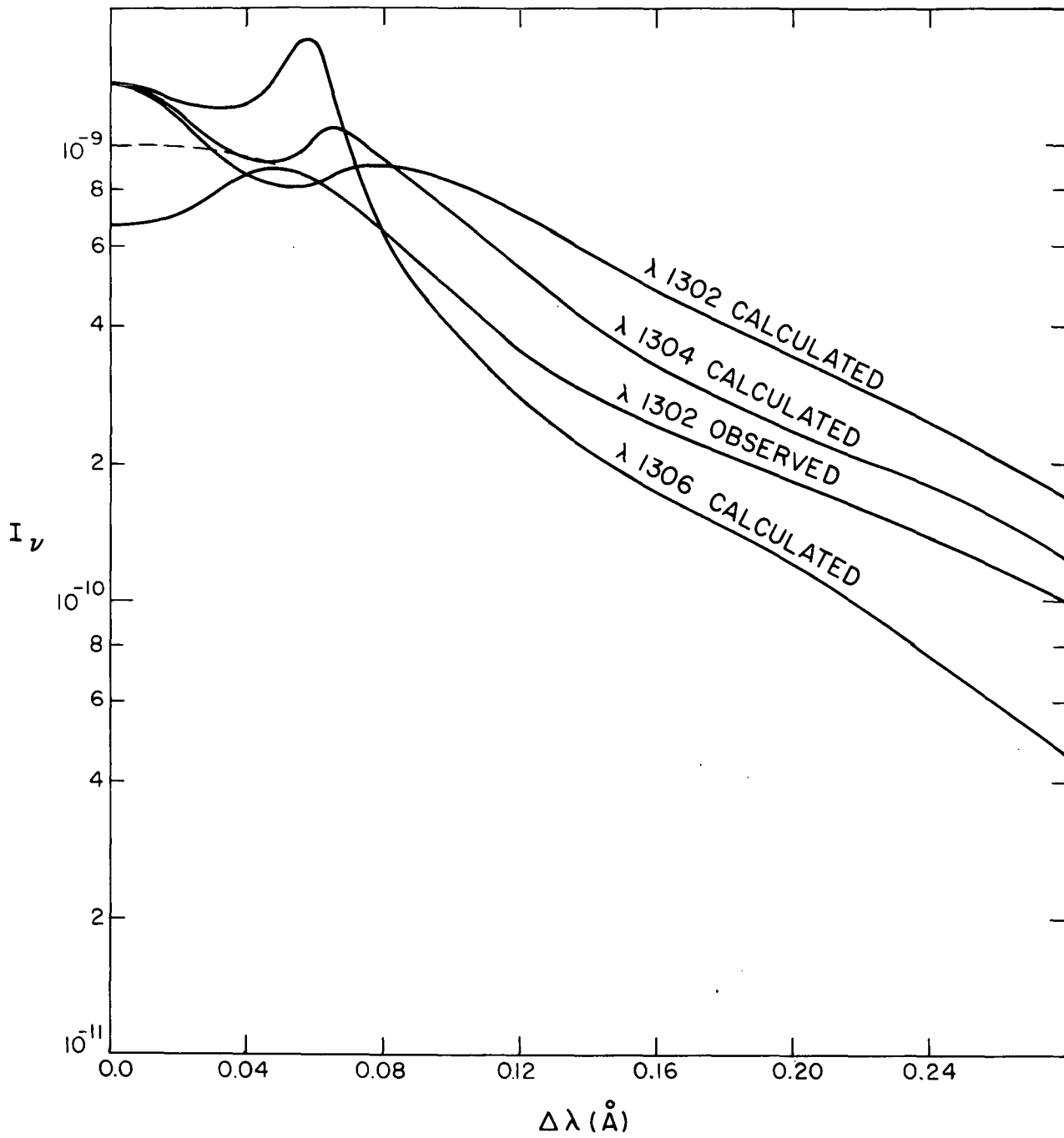


Figure 34. Profiles of the three O I resonance lines at  $\mu = 1.0$  for case 10.

In summary, we must conclude that the temperature of the HSRA is too low by about  $500^\circ$  in the region near 1100 km. A rapid increase in micro-turbulent velocity occurs near 1500 km, and velocities near  $18 \text{ km sec}^{-1}$  are reached. The chromospheric plateau emits an observable, but not dominant, amount of radiation in the resonance lines of O I, especially the  $\lambda 1302$  line.

## 6. THE CARBON II RESONANCE LINES

6.1 Introduction

The resonance lines of C II at 1334.52 and 1335.69 Å (hereafter called  $\lambda$  1334 and  $\lambda$  1336) are among the strongest in the solar ultraviolet spectrum. There are actually three lines in the multiplet, caused by transitions between the  $2s^2 2p^2 P^{\circ}_{1/2, 3/2}$  ground state and the  $2s 2p^2 D_{3/2, 5/2}$  excited state, but the  $^2P^{\circ}_{3/2} - ^2D_{3/2}$  line is less than 20% as strong as the other two and is masked by the almost coincident  $^2P^{\circ}_{3/2} - ^2D_{5/2}$  line. In Figure 35, we show a term diagram for the lowest lying levels of C II (Moore, 1949).

The C II lines are formed in that part of the solar chromosphere where C II is most abundant and the lines are most easily excited — that is, between 10,000 and 25,000°. We have tried to determine the structure of the solar atmosphere within this temperature range by matching all the observed characteristics of the C II lines with the results of our theoretical calculations.

In our atmospheres, described in Section 6.4, we specify electron temperature, electron density, total hydrogen density, neutral-hydrogen density, and microturbulent velocity as functions of physical height. Our models are not altogether self-consistent in terms of hydrostatic equilibrium and hydrogen ionization equilibrium but are rather a fitting of a model of the chromosphere-corona transition region onto the top of a model of the photosphere and chromosphere.

6.2 The Observations

We have chosen to divide into four classes the observational data that refer to the C II lines. These are (1) total absolute intensity integrated in wavelength over the two lines, (2) the ratio of integrated intensities of the two separate lines, (3) the profile of each line, and (4) the limb-brightening curve of the two combined lines.

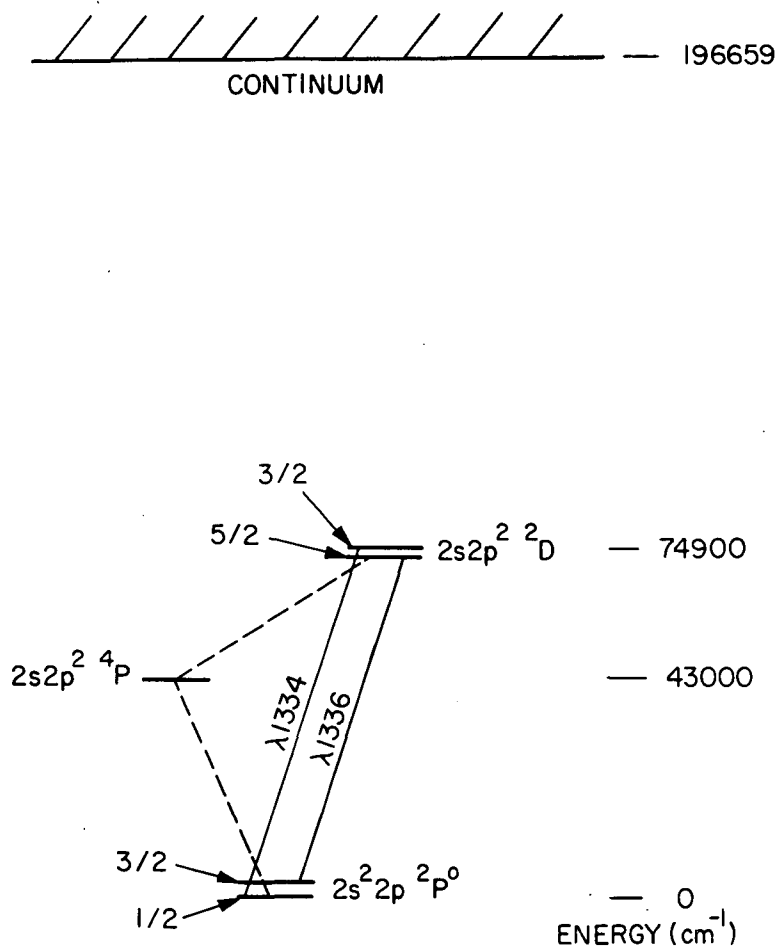


Figure 35. C II energy levels.

(1) The intensity of the C II lines was first measured by Detwiler, Garrett, Purcell, and Tousey (1961) as  $0.1 \text{ erg cm}^{-2} \text{ sec}^{-1}$  at the earth. A study by Dupree, based on measurements made photoelectrically by the Harvard experiment on OSO 4, gives the slightly lower value of  $0.071 \text{ erg cm}^{-2} \text{ sec}^{-1}$  at the earth, which can be expressed as  $1.03 \times 10^3 \text{ ergs cm}^{-2} \text{ sec}^{-1} \text{ ster}^{-1}$  at the solar surface at the disk center. The OSO 4 experiment was calibrated before launch, by comparison with a series of rocket spectra (see Reeves and Parkinson, 1970b). Dupree and Reeves estimate that the absolute intensities of the solar emission lines in this spectral region are accurate to within about a factor of two. We will adopt Dupree and Reeves' value.

(2) Detwiler et al. gave equal fluxes for the two C II lines. The rocket spectra of Berger, Bruner, and Stevens (1970) yield a ratio  $\lambda 1334/\lambda 1336$  of 1.02. However, a detailed analysis of the Harvard OSO 4 spectra by J. Vernazza (1971, private communication) gives a value of 0.73. As we show below, we are able theoretically to derive ratios of this quantity up to about 0.84, but no higher. Owing to the uncertainty in the observations, we do not try to match any specific value for this quantity.

(3) The profiles of the C II lines have been measured by Berger et al. (1970). In Figure 36, we plot the observed profiles of both wings of the  $\lambda 1334$  line as well as a typical theoretical profile. The curves have been normalized at the centers to produce a best fit, so agreement depends mainly on our choice of microturbulent velocities and on the fact that both shapes are close to gaussian. For this reason, all our theoretical profiles are virtually the same.

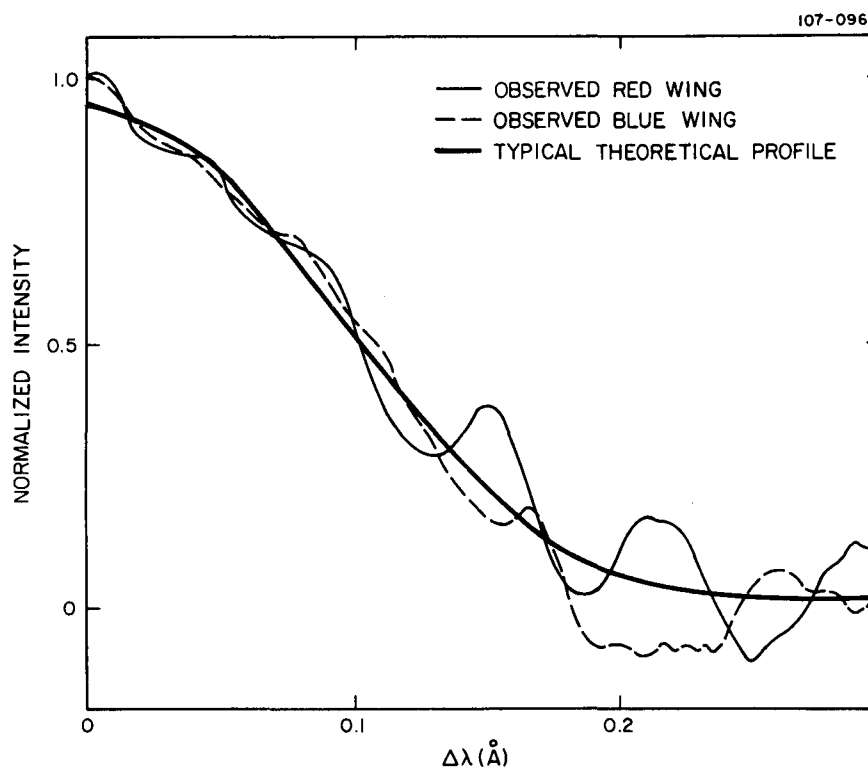


Figure 36. C II  $\lambda 1334$  profiles.

(4) By the method described by Withbroe (1970b), an average limb-brightening curve for the "quiet sun" was derived from data obtained by the Harvard OSO 4 experiment. Almost all points on the C II  $\lambda$  1335 spectroheliograms lying between  $\pm 10^\circ$  solar latitude were used. A few points were rejected after an inspection of the spectroheliograms, because it was judged that these points were affected by active regions that extended to within the  $\pm 10^\circ$  equatorial belt. The derived limb-brightening curve is shown by the filled circles on Figure 37. The noise in the observed data corresponds partially to the fact that a variable number of data points, from 5 to 50, were averaged for each point on Figure 37. We also plot in Figure 37 the limb-brightening curves calculated for two theoretical models. These two theoretical curves have maximum values of 1.35 and 1.38, which we feel closely represents an optimum fit to the observations. In what follows, we shall use the term "limb-brightening parameter" to mean the maximum of the theoretical limb-brightening curve for a given model, for the two lines combined. The OSO 4 C II spectroheliograms include radiation both from the lines and from the underlying continuum. Using the spectra of OSO 6, we determined that the continuum contributes only 3 to 4% of the total measured intensity and that the continuum does not show marked limb brightening or darkening. So our C II curves should not be noticeably affected by the problem. The spatial resolution of the instrument was 1 arcmin, which limits the sharpness of the observed limb-brightening curve near the limb of the sun. As in Section 7, our theoretical limb-brightening curves include a correction for the effects of the finite spatial resolution of the OSO 4 instrument.

We desired to obtain a new limb-brightening curve from the Harvard experiment on OSO 6. However, the much higher level of solar activity during the lifetime of OSO 6, combined with the fact that solar active regions had approached closer to the solar equator than during the lifetime of OSO 4, made our previous methods for deriving limb-brightening curves inapplicable. A new type of data was now available, in the form of spectra taken at several points across the solar disk. These points were especially chosen, from almost simultaneous spectroheliograms in the O VI  $\lambda$  1032 line, to be as free from activity as possible. By the use of these spectra, we hoped to produce a limb-brightening curve for which the continuum near the C II lines had been subtracted, so that the actual C II line limb brightening could be derived directly.

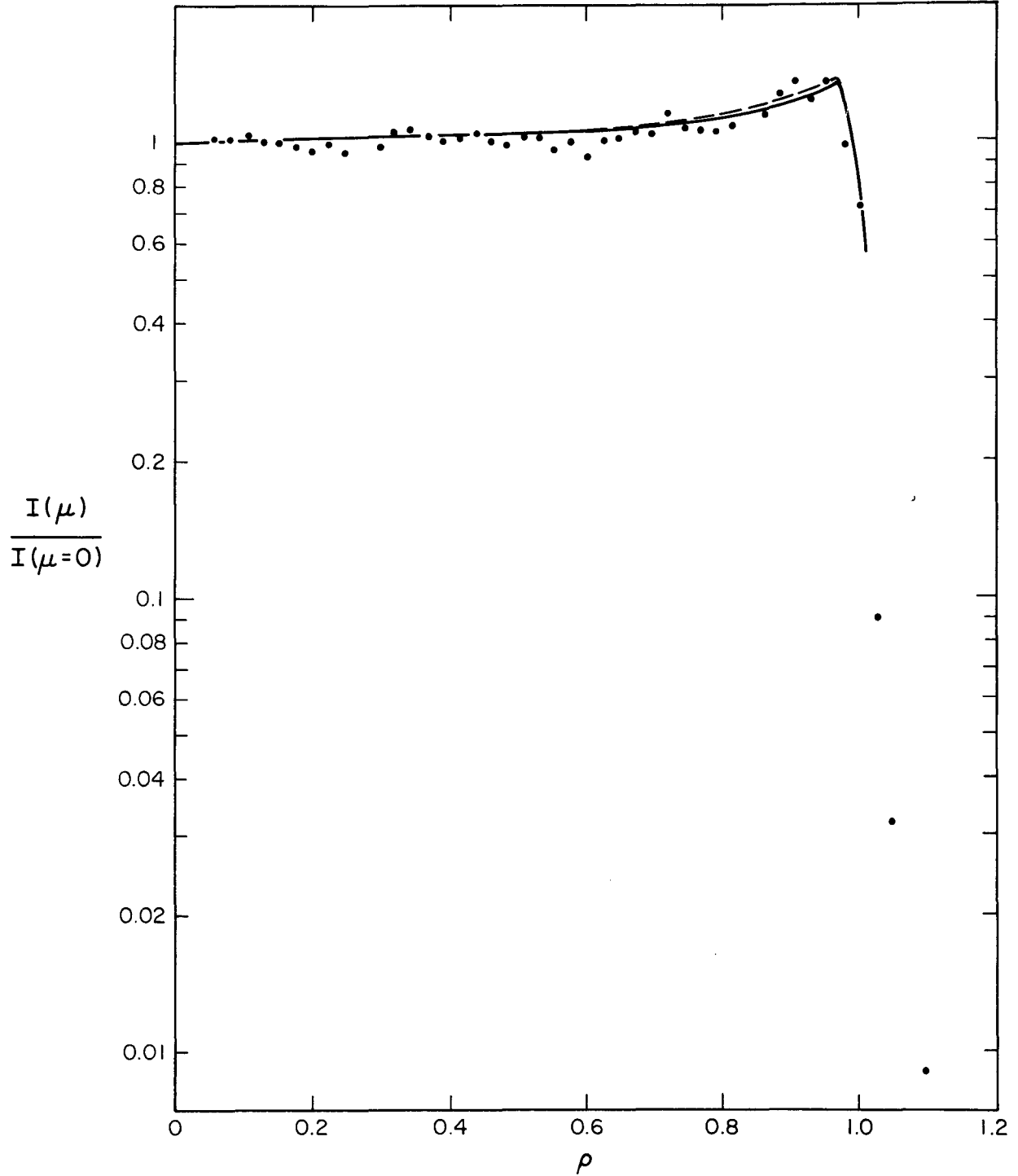


Figure 37. Observed limb brightening and two representative theoretical curves.

An inspection of the spectra showed that even the points that had been chosen to be free from activity were not really so, especially near the limb. This fact could be seen by an inspection of the intensities of some optically thin lines, such as O VI  $\lambda$  1032 or N III  $\lambda$  991, at various values of  $\mu$  across the disk. If in fact the spectra had been made at quiet regions of the sun, we would expect a  $1/\mu$  intensity variation of these lines. The lines  $\lambda$  1032 and  $\lambda$  991 actually increase in intensity considerably more rapidly than  $1/\mu$  toward the solar limb, so we must find some means of correcting for the effects of active regions in the line of sight.

Our first approach was to assume that all lines were enhanced by the same factor, owing to the effects of active regions. Thus, one should multiply the C II line intensity by a factor that brings some optically thin line, such as O VI  $\lambda$  1032, down onto a  $1/\mu$  limb-brightening curve. This was done, but the correction factors were such that the resulting curve for C II showed considerable limb darkening, which was in unacceptably poor agreement with the OSO 4 results.

Our next approach was to assume that the enhancement in the various lines was not equal but that for each line it was proportional to the active region/quiet region intensity ratios found by Noyes, Withbroe, and Kirschner (1970). They found  $I_A/I_Q$  to be

C II $\lambda$ 1334	4.60,
O VI $\lambda$ 1032	6.30,
N III $\lambda$ 991	5.25.

For an optically thin line (say,  $\lambda$  1032), let us denote the observed intensity at radius  $\rho$  by  $I_{1032}(\rho)$  and the intensity according to a  $1/\mu$  brightening law (assuming that we have some spectra from truly quiet regions near  $\rho = 0.0$ ) by  $I_{1032}(\rho_1/\mu)$ . Then we assume that

$$I_{1032}(\rho) = I_{1032}(\rho_1/\mu) (1 + 5.30 q) \quad , \quad (142)$$

where  $q$  gives an active-area fraction, ranging from 0 for quiet regions to 1 for the case of active regions covering the whole spatial-resolution element

of the spectrometer. The parameter  $q$  may vary somewhat more than this, owing to the scatter of the data points. In analogy with equation (142), we should also have

$$I_{1334}(\rho) = I_{1334}(\rho_Q) (1 + 3.60 q) \quad , \quad (143)$$

where  $I_{1334}(\rho_Q)$  is the desired  $\lambda 1334$  limb-brightening value for quiet regions. In practice, the smallest value of  $\rho$  for which we had spectra was  $\rho = 0.343$ , corresponding to  $\mu = 0.939$ . We assumed that the C II curve was essentially flat out to this point and that the N III and O VI curves had risen to 1.12 times their value at  $\mu = 1.0$ , corresponding to a  $1/\mu$  brightening law. Then equation (142) can be solved for  $q$ , and the desired  $I_{1334}(\rho_Q)$  determined from equation (143).

We can derive two partially independent C II limb-brightening curves by comparison of C II intensities with those of N III and O VI, respectively. These curves are shown in Figure 38.

Another method of normalization of the spectra is illustrated in Figure 39. The small dots were determined by simply using the intensity at  $\lambda 909$ , a point near the head of the Lyman continuum that shows a relatively flat limb-brightening curve, as a standard intensity. That is, the points plotted are simply  $[I_{1334}(\rho)/I_{909}(\rho)]$  for each spectrum used. In order to eliminate, insofar as possible, the effects of active regions, the available spectra were divided into categories according to the intensity in the C II line. Spectra of intensity above a certain value were considered to be contaminated by active regions and were not used.

Note that the scatter of the points from the OSO 6 spectra is considerably greater than that of the OSO 4 spectroheliogram points. This is primarily due to the fact that the OSO 4 points have already been averaged, and each OSO 4 point plotted is an average of between 5 and 50 original data points. But near the limb ( $\rho = 1.0$ ), the OSO 6 points normalized through  $\lambda 991$  and  $\lambda 1032$  seem to show definite limb darkening, and in fact the darkening is greater when we

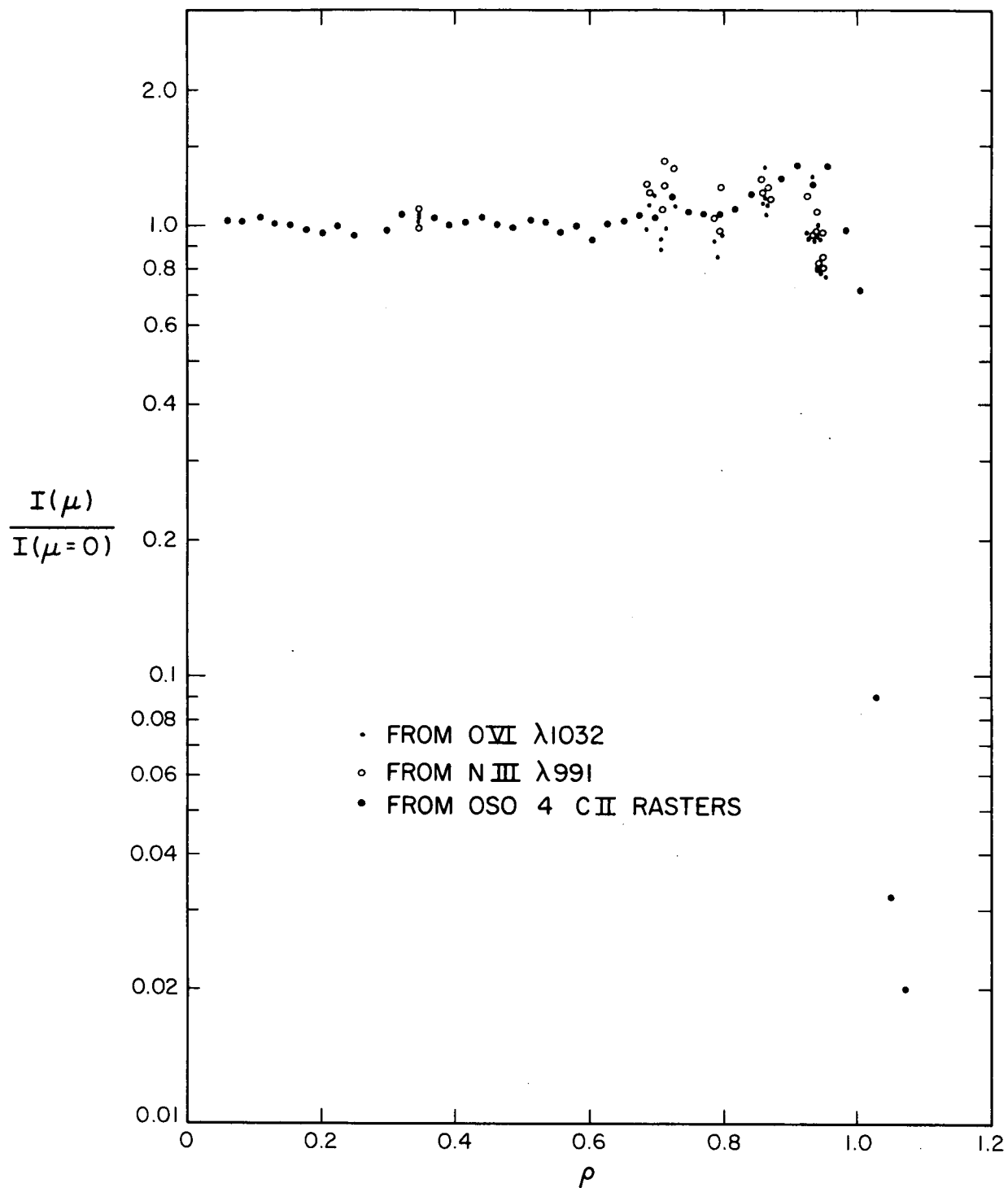


Figure 38. Normalization of the OSO 6 C II limb-brightening curve by means of O VI  $\lambda 1032$  or N III  $\lambda 991$ .

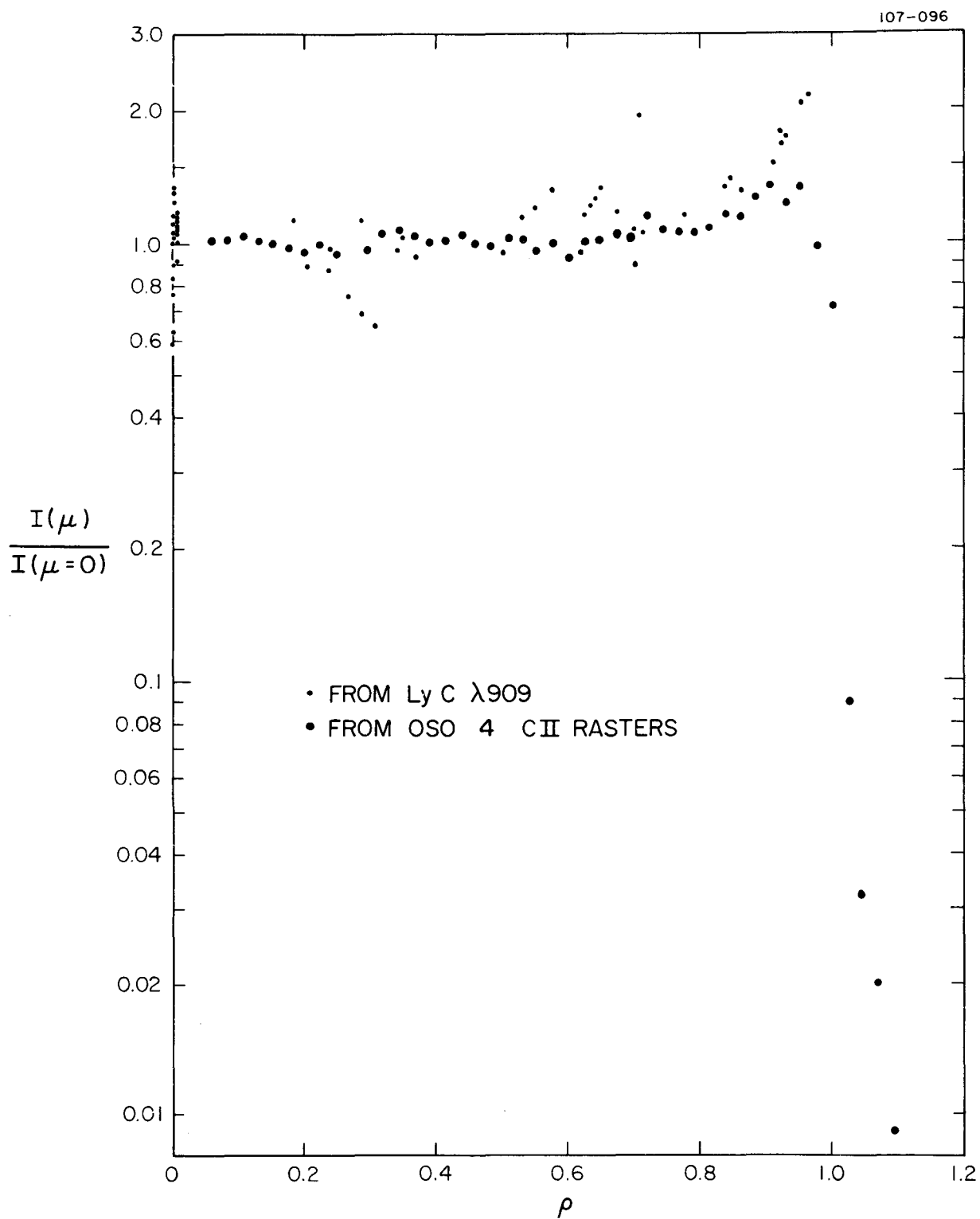


Figure 39. Normalization of the OSO 6 C II limb-brightening curve by means of the Lyman continuum  $\lambda$  909.

normalized by  $\lambda 1032$ , while the points normalized at  $\lambda 909$  show strong limb brightening. This is clearly an artifact of our method of data reduction and would lead one to give more weight to the limb-brightening curve derived from the OSO 4 data than to either of the curves derived from the OSO 6 spectra.

### 6.3 Atomic Data and C I Ionization

It was decided to use a five-level model C II atom, consisting of the two  $^2P^o$  ground-state levels, the  $^4P$  state considered as one level, and the two  $^2D$  levels, plus a continuum. We shall discuss first the various atomic collisional and radiative rates that must be specified and then the models of the solar atmosphere for which calculations were made. The atomic parameters are tabulated in Table 5, for which an explanation follows.

We have numbered the five levels with the numbers in parentheses after the level designations. In the table, we have used the convention of giving exponents in parentheses.

The A values have been adopted from the experimental results of Lawrence and Savage (1966). We have shown in parentheses the A 5-2 value that we would obtain by using the ratio of A values within the multiplet as tabulated by Wiese *et al.* (1966). For our actual calculations, we have omitted radiative transitions from level 5 to level 2, since this line is weak and heavily blended with the 4-2 line. The radiative and Van der Waals broadening half-widths have been calculated according to equations (137) and (139), respectively. These quantities appear not to be critical for the C II lines, since the lines are not very optically thick and Doppler broadening dominates.

For the collisional transition rates between levels 1 and 5 and between levels 2 and 4, we have used the general formula of Van Regemorter (1962). We have expressed the rates in terms of the quantity CE I-J, defined by equation (127). The parameter CE I-J is weakly temperature dependent, and we have given values for  $T_e = 15,000^\circ$ . The rate of collisional excitation

Table 5. Atomic data for C II.  
(Rates tabulated for  $T_e = 15,000^\circ$ .)

Upper level					
	$^2P_{3/2}^o(2)$	$^4P(3)$	$^2D_{5/2}(4)$	$^2D_{3/2}(5)$	Continuum
$^2P_{1/2}^o(1)$	CE = 5.60 (-8)	CE = 1.18 (-8)	CE = 0	CE = 3.43 (-8)	CI = 5.43 (-9)
				A = 2.13 (+8)	$\alpha = 2.54$ (-18)
				CRD = 1.4 (-5)	
				CVW = 4.0 (-5)	
			CSK = 0		
$^2P_{3/2}^o(2)$		CE = 1.18 (-8)	CE = 3.43 (-8)	CE = 0	CI = 5.43 (-9)
			A = 2.84 (+8)	[A = 4.73 (+7)]	$\alpha = 2.54$ (-18)
			CRD = 1.5 (-5)		
			CVW = 4.0 (-5)		
			CSK = 0		
$^4P(3)$			CE = 3.53 (-9)	CE = 2.37 (-9)	CI = 1.77 (-8)
					$\alpha = 1.0$ (-18)
$^2D_{5/2}(4)$				CE = 1.90 (-8)	CI = 2.80 (-8)
					$\alpha = 1.0$ (-18)
$^2D_{3/2}(5)$					CI = 2.80 (-8)
					$\alpha = 1.0$ (-18)

via the optically forbidden or weak 5-2 and 4-1 transitions should be much smaller than via the allowed transitions, so we have set the 5-2 and 4-1 cross sections equal to zero.

No published detailed calculations of the cross sections for collisional transitions between the  $^4\text{P}$  state and the  $^2\text{P}$  and  $^2\text{D}$  levels have been made. As an estimate, we have simply used the same collision strength found by Osterbrock (1970) for the somewhat similar intersystem line  $\lambda 1909$  in C III. We find that excitation via the  $^4\text{P}$  level contributes 0.10 to 0.20 of the total line excitation.

The collisional transition rates for the fine-structure transitions 2-1 and 5-4 have been computed from the formulas of Bahcall and Wolf (1968). We have chosen a collision strength between the  $^2\text{D}$  levels equal to that between the  $^2\text{P}$  levels. At temperatures above about  $9000^\circ$ , transitions due to electron collisions are the most important, with proton collisions smaller by about a factor of 3. For temperatures below  $9000^\circ$ , neutral-hydrogen-atom collisions become important. All three processes have been taken into account in our calculations, although we express the rates in terms of the electron-number densities. Bely and Faucher (1970) have derived proton-collision cross sections between the ground-state levels about four times greater than those that we used. If this factor holds true for electron collisions as well, then the fine-structure transition rates could be significantly increased. Wofsy et al. (1971) have calculated the collisional cross sections at small energies for this transition due for collisions with neutral hydrogen atoms.

The collisional ionization rates were computed by the formula of House (1964). After our computations were completed, accurate experimentally determined cross sections for collisional ionization from the ground state of C II were published by Aitken, Harrison, and Rundel (1971). The rates given by the cross sections of Aitken et al. are somewhat higher than those that we used. The photoionization rates from the ground-state levels were calculated by the method of Burgess and Seaton (1960) as modified by Peach (1967). The resulting cross section is smaller by about a factor of 2 than that given by Henry (1970). Since the method of Burgess and Seaton cannot be applied to photoionization from the  $^4\text{P}$  and  $^2\text{D}$  levels, we have simply made estimates.

We assume a  $\nu^{-3}$  cross-section dependence beyond threshold. We shall find that the C II/C III ionization equilibrium is not crucial in the formation of the C II lines, since at the temperatures that turn out to be of interest, almost all the carbon present is in the form of C II. Emission from regions of high temperature, with  $T_e \gtrsim 25,000$  K, does not appear to be significant.

The computer code we use, PANDORA, treats only the ion whose lines are being studied, together with the next stage of ionization. We determine the relative population of C II and C III ions at the same time as we determine the C II level populations. We must simultaneously determine the relative populations of C I and C II at each point in our atmosphere. To do this, we made a series of calculations with a six-level model C I atom, including radiative transfer in both the  $\lambda 1561$  and the  $\lambda 1657$  lines. Our model atom consisted of the  $^3P$  ground state plus the lowest  $^1D$ ,  $^1S$ ,  $^5S^o$ ,  $^3P^o$ , and  $^3D^o$  excited states. Our transition rates were taken from the papers of Lawrence and Savage (1966), Van Regemorter (1962), House (1964), and Burgess and Seaton (1960). We estimated the radiation temperatures in the various ionization continua at each point in the atmosphere, on the basis of the intensity measurements of Detwiler *et al.* (1961) and on calculations of optical depths at the wavelengths of the various continua. We found that the ionization of C I (shown as the curve  $\log N_{C II}/N_{C tot}$  in Figure 40) is very different from the results of density-independent calculations such as those of House (1964). The effects of photoionization by the solar-radiation fields are important, especially for the temperature-minimum region, where the radiative recombination rates can be very small. Thus, we find that the ratio  $N_{C II}/N_{C I}$  is nowhere less than  $10^{-4}$ , and carbon is almost entirely ionized at heights above 1300 km in our model, where  $T_e$  is still less than  $6000^\circ$ . In fact, we find a C I/C II ionization equilibrium quite close to LTE.

#### 6.4 Calculations

Knowing the C I/C II ionization, we have made a series of calculations attempting to match the observational data. We chose a model atmosphere in the photosphere and low chromosphere based on the Harvard-Smithsonian Reference Atmosphere (Gingerich *et al.*, 1971). In the region immediately above 1860 km, our model has a density of  $N_{H tot} = N_e \approx 3 \times 10^{10}$ . Where

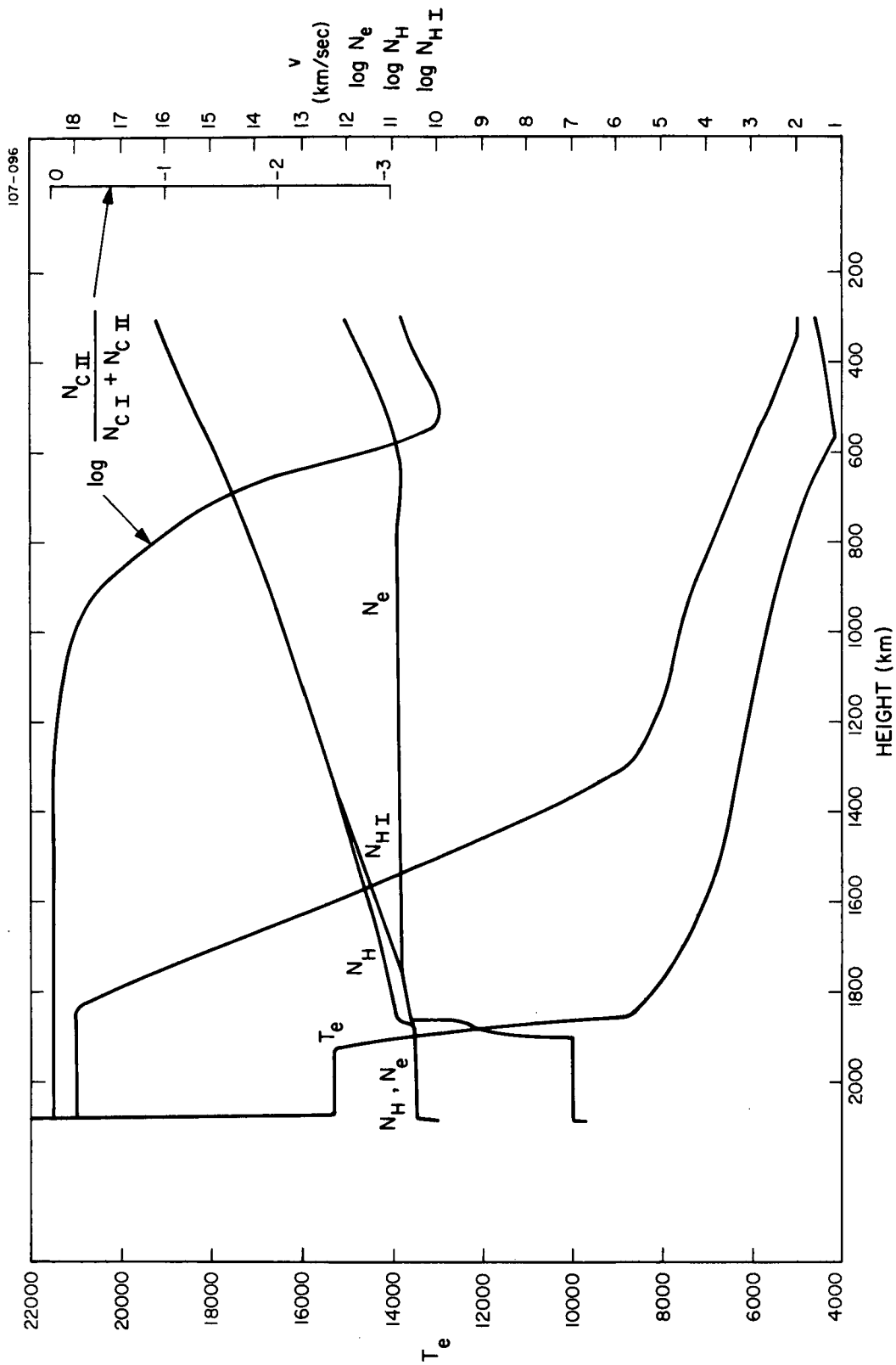


Figure 40. Model 1, atmospheric parameters.

the temperature rises above  $40,000^\circ$ , we have fitted this atmosphere onto a region of steeply rising temperature with constant electron pressure, as proposed by Dupree and Goldberg (1967).

We made some calculations with atmospheric models that rise smoothly from a temperature near  $10,000^\circ$  to temperatures above  $40,000^\circ$ . In such models, if we adjust the thickness of the atmosphere so as to obtain agreement with the observed intensities, we always find that the bulk of the emission arises from an optically thin region with high temperature, near  $40,000^\circ$ . The resulting computed limb brightening is much greater than is observed; values of the limb-brightening parameter are found to be 1.8 to 2.0. As before, we have included the correction due to the finite spatial resolution of the OSO 4 instrument in our theoretical limb-brightening curves. We sum the intensities of both lines in computing the theoretical curves since the OSO 4 observations include both lines.

We are thus led to conclude that the flatness of the observed limb-brightening curve implies the existence of a temperature plateau in the region of formation of the C II lines. In Figure 41, we plot six different models of the chromospheric plateau. We have given in parentheses the computed limb-brightening parameter for each atmosphere. Since we estimate that the observed limb-brightening parameter falls within the range 1.31 to 1.38, all the models except model 5 agree reasonably well with the observations in this respect. All these models have been fitted onto the top of the HSRA atmosphere, so that height zero in Figure 41 corresponds to 1860 km above  $\tau_{5000} = 1$ . In Figure 40, we plot all the important atmospheric quantities for model 1, including the C I/C II ionization ratio and the decrease in micro-turbulence below 1700 km. The other models are identical to model 1 below 1860 km, and all our models have an electron density  $N_e = 3.15 \times 10^{10}$  in the region of the chromospheric plateau. In Figure 42, we show the detailed behavior with height of the line-center optical depth in  $\lambda 1336$  and of the source function for our model 4. In Table 6, we list the characteristics of each of our models and show their agreement with the observations. We shall discuss the models and our conclusions at the same time.

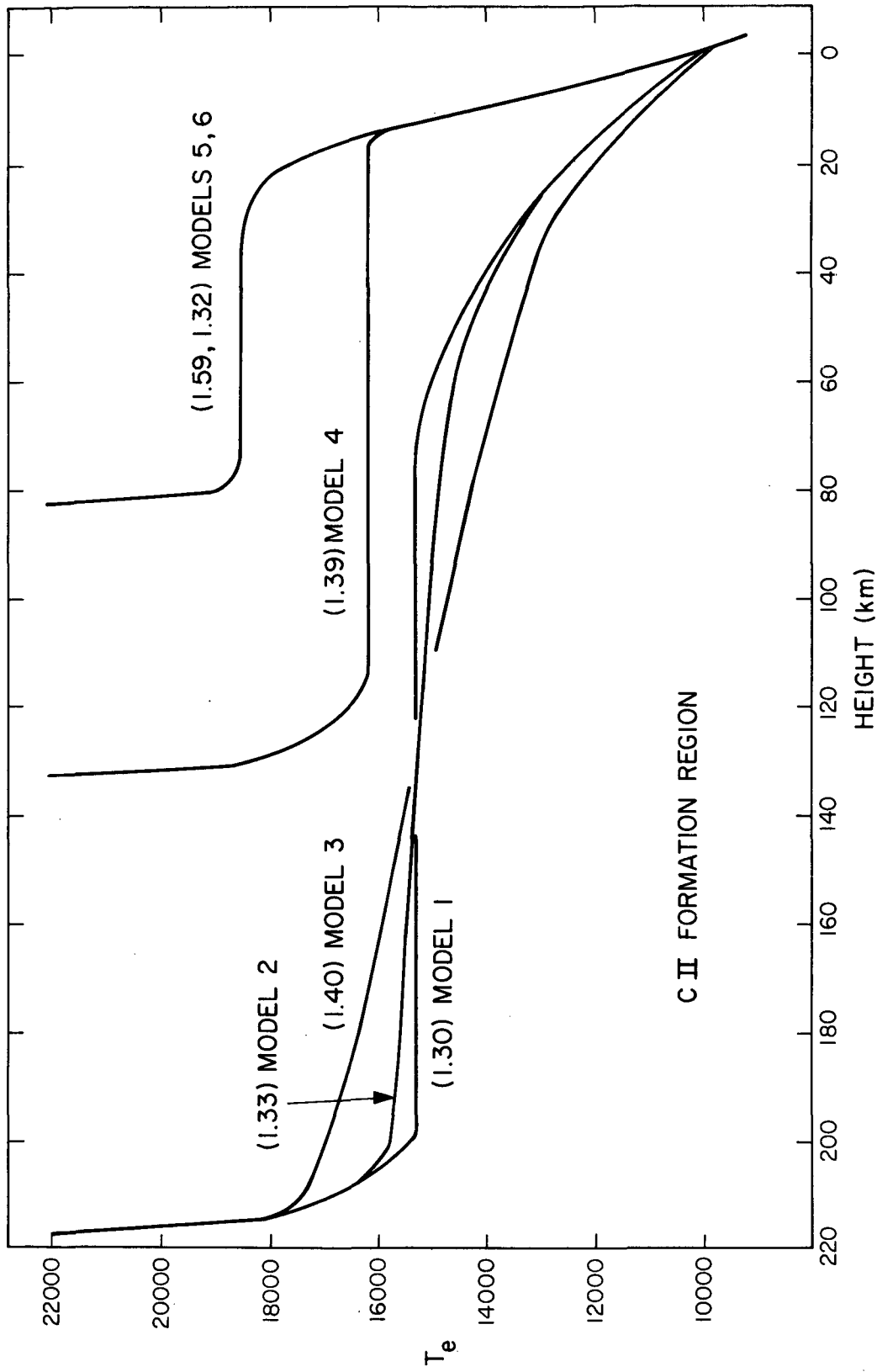


Figure 41. Six model atmospheres, with limb brightenings.

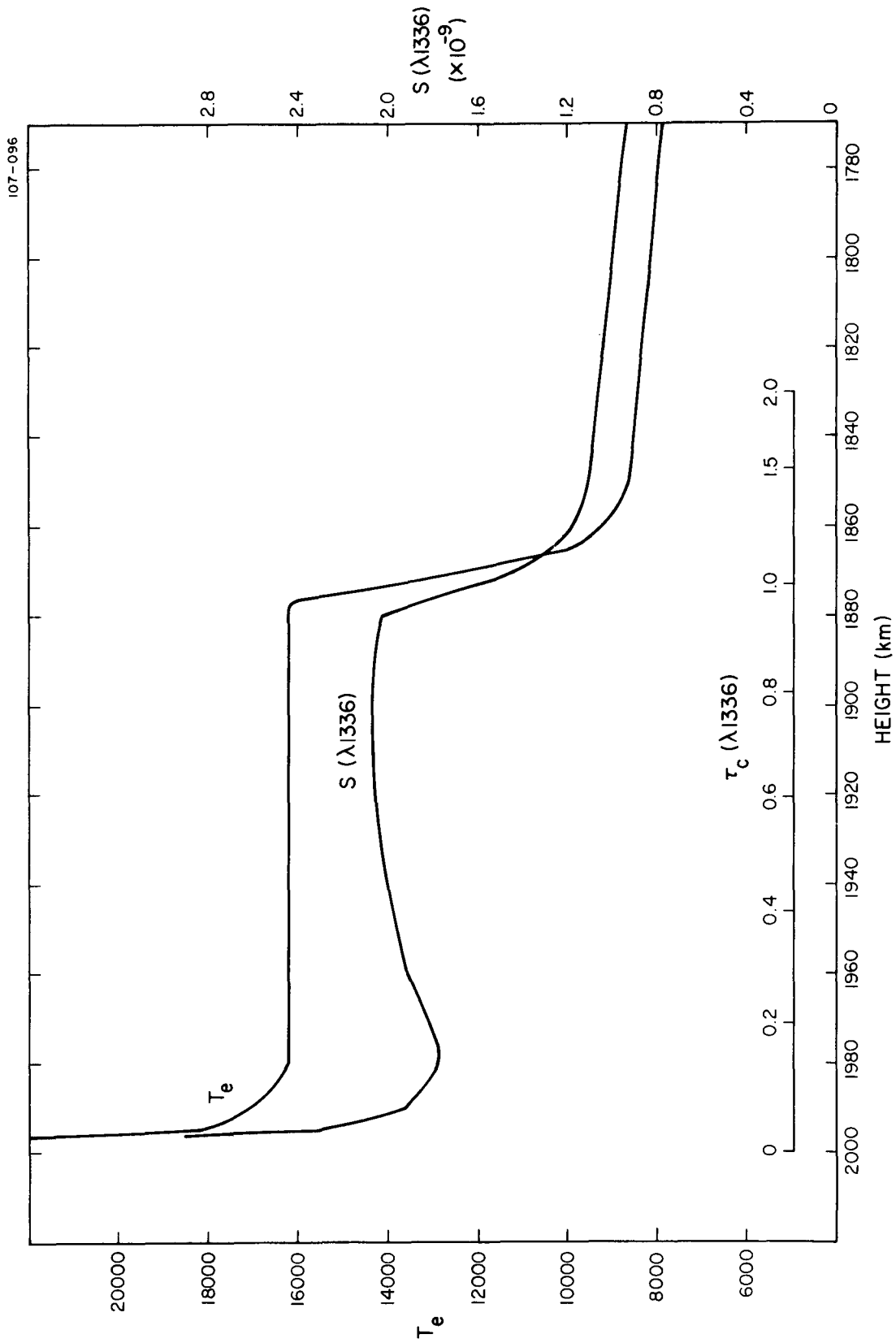


Figure 42. Detail of model 4.

Table 6. Summary of calculations on the C II lines.

	Observed	Model 1	Model 2	Model 3	Model 4	Model 5	Model 6
Combined intensity (both lines)	$1031^{1,2} \pm 50$	1035	1029	1061	1042	1051	1082
Intensity $\lambda$ 1334		440	438	448	437	437	380
Intensity $\lambda$ 1336		595	591	613	605	614	702
Ratio $\lambda$ 1334/ $\lambda$ 1336	$1.0^3, 1.02^4, 0.73^5$	0.74	0.74	0.73	0.72	0.71	0.54
Limb brightening	$1.35 \pm 0.03$	1.30	1.32	1.40	1.39	1.59	1.32
FWHM <sup>6</sup> $\lambda$ 1334	$0.22 \text{ \AA}^4$	0.22	0.22	0.22	0.22	0.22	0.06
FWHM <sup>6</sup> $\lambda$ 1336	$0.25 \text{ \AA}^4$	0.22	0.22	0.22	0.22	0.21	0.06
Average $T_e$ of plateau (K)		15,300	15,300	15,300	16,200	18,500	18,500
Width of plateau (km)		160	160	160	110	60	60
Microturbulent velocity (cm sec <sup>-1</sup> )		18.0	18.0	18.0	18.0	18.5	0.0

<sup>1</sup> Units are ergs cm<sup>-2</sup> sec<sup>-1</sup> ster<sup>-1</sup> at center of solar disk, integrated over the line or lines.

<sup>2</sup> From Dupree and Reeves (1971).

<sup>3</sup> From Detwiler *et al.* (1961).

<sup>4</sup> From Berger *et al.* (1970).

<sup>5</sup> From J. Vernazza (1971, private communication).

<sup>6</sup> Full width at half-maximum.

Models 1, 2, and 3 show the effects of even a small slope in the temperature-height relation on the computed limb-brightening parameter. These models all have average temperatures in the plateau of  $15,400^\circ$  and plateau widths of approximately 150 km. Note that for the relatively small temperature gradient of model 3, we still find a limb-brightening parameter slightly greater than is observed. For these models and for models 4 and 5, we have assumed that the widths of the observed line profiles are due to a combination of thermal broadening, which contributes  $5 \text{ km sec}^{-1}$ , and microturbulence, for which we must assume the values in Table 6.

Within certain limits, we can satisfy the observations with a whole family of model atmospheres with different chromospheric plateau temperatures and different plateau widths. In the low temperature direction, the variation is limited by the fact that the Lyman continuum originates at a region with  $T_e \approx 8300^\circ$ , and therefore the plateau must be optically thin in the Lyman continuum. In fact, recent work by Vernazza *et al.* (1971) implies that the required optical thinness does not occur for plateau temperatures less than  $18,000^\circ$  or thereabouts. So our models 1, 2, and 3 are apparently too cool.

If we assume, as we have above, that the line broadening is due to microturbulence, we cannot match both the observed intensity and the limb brightening with any plateau temperature higher than  $16,000^\circ$ , as shown by our model 4. In Figure 42, we show the behavior of the source function and optical depth in  $\lambda 1336$  for this model. Note that there is a local maximum in the source function in the center of the chromospheric plateau and that the optical depth of the plateau in the center of this line is of order unity. We find that an optical depth close to unity is necessary in order to reproduce the observed limb brightening.

Model 5 is an example of a plateau temperature of  $18,500^\circ$  and width of 60 km. We find that with a microturbulent velocity large enough to produce the observed line widths, the limb brightening is 1.59, which is too high. Alternatively, one might consider the possibility that the broadening of the line is produced primarily by macroturbulence. Microturbulence is usually defined as turbulence on a scale much less than the characteristic height range over

which a line is formed, while macroturbulence has a scale much greater than this size. In the case of C II, the lines are formed over a range of about 500 km, so any scale greater than this and less than the projected length of the spectrograph slit, which was several times  $10^4$  km, would be seen as macroturbulence. A spectrograph with high spatial resolution should show the line profiles of individual macroturbulent elements, which might have narrow widths but centers displaced with respect to one another. Averaging over many macroturbulent elements would produce a line profile with a width greater than that of the profiles of the individual elements. For model 6, we set the microturbulent velocity  $v$  equal to zero at all heights, and the resulting increase in line-center optical depths produces good agreement with the limb-brightening observations. Since the thermal velocity is  $5 \text{ km sec}^{-1}$ , we could have chosen values of  $v$  up to about  $5 \text{ km sec}^{-1}$  if we had wished, without much difference in the results. High-resolution stigmatic spectra of small portions of the sun should soon be able to show whether macroturbulence or microturbulence is a better approximation.

In Table 6, note that models 1 to 5 show reasonable agreement between observed and computed ratios of intensities  $\lambda 1334/\lambda 1336$  if we accept Vernazza's observation. Model 6 yields a value rather too low, while none of our models yields values close to unity, as observed by Detwiler et al. (1961) and by Berger et al. (1970). The computed values of this ratio are sensitive to the fine-structure collisional rates between the sublevels of the  $^2P$  and the  $^2D$  states. Possibly, our fine-structure transition rates are too low, but even with very strong coupling, we never compute values for the ratio  $\lambda 1334/\lambda 1336$  greater than 0.84. The observations of this ratio should be improved in the near future.\*

Note that given one model of the chromospheric plateau, we can quite easily find other models, with different temperatures and densities, that satisfy the same intensity and limb-brightening observations. To a good approximation, since the C II lines are "effectively optically thin," the intensity is simply proportional to the number of line photons created:

---

\*J. Vernazza has recently revised his method of data reduction and now measures a ratio  $\lambda 1334/\lambda 1336$  of  $0.85^{+0.05}_{-0.01}$  (1971, private communication).

$$I \propto N_e^2 \Delta Z \exp\left(-\frac{h\nu}{kT}\right) , \quad (144)$$

where  $\Delta Z$  is the thickness of the chromospheric plateau, while the optical depth is given by

$$\tau \propto N_e \Delta Z v_{\text{Dop}}^{-1} . \quad (145)$$

If we hold these two quantities constant, we can produce new atmospheres with different values of  $N_e$ . (We have omitted the dependences on the  $A$  values and excitation cross sections, which are proportional to  $\tau$  and  $I$ , respectively.) For instance, for model 6 our total pressure in the plateau region is  $0.16 \text{ dyne cm}^{-2}$ . Values as low as  $0.10 \text{ dyne cm}^{-2}$  are commonly quoted for the pressure in the chromosphere-corona transition region, so we might wish to compute a new atmosphere for this pressure. Equations (144) and (145) yield

$$\begin{aligned} N_e &= 1.77 \times 10^{10} , \\ \Delta Z &= 107 \text{ km} , \\ T_e &= 20,500^\circ . \end{aligned}$$

This model resembles some of those used by Vernazza et al. (1971) in their analysis of the Lyman lines and continuum. Note that this is the model of the very highest temperature we can allow, even assuming that microturbulence is negligible.

In conclusion, we should reiterate our main point that only models with definite chromospheric temperature plateaus can satisfy the observations. Various plateaus with temperatures in the range  $15,000$  to  $20,500^\circ$  and widths from  $60$  to  $160 \text{ km}$  can yield good agreement with observations; the question of whether the line broadening is due to microturbulence or macroturbulence is very important.

## 7. THE CARBON III LINES

7.1 Introduction

Carbon III is an ion of the beryllium-like sequence and as such has a singlet and a triplet system of energy levels. Figure 43, of the energy-level diagram for C III, indicates the  $\lambda 977$  singlet line and the  $\lambda 1176$  triplet line. The  $\lambda 977$  line is one of the strongest in the solar ultraviolet spectrum. This line was tabulated by Hinteregger (1965) as having an intensity of  $0.08 \text{ erg cm}^{-2} \text{ sec}^{-1}$  at the earth's distance from the sun, and by Dupree and Reeves (1971) as having a disk-center intensity of  $900 \text{ ergs cm}^{-2} \text{ sec}^{-1} \text{ ster}^{-1}$  at the solar surface, which corresponds to about 0.76 of Hinteregger's earlier value. The absolute accuracy of Dupree and Reeves' value is estimated to be within about a factor of 2. This line has been studied by Withbroe (1970a), who derived a line-center optical depth of 0.56 from the observed line intensity alone. Withbroe also measured the limb brightening of this line from OSO 4 data and found that the degree of limb brightening is considerably smaller than a  $1/\mu$  law would yield. He found good agreement between the observed limb brightening of  $\lambda 977$  and the limb brightening that he calculated using the model defined by Dupree and Goldberg (1967, Figure 3). In the region  $T_e < 10^5 \text{ K}$ , where C III is most abundant, the model of Dupree and Goldberg is poorly defined by the observational points, and Withbroe chose a "best" curve, which he does not specify. His model yielded an optical depth close to 0.56. We should like to determine and define more clearly the range of model atmospheres that will fit the data on the  $\lambda 977$  line.

The subordinate triplet line,  $\lambda 1176$ , is optically thin and shows limb brightening close to a  $1/\mu$  law. Withbroe did not study this line, since it is not a resonance line. Dupree and Reeves tabulate the disk-center intensity of this line as  $248 \text{ ergs cm}^{-2} \text{ sec}^{-1} \text{ ster}^{-1}$ . It turns out that the relative intensities of the  $\lambda 1176$  and  $\lambda 977$  lines depend on electron density in the region of  $\log N_e = 10$  to 11, because under these conditions radiative deexcitation of one

of the triplet levels via the  $^3P_1^0 - ^1S_0$ ,  $\lambda 1909$  transition, which has an A value of  $190 \text{ sec}^{-1}$  according to Garstang and Shamey (1967) and Osterbrock (1970), competes with collisional deexcitation of the three  $^3P$  levels. So in principle, one might expect that, given the three observed quantities of the limb brightening in  $\lambda 977$  and the intensities of  $\lambda 977$  and  $\lambda 1176$ , it would be possible to determine the average temperature, the electron density, and the physical thickness of the region of the atmosphere where the C III lines are formed. We will investigate to what extent this can or cannot be done.

107-096

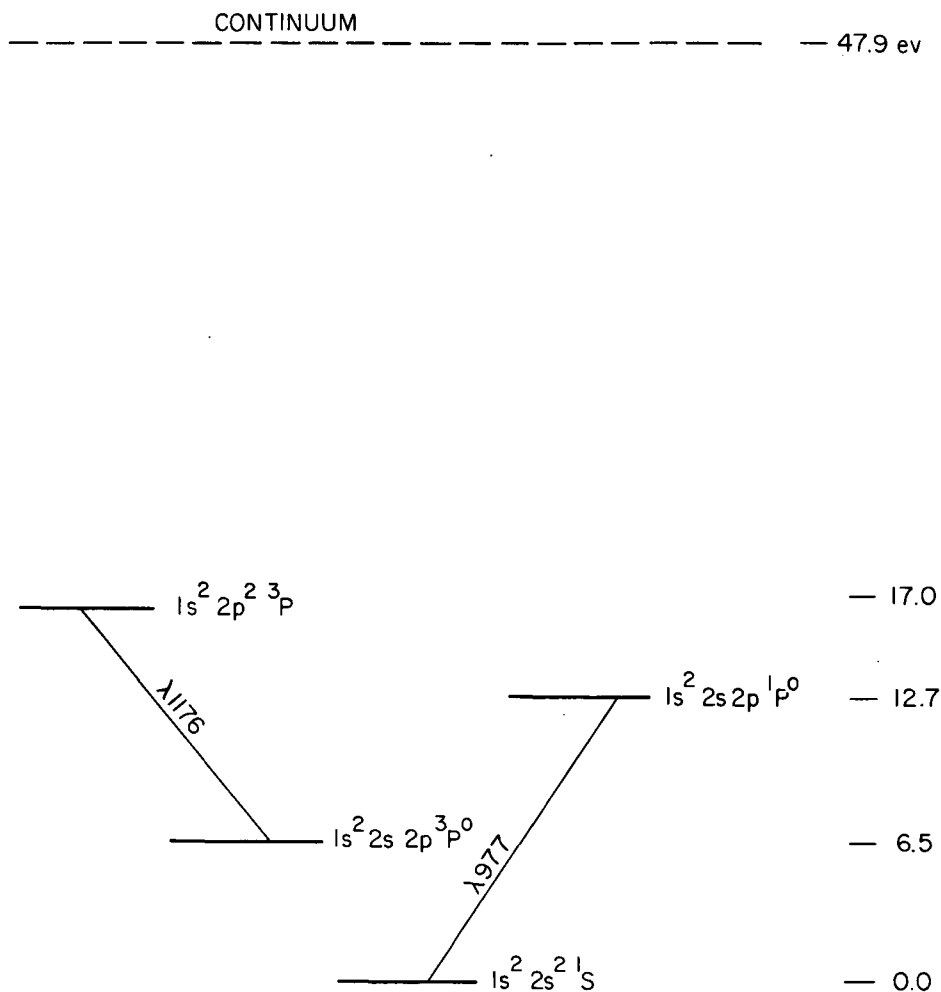


Figure 43. Energy levels for C III.

## 7.2 The Resonance Line

First, we shall discuss the problem of the ionization equilibrium of carbon. As we pointed out in connection with the C II lines, the work of Burgess and Sommers (1969) implies that for densities close to  $10^{10} \text{ cm}^{-3}$ , neither the curves of House (1964) nor those derived from the assumptions of Allen and Dupree (1969) are valid. Jordan (1969) has calculated ionization equilibria for carbon, using a temperature-density variation appropriate for the solar atmosphere. She has taken into account in an approximate way the effects of ionization from high bound levels, which reduce the dielectronic recombination effects. In Figure 44, we show the ionization equilibria for carbon as tabulated by various authors. In our calculations, we have used the C II-C III ionization equilibrium of Jordan as input for our C III line computations.

The C III/C IV ratio is determined internally by the computer code that computes C III line formation. We found that in order to obtain the desired ionization equilibrium, it was necessary to increase artificially the radiative recombination coefficients by a factor of 25 over those derived from a direct use of the quantum-defect method (Burgess and Seaton, 1960). Note that the maximum abundance of C III occurs at 59,000 K, rather than at the 90,000 K found by Allen and Dupree or the 47,000 K found by House.

Let us examine with a very simple model the formation of a line such as C III  $\lambda$  977. For purposes of determining the intensity in this line, it is probably not necessary to solve any line-transfer problem, since every photon that is created will escape. In other words,  $\epsilon \tau \ll 1$ , and the line is "effectively optically thin." Solution of the line-transfer problem might be important, however, in studying the degree of limb brightening in this line.

If we conceive of the  $\lambda$  977 line as being formed in a thin layer of thickness  $\Delta Z$  and of constant temperature with negligible microturbulence, we can determine its optical depth. We denote by  $F$  the flux in  $\lambda$  977 measured at the earth's orbit, and by  $C_{12}$  the  $^1S \rightarrow ^1P$  collisional rate per C III atom in the

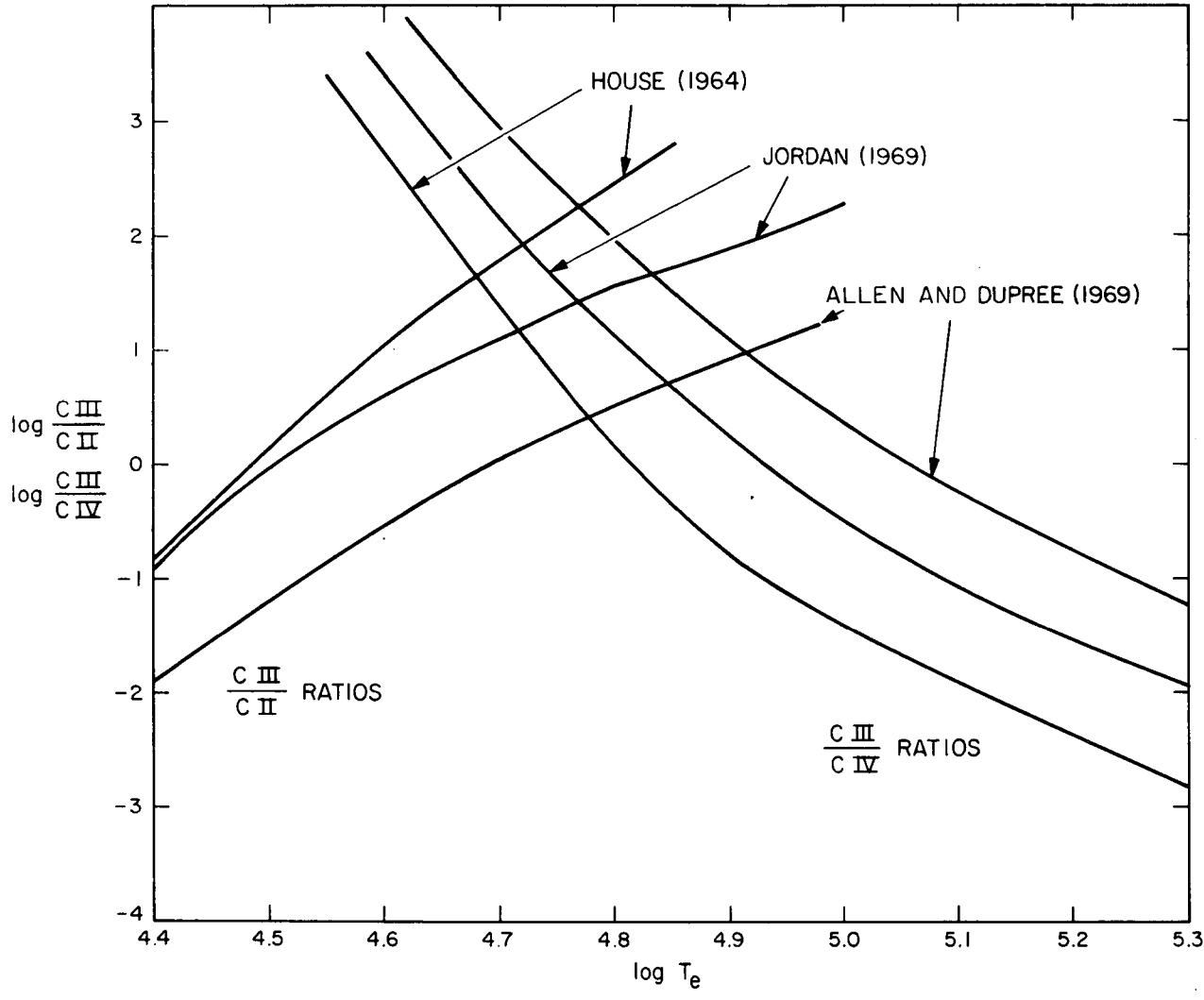


Figure 44. Ionization equilibria for C III.

ground state per electron per  $\text{cm}^3$ . Then, since only half the photons generated will escape from the sun, while half will be emitted downward, if we ignore excitations via the metastable  $^3\text{P}$  state, we have

$$4\pi R_{\text{au}} F = \frac{1}{2} 4\pi R_{\odot}^2 \Delta Z N_1 C_{12} N_e h\nu \quad ; \quad (146)$$

and denoting the line-center optical depth by  $\tau_0$ ,

$$\tau_0 = \alpha_0 N_1 \Delta Z \quad (147)$$

where  $\alpha_0$  is the line-center absorption cross section, we obtain

$$\tau_0 = \frac{R_{\text{au}}^2}{R_{\odot}^2} \frac{2 \alpha_0 F}{h\nu C_{12} N_e} \quad . \quad (148)$$

Inserting the expression for  $C_{12}$  of Seaton (1964), which is

$$C_{ij} = 1.70 \times 10^{-3} \frac{f(i \rightarrow j)}{\chi_{ij}} \frac{10^{-5040 \chi_{ij}/T}}{T^{1/2}} \bar{g} \quad (149)$$

with  $\chi_{ij}$  given in electron volts, and inserting  $T_e = 68,000 \text{ K}$  and the value  $N_e = 8.83 \times 10^9$  derived from Dupree and Goldberg's (1967) choice of a transition-region value of  $N_e T_e = 6 \times 10^{14}$ , we have, upon reduction,

$$\tau_0 = \frac{0.1055}{\bar{g}} \quad . \quad (150)$$

Note that Van Regemorter's (1962) formula yields  $\bar{g} = 0.20$ , while Pottasch (1964) tabulates a Gaunt factor of 0.41. Thus,  $\tau_0$  should fall between about 0.26 and 0.53.

Since, to a first approximation, the metastable  $^3\text{P}$  state is populated and depopulated by collisions, we can immediately calculate the relative populations

of the  $^3P$  state and ground state and thus derive a physical thickness for the layer of formation of the C III lines. Using the  $f$  value of 0.81 from Wiese et al. (1966), we find that at  $T_e = 68,000$  K, half the C III atoms will be in the excited  $^3P$  level and the layers corresponding to our two estimates of  $\tau_0$  above will be 34 and 69 km thick. Note that this is somewhat thicker than implied by the atmosphere of Kanno and Tominaga, which is quoted by Pottasch (1964). These authors find only 7.8 km between the temperature limits of 50,000 and 100,000 K, although it is possible that these temperature limits do not completely delimit the region of C III line formation.

As a first step, it was decided to study the  $\lambda 977$  line alone. To do this, one must take into account direct excitation to the  $^1P^0$  level from the ground level and also indirect excitation via the  $^3P^0$  state. In Table 7 we tabulate the set of atomic parameters adopted for a study of the  $\lambda 977$  line. We have separated the three  $^3P^0$  levels, which are in fact separated by 23 and 57  $\text{cm}^{-1}$ .

We have used Moore's (1949) values for the energy levels. Our adopted photoionization cross sections are tabulated for the heads of the various continua, and we have assumed a  $\nu^{-3}$  dependence of the photoionization cross sections beyond threshold. Actual photoionization is negligible in comparison with collisional ionization, but the photoionization cross sections determine the photorecombination rates. As explained above, we have scaled up the cross sections predicted by the method of Burgess and Seaton (1960) so as to reproduce Jordan's (1969) ionization equilibria. The collisional ionization rates are tabulated in terms of the quantities  $C$  I defined in equation (131). We have used the formula of House (1964) (equation 130) to determine the collisional ionization rates. For our initial work, we chose to calculate excitation in the  $\lambda 977$  line according to the formula of Seaton (1964) (equation 149) with an averaged Gaunt factor  $\bar{g} = 0.20$ . The collisional rates between the ground state and the excited  $^3P^0$  levels were calculated by using the collision-strength calculations of Osterbrock (1970). For the transitions between the  $^3P^0$  levels and the  $^1P^0$  upper level of the  $\lambda 977$  line, there are no published calculations of collision strengths, so we used the same collision strength as given by Osterbrock's calculations for the  $^1S-^3P^0$  collisions.

Table 7. Atomic parameters for C III.

Level number	Level	Excitation ( $\text{cm}^{-1}$ )	Statistical weight	Photoionization	Collisional ionization (CI)
1	$1S$	0	1	$5.0 \times 10^{-17}$	$2.60 \times 10^{-11}$
2	$3P_0^0$	52315	1	$1.0 \times 10^{-16}$	$1.74 \times 10^{-11}$
3	$3P_1^0$	52338	3	$1.0 \times 10^{-16}$	$1.74 \times 10^{-11}$
4	$3P_2^0$	52394	5	$1.0 \times 10^{-16}$	$1.74 \times 10^{-11}$
5	$1P_0^0$	102351	3	$2.0 \times 10^{-16}$	$2.41 \times 10^{-11}$
6	$3P_0$	137374	1		
7	$3P_1$	137403	3		
8	$3P_2$	137450	5		
	Continuum	386160	2		

$A(3P_1^0 - 1S) = 190 \text{ sec}^{-1}$  (Garstang and Shamey, 1967).

$A(1P_0^0 - 1S) = 1.9 \times 10^9 \text{ sec}^{-1}$  (Wiese et al., 1966).

$f(1P_0^0 - 1S) = 0.81$  (Wiese et al., 1966).

The collisional rates within the  ${}^3P^0$  term that we used were estimated from various considerations. We included the effects of both electron and proton collisions, using ratios of electron to proton density derived from a H-to-He number-density ratio of 10 to 1, and estimated H and He ionization equilibria. With such an assumed ratio  $N_p/N_e$ , we can still use equation (127) to express the collision rates in terms of CE's. The proton-collision cross sections were calculated by Munro et al. (1971), who somewhat improved the assumed energy dependence of the cross sections of Bahcall and Wolf (1968). The electron-collision cross sections for these transitions were also calculated by Munro et al., using the original results of Blaha (1968), corrected for exchange in the way used by Blaha (1969) and by Saraph, Seaton, and Shemming (1969). Our derived curves for  $CE_{ij}(T_e)$  are plotted in Figure 45.

A series of calculations was made using the set of atomic parameters that we have described and several different atmosphere models. We assumed that the C III lines were formed in a layer of constant electron pressure such that  $N_e T_e = 6 \times 10^{14}$ , and we varied the physical thickness, the temperature, and the microturbulent velocity in the region of formation of the line. The agreement between these results and the observations was reasonable but not perfect, and we wish merely to note some points that are not highly dependent upon the chosen atmosphere model.

The observed limb-brightening curve of Withbroe (1970a) agrees with our calculated limb-brightening curve only if we adjust the thickness of the formation layer so as to have a line-center optical depth of  $\tau_c = 0.55$ , which when scaled according to Withbroe's convention yields  $\tau = 0.975$ , in good agreement with Withbroe's value of  $\tau = 1.00$  and also with our independently derived value of  $\tau_c = 0.53$  from equation (150) with  $\bar{g} = 0.20$ . In Figure 46, we plot the limb-brightening observations from Withbroe (1970a) and our curve for  $\tau_c = 0.54$ . The agreement of our curve with that derived theoretically by Withbroe, and the agreement of our optical depth with his, imply that a detailed solution of the radiative-transfer and statistical-equilibrium equations is not necessary for a line so optically thin as this one.

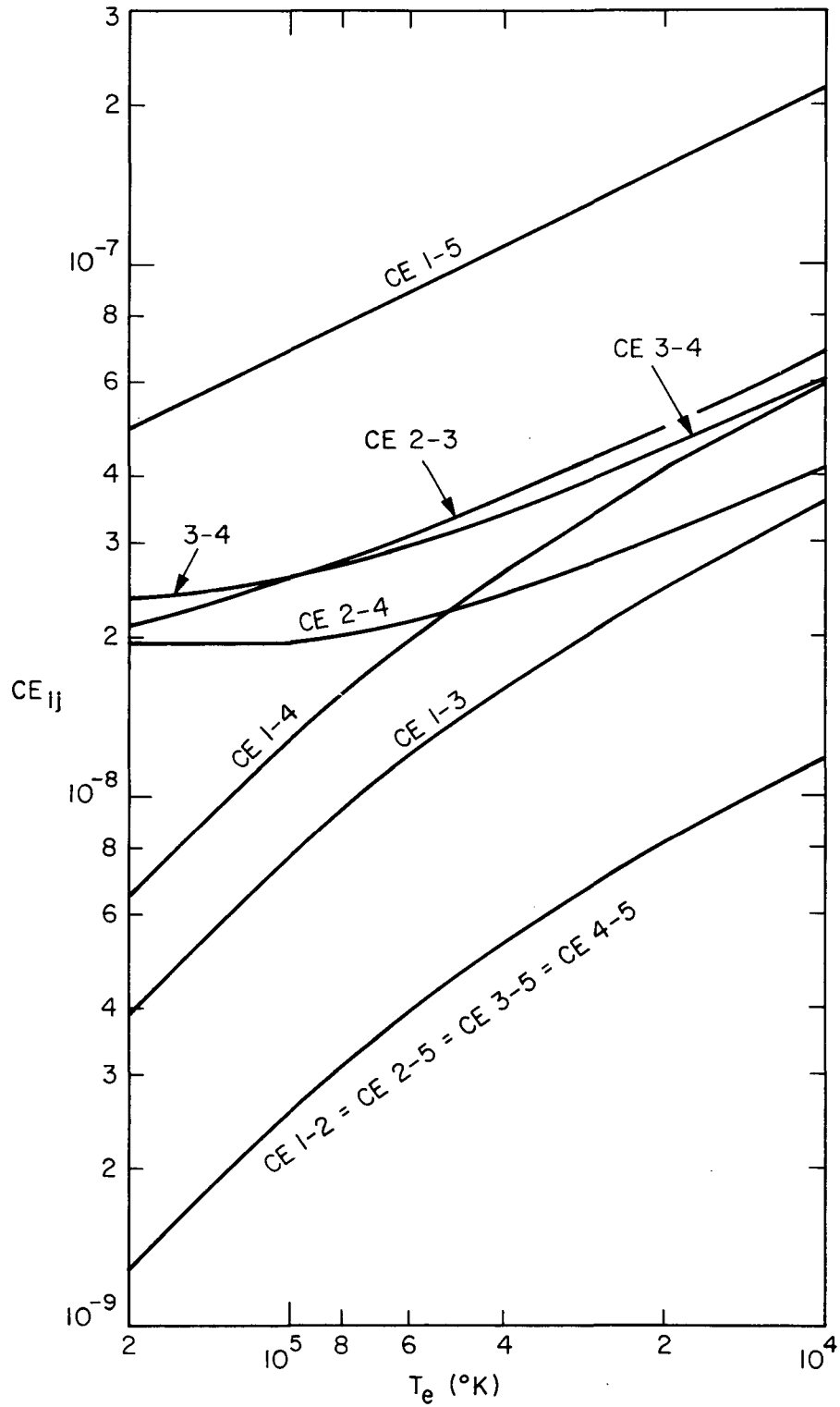


Figure 45. Collisional rate constants for C III.

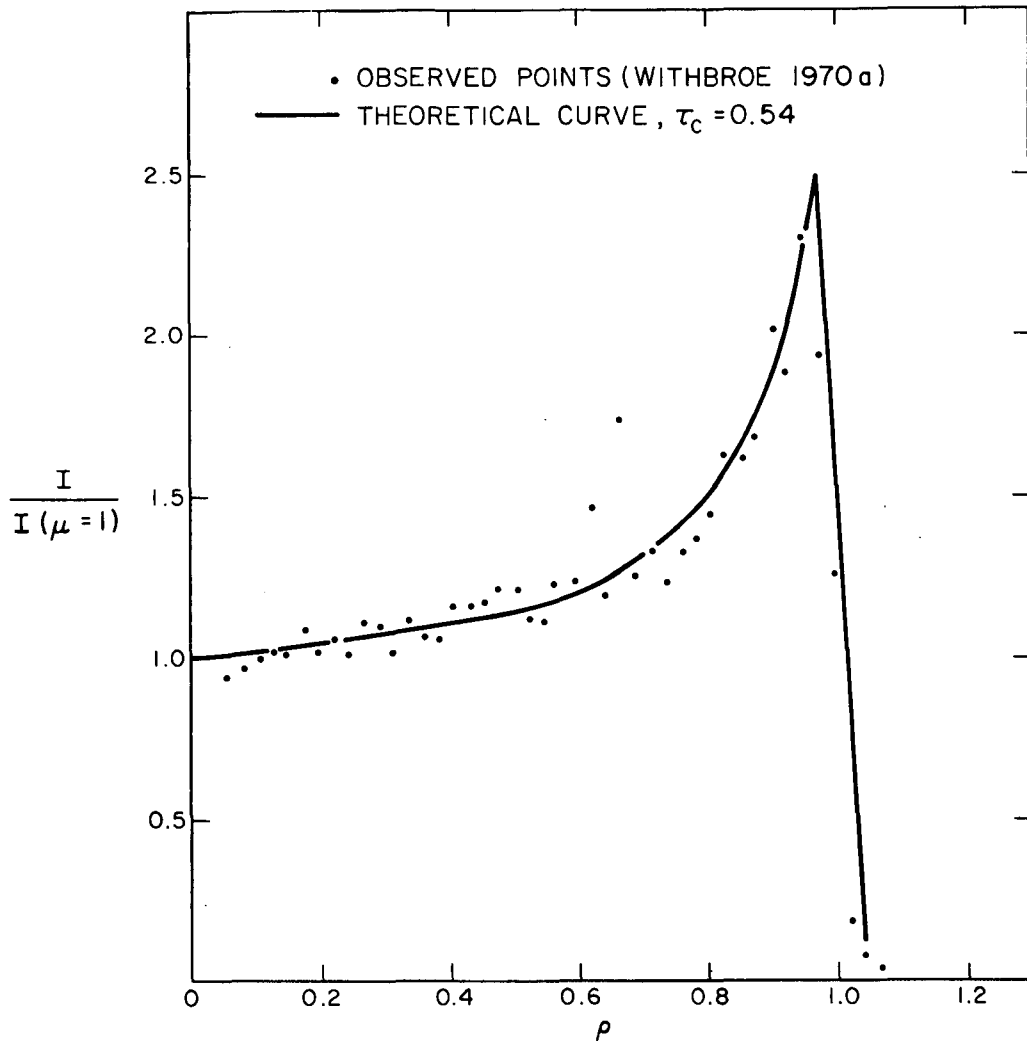


Figure 46. Comparison of C III limb-brightening observations of Withbroe (1970a) with a theoretical curve of constant  $S$  and  $\tau_c = 0.54$ .

For models that give the correct optical thickness in  $\lambda 977$ , we find a tendency to derive an intensity in  $\lambda 977$  greater than that observed. Since for a constant line-center optical depth the intensity in the line is proportional to the broadening velocity, we are led to propose a broadening velocity that is as small as possible. In the region of formation of C III, the thermal broadening velocity is about  $10 \text{ km sec}^{-1}$ , so the microturbulent broadening velocity is apparently considerably smaller than  $10 \text{ km sec}^{-1}$  — that is,  $\lesssim 5 \text{ km sec}^{-1}$ . High-resolution spectra will probably settle this point soon.

We note it would seem unlikely that the regions of formation of C II and of C III, which are directly adjacent to one another in the solar atmosphere, should have microturbulent velocities as different as 16 and 5 km sec<sup>-1</sup>, respectively.

Our models also indicate that approximately 50% of the total number of C III atoms will be found in the <sup>3</sup>P<sup>o</sup> levels, so it is incorrect to assume that nearly all the C III is in the ground state. Nevertheless, computations such as those reported above (equations 146 to 150) are valid since the proportion of λ 977 photons created by excitation via the <sup>3</sup>P<sup>o</sup> states is relatively small (~ 10%).

### 7.3 Inclusion of the Subordinate Line

It was decided that, since it appears that radiative transfer and optical-depth effects in λ 977 are small, it would be best for us to do a series of calculations of the populations of the various C III levels, neglecting radiation in the lines and assuming one value for N<sub>e</sub> and for T<sub>e</sub>. We could then study the problem of matching the λ 977 and λ 1176 intensities and the optical depth in λ 977. We therefore wrote a computer program that solves the equations of statistical equilibrium for levels one to five in Table 7, allowing us to vary N<sub>e</sub> and T<sub>e</sub> and, if necessary, the various collisional transition rates as well. To compute the relative intensities of the λ 977 and λ 1176 lines, we must specify the collisional excitation rates of the six lines of the λ 1176 multiplet. We used equation (149), with  $\bar{g}$  a variable parameter. We assumed in all our calculations that  $\bar{g}$  is equal for all transitions within this multiplet. The data tabulated for this multiplet by Wiese et al. (1966) are given in Table 8.

Once we have computed the relative populations of levels 1 to 5, the ratio of emissivities per cm<sup>3</sup> in the λ 977 and λ 1176 lines is given by

$$\frac{\epsilon_{977}}{\epsilon_{1176}} = \frac{h\nu_{977}(N_1 C_{1-5} + N_2 C_{2-5} + N_3 C_{3-5} + N_4 C_{4-5})}{h\nu_{1176}[N_2 C_{2-7} + N_3(C_{3-6} + C_{3-7} + C_{3-8}) + N_4(C_{4-7} + C_{4-8})]} \quad (151)$$

Table 8. Data for the C III  $\lambda$  1176 multiplet.

Level numbers	$\lambda$	Transition	$\omega_{\text{lower}}$	$\omega_{\text{upper}}$	A	f
2-7	1175.25	$^3P_0^0 - ^3P_1$	1	3	$4.2 \times 10^8$	0.26
3-6	1175.97	$^3P_1^0 - ^3P_0$	3	1	$1.3 \times 10^8$	0.087
3-7	1175.57	$^3P_1^0 - ^3P_1$	3	3	$3.1 \times 10^8$	0.065
3-8	1174.92	$^3P_1^0 - ^3P_2$	3	5	$3.1 \times 10^8$	0.11
4-7	1176.35	$^3P_2^0 - ^3P_1$	5	3	$5.2 \times 10^8$	0.065
4-8	1175.70	$^3P_2^0 - ^3P_2$	5	5	$9.4 \times 10^8$	0.20
Multiplet average:	1175.70	$^3P^0 - ^3P$	9	9	$1.3 \times 10^9$	0.26

However, this emissivity is proportional to the total flux in the line, whereas the observations of Dupree and Reeves refer to specific intensity at the center of the solar disk. For a line that shows  $1/\mu$  limb-brightening behavior, it can easily be shown that  $F = 2\pi I(\mu = 1)$ . For a line whose limb brightening is less pronounced, the ratio of  $F$  to  $I(\mu = 1)$  depends only on the limb-brightening curve falling to  $\pi$  for a flat limb-brightening curve. We determined numerically that the ratio  $F/I(\mu = 1)$  corresponding to the observed C III  $\lambda 977$  limb-brightening curve is 4.67. Therefore, our deduced ratio of intensities is

$$\frac{I_{977}}{I_{1176}} = \frac{\epsilon_{977}/4.67}{\epsilon_{1176}/6.283} \quad (152)$$

By considering the absolute intensities of the lines, we can determine the total number of C III ions per  $\text{cm}^2$  in the layer of C III line formation and thus the optical depth in the center of  $\lambda 977$ .

In other words, in general the three observed quantities  $I_{977}$ ,  $I_{1176}$ , and  $\tau_c(\lambda 977)$  serve to define uniquely  $N_e$ ,  $T_e$ , and the thickness of the layer of formation under our assumptions. It was found desirable to make this calculation for a variety of assumed values of  $\bar{g}(\lambda 977)$ , which we shall denote by  $G_1$ , and of  $\bar{g}(\lambda 1176)$ , which we shall denote by  $G_2$ . In Figure 47, we plot the derived values of  $\log N_e$  and  $\log T_e$  for various assumed values of  $G_1$  and  $G_2$ . It turns out that it is only possible to satisfy the three observational constraints on this problem with a limited number of  $(G_1, G_2)$  pairs of values. In Figure 48, we plot a large number of trial pairs of  $(G_1, G_2)$  values, indicating which pairs have consistent solutions for  $I_{977}$ ,  $I_{1176}$ , and  $\tau_{977}$ . Only a narrow band of  $(G_1, G_2)$  pairs allows solutions. For  $G_1 < 0.40$ , this band centers on  $G_1 = G_2$ , while for  $G_1 > 0.40$ , we find  $G_2$  is slightly greater than  $G_1$ . The form of the solution or lack thereof is indicated by the curves on Figure 49. For  $(G_1 = 0.20, G_2 = 0.20)$  and  $(G_1 = 0.41, G_2 = 0.33)$ , we have plotted curves for points that yield layers of line formation satisfying two of the three constraints. The curves labeled ratio  $(G_1, G_2)$  yield correct  $\lambda 977$  intensities and correct  $\lambda 977/\lambda 1176$  intensity ratios, while the curves labeled  $\tau(G_1, G_2)$  yield correct  $\lambda 977$  intensities and correct  $\tau$  values for  $\lambda 977$ .

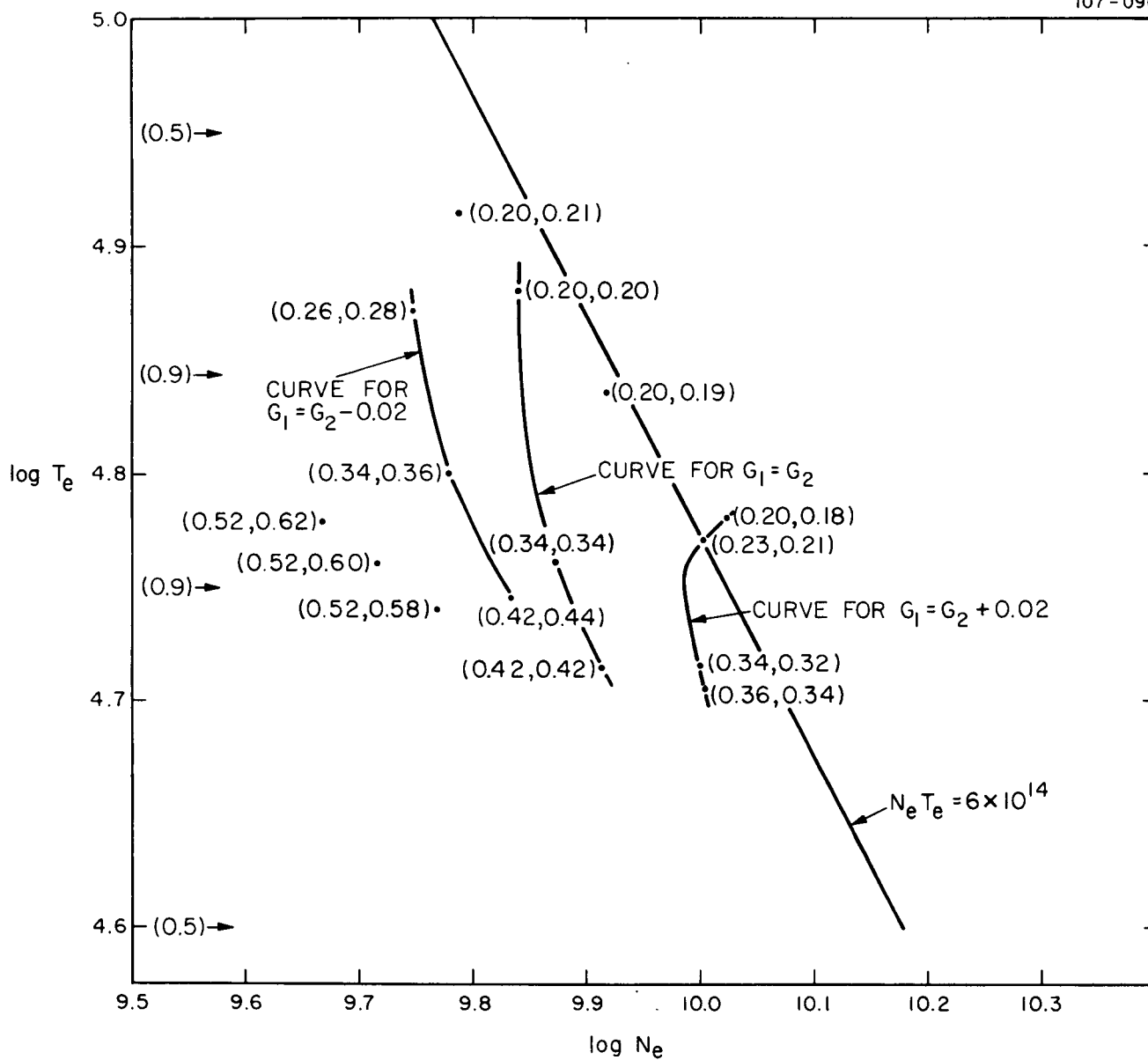


Figure 47.  $\log N_e$  and  $\log T_e$  found from consistent solutions for  $I_{977}$ ,  $I_{1176}$ , and  $\tau_c(\lambda 977)$  for various values of the averaged collisional Gaunt factors  $\bar{g}(\lambda 977)$  and  $\bar{g}(\lambda 1176)$ , denoted by  $(G_1, G_2)$ .

For  $(G_1 = 0.20, G_2 = 0.20)$ , these two curves cross at the point  $\log T_e = 4.88$ ,  $\log N_e = 9.84$ , which satisfies all the observations. For  $(G_1 = 0.41, G_2 = 0.33)$ , the two curves do not cross at any point, which means that no consistent solution is possible.

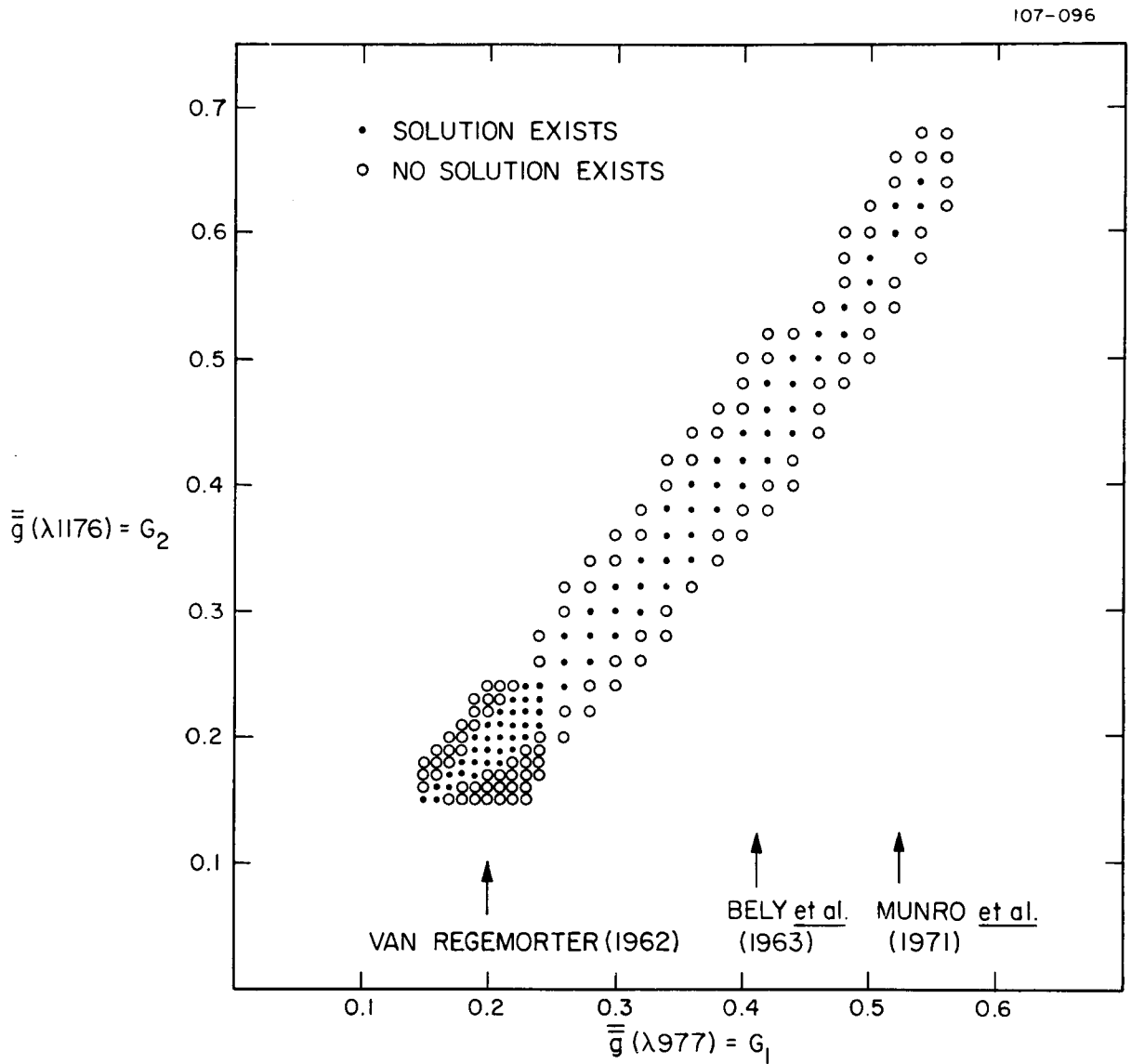


Figure 48. Region of possible consistent solutions for  $I_{977}$ ,  $I_{1176}$ , and  $\tau_c(\lambda 977)$  as functions of the averaged collisional Gaunt factors  $\bar{g}(\lambda 977)$  and  $\bar{g}(\lambda 1176)$ .

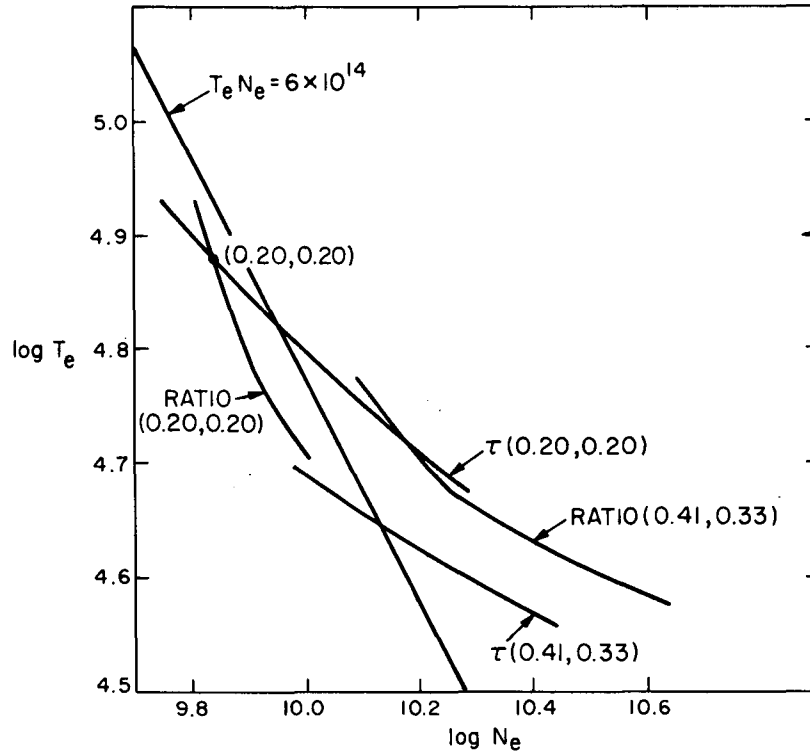


Figure 49. Curves of the loci of points in the  $\log N_e$ ,  $\log T_e$  plane that satisfy the  $I_{977}$  and  $I_{1176}$  observations (labeled "ratio") and of points that satisfy the  $I_{977}$  and  $\tau_c(\lambda 977)$  observations (labeled "τ"). Numbers in parentheses are  $\bar{g}(\lambda 977)$  and  $\bar{g}(\lambda 1176)$  used in calculating each curve.

In Figure 47, the straight sloping line defines  $N_e T_e = 6 \times 10^{14}$ , which is the transition-region value proposed by Dupree and Goldberg (1967). We have placed arrows on the  $T_e$  axis to indicate the temperatures at which C III composes 90 and 50% of the total amount of carbon. It would be hoped that upon using the best available values of  $G_1$  and  $G_2$ , we would arrive at a point in Figure 47 where C III is the dominant form of carbon. We find that in fact all the points for consistent  $(G_1, G_2)$  pairs do fall at temperatures where C III dominates, so this is no problem.

Many theoretical values for  $G_1$  and  $G_2$  have been calculated. The general formula of Van Regemorter (1962) gives  $G_1 = 0.20$ ,  $G_2 = 0.20$ . But this formula has been shown to underestimate  $\bar{g}$ 's for highly charged ions (Bely,

Tully, and Van Regemorter, 1963). The results of Bely et al. were used by Pottasch (1964) to derive an estimate of  $G_1 = 0.41$ . More recently, detailed calculations have been made by Eissner (quoted by Tondello and McWhirter (1971) and by Jordan (1971)), which have been used by Munro, Dupree, and Withbroe (1971). From the collision strengths used by Jordan, we derive  $G_1 = 0.30$ ,  $G_2 = 0.53$ , while from the collision rates of Munro et al. (1971), we derive  $G_1 = 0.52$ ,  $G_2 = 0.37$ . Since the results of Eissner have not been published, we cannot easily reconcile these discrepancies. The calculated  $G_i$ 's are weak functions of temperature, but this effect will not settle the disparity in these quoted values. We also note that neither of these last two pairs of  $G_i$  values yields a consistent solution, as can be determined by an inspection of Figure 48. On Figure 48, we show by arrows on the  $G_1$  axis the values of this variable given by Van Regemorter, by Bely et al., and by Munro et al.

We desired to make some more detailed calculations of the C III line-formation problem, using the computer code employed in the previous chapters. However, first a choice of  $G_1$  and  $G_2$  had to be made. It was decided that ( $G_1 = 0.40$ ,  $G_2 = 0.42$ ) represents a reasonable choice for the  $G_i$ 's. The average parameters implied for this model by our calculations are the following:

$$\begin{aligned}
 T_e &= 57,400^\circ \text{ ,} \\
 N_e &= 6.61 \times 10^9 \text{ ,} \\
 N_e T_e &= 3.80 \times 10^{14} \text{ ,} \\
 \Delta Z &= 35 \text{ km (not including dilution due to ionization equilibrium) ,} \\
 &= 38 \text{ km (including dilution effects) .}
 \end{aligned}$$

A model of the region of formation of the C III lines was formulated on the basis of these parameters. In Figure 50, we show the variations with height of the temperature, electron density, total hydrogen density, and source function for the  $\lambda 977$  line. We take as our zero point of height that at which  $T_e = 20,000$  K. This atmosphere has a base temperature and density that will fit onto the top of the atmospheres derived in Section 6.

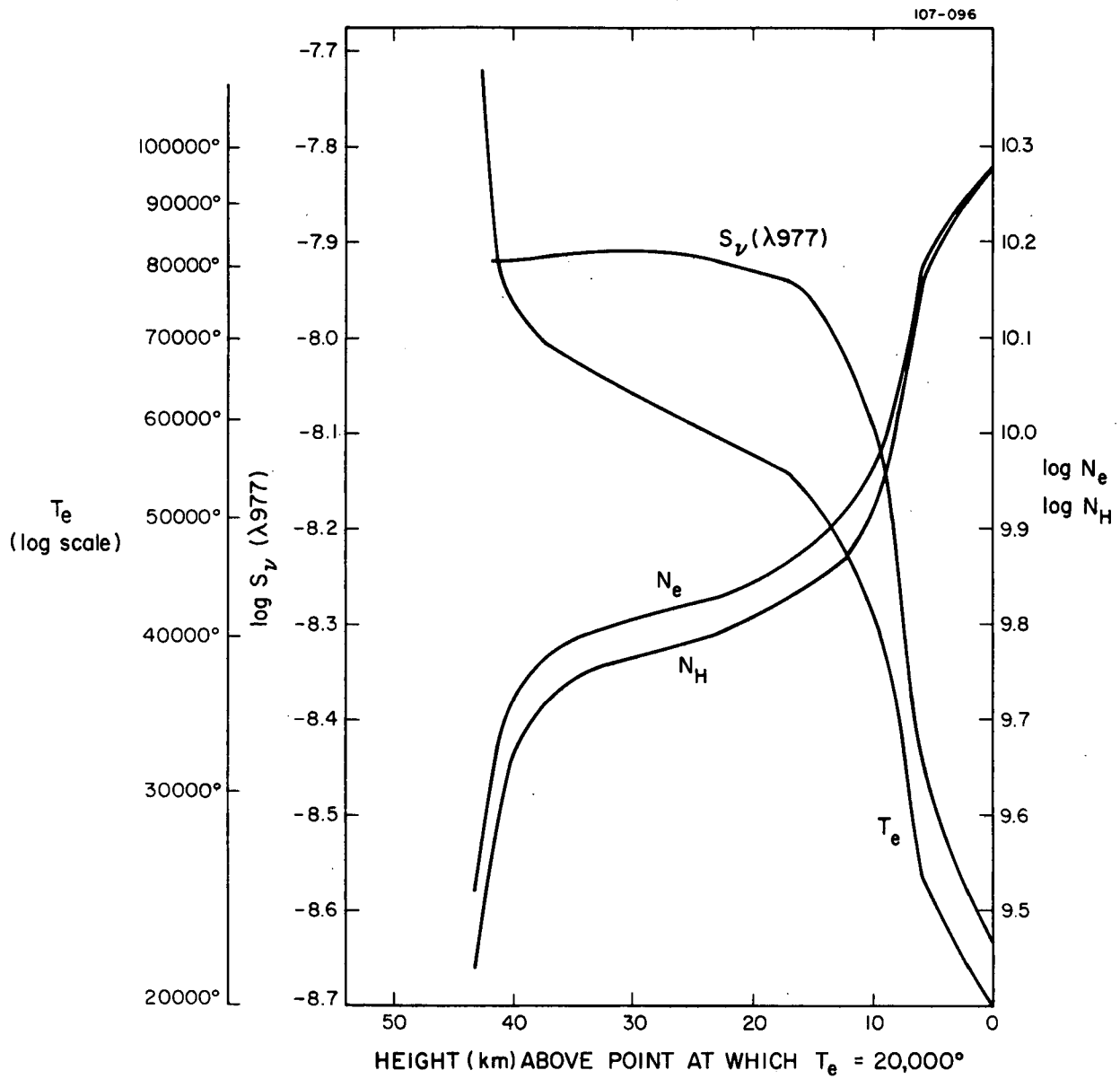


Figure 50. The variation with height of  $T_e$ ,  $N_e$ ,  $N_H$ , and  $S_\nu(\lambda 977)$  for our model of the formation of the C III lines.

The actual derived values of  $\tau_c$ ,  $I_{977}$ , and ratio  $\lambda 977/\lambda 1176$  for this model are 0.564, 845 ergs cm<sup>-2</sup> sec<sup>-1</sup> ster<sup>-1</sup>, and 3.65 instead of the values 0.558, 900, and 3.63 that are observed, but this difference is small compared to the observational errors.

Note that a local maximum of the source function for  $\lambda 977$  occurs near the center of the region of line formation, even though  $\tau_c < 1$  and the temperature increases monotonically outward. It appears that the formation of this line could be reasonably well represented by a layer of constant  $\epsilon B$ , of finite optical depth, as discussed in Section 1. The apparent existence in Figure 50 of a temperature plateau at approximately 60,000 K is not based on any firm observational evidence but rather derives from the somewhat arbitrary way in which the temperature curve was drawn. Our atmosphere has a considerably lower density and greater depth than most previously published models of this portion of the solar atmosphere. For instance, the model by Pottasch (1964) rises from  $T_e = 20,000$  K to  $T_e = 10^5$  K in only 14 km, while  $N_e T_e \sim 7 \times 10^{14}$  as compared with our value of  $N_e T_e \sim 4 \times 10^{14}$ . Since the intensity in a line is proportional to  $N_e^2 \Delta Z$ , where  $\Delta Z$  is the thickness of the layer of line formation, we would expect near agreement of this quantity for the two models, which is in fact found. So to some extent, the only new quantity that we have determined from this study of the C III lines is the value of  $N_e T_e$  in the low transition region.

## 8. CONCLUDING REMARKS

In the chapters on individual lines, we have arrived at several definite or tentative conclusions about the conditions responsible for their formation. Some of these ideas have appeared several times in different sections. Here we bring together our various conclusions and inferences relating to the structure of the solar atmosphere and outline some of the resulting picture of the sun's outer layers.

The temperature-height relation of the solar chromosphere and chromosphere-corona transition region was discussed in Sections 4 through 7. We find that the great intensity of the O I lines implies a chromospheric temperature approximately 500 K greater than that of the HSRA atmosphere in the height range around 1100 km. The Mg II lines are consistent with this conclusion but are not very sensitive to such chromospheric temperature differences. Above the region of Lyman-continuum formation, the C II results imply a temperature plateau, with a temperature and width of close to 19,000 K and 60 km, respectively. At temperatures above 20,000 K, we find from the C III results a rise to 100,000 K in about 43 km, with a slight indication of a smaller temperature gradient near 60,000 K than above or below this point.

These temperature plateaus in the regions of formation of the C II and C III lines deserve further comment. In our calculations, the main evidence for the existence of the plateaus is the limb-brightening data from the OSO 4 satellite. It is possible that effects due to lack of spherical symmetry in the actual line-formation situation might make deductions from limb-brightening data unreliable. For instance, even within the plane-parallel approximation, if one were to consider line formation in a two-component atmosphere wherein most of the emergent radiation comes from the hotter, denser component covering only a fraction of the solar surface, then for a given effective temperature of formation, the optical thickness of a line such as C III  $\lambda$  977 would be considerably increased if we held the total line emission constant.

Conversely, the effective temperature of line formation would be increased for a given optical depth. This would probably have the effect of smoothing out the temperature-height relation between 20,000 and 100,000 K, as deduced from the behavior of the C III lines. For the C II lines, with a given optical depth in the 19,000° plateau, we could hypothesize a larger micro-turbulent velocity than in the last models discussed in Section 6 and thus improve agreement with the observed line profiles. If the large majority of the C II emission occurs in a small fraction of the solar surface, it might be possible to eliminate the 19,000° plateau entirely and model both high-emission and low-emission regions with smooth temperature-height curves. Another model we might consider is that of C II emission in a very rough, or "bumpy," layer, such that the average projected thickness of the layer is a weak function of  $\mu$ , the limb angle. Another very similar model is that of Withbroe (1970a), which postulates the existence of spicules that rise through the emission layer and reduce the visibility of the emission layer near the limb. The spicules must be optically thick in the C II resonance lines and have a relatively low source function. This model might be a reasonably good representation of the true situation, but it would appear that the observed intensity ratio of the two C II lines (between 0.85 and 1.00) argues that these lines are not formed in an optically thin layer, while most models with smoothly rising temperature predict emission from an optically thin layer, if the emission arises from most of the solar surface rather than from a small area thereof.

In the sections on Mg II and O I, and in the Appendix on Ca II, we find that it is useful to assume a microturbulent velocity that rises very rapidly from a value near  $5 \text{ km sec}^{-1}$  to close to  $18 \text{ km sec}^{-1}$ . This increase has the effect of making the central reversals not quite so deep and abrupt as we would otherwise compute. The Mg II and O I (case 10) calculations agree in placing this increase at a height of approximately 1600 km. For Ca II, we treat the microturbulence and source function as functions of K line-center optical depth, but judging from various published calculations (such as Athay and Skumanich, 1968a, b, or Linsky and Avrett, 1970), it seems very unlikely that  $\tau_0 = 10$  in the K line, where we find  $v_t$  increasing rapidly, can occur as high as 1600 km. Apparently this difference is caused by our

attempt to reproduce the effects caused by inhomogeneities through the use of a one-component atmosphere. To investigate this point, it would be valuable to see whether one two-component atmosphere could reproduce the profiles and center-to-limb behavior of Ca II, Mg II, and O I. In the section on C II, we conclude that this microturbulence decreases again near the point where  $T = 10,000$  K (1860 km in the HSRA model) so as to produce a small predicted limb brightening as is observed, but as mentioned above, this is uncertain. More probably, the atmosphere divides into two components, only one of which contributes strongly to the C II emission intensity, and this component has a microturbulent velocity of close to  $16 \text{ km sec}^{-1}$ . A microturbulence of this magnitude will produce line profiles of the observed width.

In the section on C III, we combine the observations of intensity in the  $\lambda 977$  and  $\lambda 1176$  lines with the optical depth of the  $\lambda 977$  line to derive a chromosphere-corona transition-region value for  $N_e T_e$  of  $3.8 \times 10^{14}$  and a thickness between 30,000 and 80,000° of approximately 40 km. Other authors have usually found  $N_e T_e$  values that are higher, between 6 and  $10 \times 10^{14}$ . Of course, the fact that some of the necessary atomic cross sections are poorly known makes our value subject to revision. Nussbaumer (1971) has very recently derived some new relevant data.

In order to make clear those atomic parameters that we feel are most important in interpreting the various lines we have dealt with, we present in Table 9 a list of critical atomic parameters for four ions. Some of the quantities listed are already relatively well determined, but most are not. It is hoped that this list will encourage the study of these critical atomic parameters.

Finally, we shall make some general remarks on the problem of matching observed and computed line profiles. For lines formed in the chromosphere, such as Mg II and O I (and probably C I, N I, and others), most computed profiles show very narrow emission peaks, with deeply reversed cores, while observations always show much more rounded and broader emission peaks, with absorption cores that are not very deep. One is tempted

Table 9. Critical atomic parameters.

Ion	Atomic quantity	Observational relevance
Mg II	a) Van der Waals broadening	Line profiles, center-to-limb behavior
	b) Collisional cross section	Intensity
	c) Fine-structure cross section	Ratio of H and K lines
O I	a) Hydrogen charge-transfer rate	Ionization tied to hydrogen
	b) Collisional ionization cross section	Ionization equilibrium for $T > 10,000^\circ$ if a) is small
	c) Radiative and dielectronic recombination	Ionization equilibrium if a) is small
	d) $^3S^0$ excitation cross section	Intensity
	e) Line-broadening constants	Limb brightening, line profiles, and ratios of different lines
	f) f values for $\lambda$ 1302, $\lambda$ 1304, and $\lambda$ 1306	Intensity
C II	a) Fine-structure cross sections for $^2D$ levels	Ratio of two lines
	b) Collisional rates to $^4P$ level	Intensity, intensity ratio
	c) Collisional cross sections for $\lambda$ 1334, $\lambda$ 1336 lines	Intensity, intensity ratio
	d) f value of $\lambda$ 1334 and $\lambda$ 1336 lines	Limb-brightening behavior
C III	a) Collisional cross sections of $\lambda$ 977, $\lambda$ 1176, and $^1S-^3P^0$ and $^3P^0-^1P^0$ transitions	Intensity, intensity ratio
	b) f value for $\lambda$ 977	Limb-brightening behavior
	c) A value for $^3P_1^0 \rightarrow ^1S$	Intensity ratio

to attribute this discrepancy to macroturbulence, which will smear the underlying "true" solar profile. But if this is the case, it should be possible through the use of instruments with high spatial resolution to resolve the individual macroturbulent elements and see the "true" solar profile. Thus far, for the Mg II H and K lines, on which the most work has been done, there is very little indication that higher spatial resolution produces observed profiles similar to those usually computed. Apparently the situation is more complex than either pure macroturbulence or pure microturbulence, or even a combination of the two. Atmospheric motions that strongly affect the line profiles must be taking place on scales very similar to the characteristic thicknesses of line-formation regions, producing an intermediate form of turbulence, for which no satisfactory mathematical methods of treatment have been advanced.

## 9. ACKNOWLEDGMENTS

First and foremost, I wish to express my thanks to Dr. Eugene H. Avrett for advice and many useful discussions during all phases of my work and for the devising and continuous updating of PANDORA. I also owe special thanks to Dr. George L. Withbroe for discussions about the C III lines and the OSO data and to Rudolf Loeser for help in resolving some questions concerning the use of PANDORA.

Others at the Harvard College Observatory and at the Smithsonian Astrophysical Observatory who have contributed to my knowledge of the sun include Dr. Robert W. Noyes, Dr. Andrea K. Dupree, Richard H. Munro, Dr. Wolfgang Kalkofen, and Jorge Vernazza, all of whom I thank.

Finally, I acknowledge my debt to the Smithsonian Research Foundation for support via a Smithsonian Research Fellowship during most of my work on this thesis.

During the past year, this research has been supported by the National Aeronautics and Space Administration under contract NAS 5-9274 and grant NGR 22-007-211.

10. REFERENCES

- AITKEN, K. L., HARRISON, M. F. A., and RUNDEL, R. D.  
 1971. Measurement of the cross section for electron impact ionization of multi-electron ion II.  $N^{2+}$  to  $N^{3+}$  and  $C^+$  to  $C^{2+}$ . Journ. Phys. B: Atom. Molec. Phys., vol. 4, pp. 1189-1199.
- ALLEN, C. W.  
 1961. Solar ultraviolet and x-ray line emission. Mem. Soc. Roy. Sci. Liège, ser. 5, vol. 4, pp. 241-250.
- ALLEN, J. W., and DUPREE, A. K.  
 1969. Calculations of ionization equilibria for oxygen, neon, silicon, and iron. Astrophys. Journ., vol. 155, pp. 27-36.
- ATHAY, R. G.  
 1966. Theoretical line intensities. V. Solar UV emission lines of heavy elements. Astrophys. Journ., vol. 145, pp. 784-795.  
 1969. Boundary conditions on model solar chromospheres. Solar Phys., vol. 9, pp. 51-55.  
 1970. A non-LTE line-blanketed solar model. Astrophys. Journ., vol. 161, pp. 713-736.
- ATHAY, R. G., and CANFIELD, R. C.  
 1969. Computed profiles for solar Mg-b and Na D lines. Astrophys. Journ., vol. 156, pp. 695-706.  
 1970. A self-consistent model atmosphere program with applications to solar O I resonance lines. In Spectrum Formation in Stars with Steady-State Extended Atmospheres, N. B. S. Spec. Publ. 332, Washington, D.C.
- ATHAY, R. G., MENZEL, D., PECKER, J. -C., and THOMAS, R. N.  
 1955. The thermodynamic state of the outer solar atmosphere V. A model of the chromosphere from the continuum emission. Astrophys. Journ. Suppl., vol. 1, pp. 505-519.
- ATHAY, R. G., and SKUMANICH, A.  
 1967. An integral equation for the line source function and its numerical solution. Ann. d'Astrophys., vol. 30, pp. 669-676.

ATHAY, R. G., and SKUMANICH, A.

1968a. Emission cores in H and K lines. I. The optically thick chromosphere. *Solar Phys.*, vol. 3, pp. 181-203.

1968b. Emission cores in H and K lines. IV. Center-to-limb variation. *Solar Phys.*, vol. 4, pp. 176-184.

AVRETT, E. H.

1965. Solutions of the two-level line transfer problem with complete redistribution. *Smithsonian Astrophys. Obs. Spec. Rep. No. 174*, pp. 101-142.

1969. Lectures on the theory of line formation. Lectures delivered at UCLA, Feb. 10-28, 1969 (unpublished).

1971. Solution of non-LTE transfer problems. *Journ. Quant. Spectrosc. Radiat. Trans.*, in press.

AVRETT, E. H., and HUMMER, D. G.

1965. Non-coherent scattering II: Line formation with a frequency independent source function. *Mon. Not. Roy. Astron. Soc.*, vol. 130, pp. 295-331.

AVRETT, E. H., and LOESER, R.

1963. A simple and accurate method for the evaluation of the Milne integrals. *Journ. Quant. Spectrosc. Radiat. Trans.*, vol. 3, pp. 201-208.

1966. Kernel representations in the solution of line-transfer problems. *Smithsonian Astrophys. Obs. Spec. Rep. No. 201*, 114 pp.

1969. Formation of line and continuous spectra. I. Source-function calculations. *Smithsonian Astrophys. Obs. Spec. Rep. No. 303*, 98 pp.

BAHCALL, J. N., and WOLF, R. A.

1968. Fine-structure transitions. *Astrophys. Journ.*, vol. 152, pp. 701-730.

BAKER, J. G., ALLER, L. H., and MENZEL, D. H.

1939. Physical processes in the gaseous nebulae. VII. The transfer of radiation in the Lyman continuum. *Astrophys. Journ.*, vol. 90, pp. 271-280.

BEEBE, H. A.

1971. Formation of the Ca II K-line core with arbitrary temperature minima. *Solar Phys.*, vol. 17, pp. 304-315.

- BEEBE, H. A., and JOHNSON, H. R.  
 1969. Ca II resonance lines in non-homogeneous chromospheres. *Solar Phys.*, vol. 10, pp. 79-87.
- BELY, O., and FAUCHER, P.  
 1970. Fine structure proton excitation rates for positive ions in the  $2p$ ,  $2p^5$ ,  $3p$ ,  $3p^5$  series. *Astron. Astrophys.*, vol. 6, pp. 88-92.
- BELY, O., TULLY, J., and VAN REGEMORTER, H.  
 1963. L'excitation des atomes par chocs électroniques, application à l'excitation des transitions de resonance dans les series isoélectroniques du lithium et du sodium. *Ann. Phys.*, vol. 8, pp. 303-321.
- BERGER, R. A., BRUNER E. C., Jr., and STEVENS, R. J.  
 1970. Solar C II resonance line profiles. *Solar Phys.*, vol. 12, pp. 370-378.
- BLAHA, M.  
 1968. Collisional excitations of positive ions in  $p^q$  configurations: Transitions between levels of the P term, Part I. *Ann. d'Astrophys.*, vol. 31, pp. 311-321.  
 1969. Collisional excitation of positive ions in  $p^q$  configurations: Transitions between levels of the P term, Part II. *Astron. Astrophys.*, vol. 1, pp. 42-43.
- BÖHM-VITENSE, E.  
 1954. Über die Temperatur- und Druckschichtung der Sonnenatmosphäre. *Zeits. f. Astrophys.*, vol. 34, pp. 209-228.
- BRUNER, E. C., Jr., JONES, R. A., RENSE, W. A., and THOMAS, G. E.  
 1970. Ultraviolet line profiles of O I in the solar spectrum. *Astrophys. Journ.*, vol. 162, pp. 281-285.
- BRUNER, E. C., Jr., and RENSE, W. A.  
 1969. Rocket observations of solar ultraviolet emission lines. *Astrophys. Journ.*, vol. 157, pp. 417-424.
- BURGESS, A., and SEATON, M. J.  
 1960. A general formula for the calculation of atomic photo-ionization cross sections. *Mon. Not. Roy. Astron. Soc.*, vol. 120, pp. 121-151.

BURGESS, A., and SOMMERS, H. P.

1969. The effects of electron and radiation density on dielectronic recombination. *Astrophys. Journ.*, vol. 157, pp. 1007-1021.

CHAMARAUX, P.

1967. Calcul des raies du sodium neutre dans le spectre solaire sans l'hypothèse de l'équilibre thermodynamique local. *Ann. d'Astrophys.*, vol. 30, pp. 67-84.

CILLIE, G.

1932. The hydrogen emission in gaseous nebulae. *Mon. Not. Roy. Astron. Soc.*, vol. 92, pp. 820-831.

CORLISS, C. H., and BOZMAN, W. R.

1962. Experimental transition probabilities for spectral lines of seventy elements. N. B. S. Mono. 53, Washington, D. C.

CUNY, Y.

1967. Détermination exacte de la structure stationnaire d'une atmosphère d'hydrogène. *Ann. d'Astrophys.*, vol. 30, pp. 143-183.  
1968. Contribution à l'étude du spectre solaire de l'hydrogène. *Solar Phys.*, vol. 3, pp. 204-240.

DALGARNO, A., and DEGGES, T. C.

1968. Electron cooling in the upper atmosphere. *Planet. Space Sci.*, vol. 16, pp. 125-127.

DEFOUW, R. J.

1970. Thermal instability of a model hydrogen plasma. *Astrophys. Journ.*, vol. 161, pp. 55-66.

DETWILER, C. R., GARRETT, D. L., PURCELL, J. P., and TOUSEY, R.

1961. The intensity distribution in the ultraviolet solar spectrum. *Ann. de Géophys.*, vol. 17, pp. 263-272.

DUMONT, S.

1966. Étude de la fonction source avec une largeur Doppler variable. *Comptes Rendus*, vol. 262, pp. 740-743.  
1967a. Formation des raies du Ca II et du Mg II dans la basse chromosphère. *Ann. d'Astrophys.*, vol. 30, pp. 421-437.  
1967b. Contribution à l'étude de la zone de transition entre la photosphère et la chromosphère à partir des raies de résonance de Ca II et Mg II. *Ann. d'Astrophys.*, vol. 30, pp. 861-885.

- DUPREE, A. K., and GOLDBERG, L.  
1967. Solar abundance determination from ultraviolet emission lines. *Solar Phys.*, vol. 1, pp. 229-241.
- DUPREE, A. K., and REEVES, E. M.  
1971. The extreme ultraviolet spectrum of the quiet sun. *Astrophys. Journ.*, vol. 165, pp. 599-614.
- EDDY, J. A., LÉNA, P. J., and MacQUEEN, R. M.  
1969. Far infrared measurement of the solar minimum temperature. *Solar Phys.*, vol. 10, pp. 330-341.
- ELSTE, G.  
1968. Comments on the Bilderberg Continuum Atmosphere. *Solar Phys.*, vol. 3, pp. 106-117.
- ELWERT, G.  
1952. Über die Ionisations- und Rekombinationsprozesse in einem Plasma und die Ionisationsformel der Sonnenkorona. *Zeits. f. Naturforschung*, vol. 7a, pp. 432-439.
- ENGVOLD, O.  
1966. On the center-limb variation of the H- and K-lines of Ca II. *Astrophys. Norvegica*, vol. 10, pp. 101-125.
- FEAUTRIER, P.  
1964. Sur la résolution numérique de l'équation de transfert. *Comptes Rendus*, vol. 258, pp. 3189-3191.
- FIELD, G. B.  
1965. Thermal instability. *Astrophys. Journ.*, vol. 142, pp. 531-567.
- FIELD, G. B., and STEIGMAN, G.  
1971. Charge transfer and ionization equilibrium in the interstellar medium. *Astrophys. Journ.*, vol. 166, pp. 59-64.
- FINN, G. D.  
1967. Frequency redistribution on scattering. *Astrophys. Journ.*, vol. 147, pp. 1085-1089.
- FINN, G. D., MUGGLESTONE, D., and YOUNG, R. L.  
1967. The solar sodium D-lines II. Scattering profiles. *Mon. Not. Roy. Astron. Soc.*, vol. 137, pp. 445-462.
- GARSTANG, R. H., and SHAMEY, L. J.,  
1967. Intercombination-line oscillator strengths in the helium and beryllium isoelectronic sequences. *Astrophys. Journ.*, vol. 148, pp. 665-666.

GINGERICH, O.

1970. A new solar model. Unpublished.

GINGERICH, O., and de JAGER, C.

1968. The Bilderberg model of the photosphere and low chromosphere.  
Solar Phys., vol. 3, pp. 5-24.

GINGERICH, O., NOYES, R. W., KALKOFEN, W., and CUNY, Y.

1971. The Harvard-Smithsonian Reference Atmosphere. Solar Phys.,  
in press.

GIOVANELLI, R. G.

1949. The hydrogen spectrum of the sun. Mon. Not. Roy. Astron. Soc.,  
vol. 109, pp. 298-323.

GOLDBERG, L.

1965. Observational requirements for a theory of formation of H and  
K lines. In Proc. Second Harvard-Smithsonian Conf. on Stellar  
Atmospheres, Smithsonian Astrophys. Obs. Spec. Rep. No.  
174, pp. 389-396.

GOLDBERG, L., MÜLLER, E. A., and ALLER, L. H.

1960. The abundances of the elements in the solar atmosphere. Astro-  
phys. Journ. Suppl., No. 5, pp. 1-138.

GRIEM, H. R.

1964. Plasma Spectroscopy. McGraw-Hill Book Co, New York.

HEINTZE, J. R. W., HUBENET, H., and de JAGER, C.

1964. A reference model of the solar photosphere and low chromosphere.  
Bull. Astron. Neth., vol. 17, pp. 442-445.

HENRY, R. J. W.

1970. Photoionization cross-sections for atoms and ions of carbon,  
nitrogen, oxygen and neon. Astrophys. Journ., vol. 161,  
pp. 1153-1155.

HENRY, R. J. W., and WILLIAMS, R. E.

1968. Collision strengths and photoionization cross sections for nitrogen,  
oxygen and neon. Publ. Astron. Soc. Pac., vol. 80, pp. 669-679.

HINTEREGGER, H. E.

1965. Absolute intensity measurements in the extreme ultraviolet spec-  
trum of solar radiation. Space Sci. Rev., vol. 4, pp. 461-497.

HOUSE, L. L.

1964. Ionization equilibrium of the elements from H to Fe. *Astrophys. Journ. Suppl.*, No. 8, pp. 307-328.

HOUTGAST, J.

1965. Absolute intensities in high dispersion solar spectra between  $\lambda$  3000 and  $\lambda$  4000 Angstroms. *Proc. Kon. Nederl. Acad. Wetensch. Amst.*, vol. 68, ser. B, pp. 306-310.

HUMMER, D. G.

1968. Non-coherent scattering. III. The effect of continuous absorption on the formation of spectral lines. *Mon. Not. Roy. Astron. Soc.*, vol. 138, pp. 73-108.
1969. Non-coherent scattering. VI. Solutions of the transfer problem with a frequency-dependent source function. *Mon. Not. Roy. Astron. Soc.*, vol. 145, pp. 95-120.

JEFFERIES, J. T.

1960. The source function in a non-equilibrium atmosphere. VII. The interlocking problem. *Astrophys. Journ.*, vol. 132, pp. 775-789.
1968. Spectral Line Formation. Blaisdell Publ. Co., Waltham, Mass.

JEFFERIES, J. T., and WHITE, O. R.

1960. The source function in a non-equilibrium atmosphere. VI. The frequency dependence of the source function for resonance lines. *Astrophys. Journ.*, vol. 132, pp. 767-774.

JOHNSON, H. R.

1964. A theoretical study of the excitation of sodium in the solar photosphere. *Ann. d'Astrophys.*, vol. 27, pp. 695-707.

JORDAN, C.

1969. The ionization equilibrium of elements between carbon and nickel. *Mon. Not. Roy. Astron. Soc.*, vol. 142, pp. 501-521.
1971. The relative intensities of lines from Be I-like ions in the solar spectrum. To be published.

KALKOFEN, W.

- 1968a. The simultaneous solution of strongly coupled transfer equations. In Resonance Lines in Astrophysics, Proc. Conf. held at National Center for Atmospheric Research, Boulder, Colorado, Sept. 1968, pp. 3-26.

KALKOFEN, W.

- 1968b. Mapping methods in radiative transfer. In Resonance Lines in Astrophysics, Proc. Conf. held at National Center for Atmospheric Research, Boulder, Colorado, Sept. 1968, pp. 65-78.

KORFF, S. A.

1932. On the measurement and interpretation of Fraunhofer lines. *Astrophys. Journ.*, vol. 76, pp. 291-298.

LAWRENCE, G. M.

1969. Vacuum ultraviolet transition probabilities in C, N, O and N<sub>2</sub>. *Can. Journ. Chem.*, vol. 47, pp. 1856-1857.

LAWRENCE, G. M., and SAVAGE, B. D.

1966. Radiative lifetimes of UV multiplets in boron, carbon, and nitrogen. *Phys. Rev.*, vol. 141, pp. 67-70.

LEMAIRE, P.

1969. High resolution balloon spectra of the sun in the Mg II doublet lines II. *Astrophys. Journ. Lett.*, vol. 3, pp. 43-48.

LINSKY, J. L.

1968. Calcium line formation in the solar chromosphere. *Smithsonian Astrophys. Obs. Spec. Rep. No. 274*, 3 vols.

LINSKY, J. L., and AVRETT, E. H.

1970. The solar H and K lines. *Publ. Astron. Soc. Pac.*, vol. 82, pp. 169-248.

MANKIN, W. G., and STRONG, J.

1969. Solar far-infrared radiation (abstract). *Bull. Am. Astron. Soc.*, vol. 1, p. 200.

McCREA, W. H.

1929. The mechanics of the chromosphere. *Mon. Not. Roy. Astron. Soc.*, vol. 89, pp. 718-730.

MILNE, E. A.

1930. Thermodynamics of the stars. In *Handbuch der Astrophysik*, Springer-Verlag, Berlin, vol. 3, part 1, pp. 65-255.

MINNAERT, M.

1953. The photosphere. In The Sun, ed. by G. P. Kuiper, Univ. of Chicago Press, Chicago, pp. 88-185.

MIYAMOTO, S.

1954. Contours of strong Fraunhofer lines. *Publ. Astron. Soc. Japan*, vol. 6, pp. 140-149.

- MOORE, C. E.  
 1949. Atomic Energy Levels, Vol. I. N.B.S. Circ. 467, Washington, D.C.
- MUNRO, R. H., DUPREE, A. K., and WITHBROE, G. L.  
 1971. Electron densities derived from line intensity ratios: Beryllium isoelectronic sequence. *Solar Phys.*, vol. 19, pp. 347-355.
- NOYES, R. W., and KALKOFEN, W.  
 1970. The solar Lyman continuum and the structure of the solar chromosphere. *Solar Phys.*, vol. 15, pp. 120-138.
- NOYES, R. W., WITHBROE, G. L., and KIRSCHNER, R. P.  
 1970. Extreme ultraviolet observations of active regions in the chromosphere and the corona. *Solar Phys.*, vol. 11, pp. 388-398.
- NUSSBAUMER, H.  
 1971. *Astron. Astrophys.* (in press).
- OSTERBROCK, D. E.  
 1970. Excitation of C III  $\lambda$  1909 and other semiforbidden emission lines in QSO's and nebulae. *Astrophys. Journ.*, vol. 160, pp. 25-30.
- PARKES, D. A., KEYSER, L. F., and KAUFMAN, F.  
 1967. Oscillator strength of the resonance triplet of atomic oxygen. *Astrophys. Journ.*, vol. 149, pp. 217-224.
- PARKINSON, W. H., and REEVES, E. M.  
 1969. Measurements in the solar spectrum between 1400 and 1875 Å with a rocket-borne spectrometer. *Solar Phys.*, vol. 10, pp. 342-348.  
 1970. Quoted by Gingerich, Noyes, Kalkofen, and Cuny (1971).
- PEACH, G.  
 1967. A revised general formula for the calculation of atomic photoionization cross sections. *Mem. Roy. Astron. Soc.*, vol. 71, pp. 13-27.
- PLASKETT, H. H.  
 1931. The formation of the magnesium b lines in the solar atmosphere. *Mon. Not. Roy. Astron. Soc.*, vol. 91, pp. 870-933.
- POTTASCH, S. R.  
 1964. On the interpretation of the solar ultraviolet emission line spectrum. *Space Sci. Rev.*, vol. 3, pp. 816-855.

POTTASCH, S. R., and THOMAS, R. N.

1960. Thermodynamic structure of the outer solar atmosphere. VI. Effect of departures from the Saha equation on inferred properties of the low chromosphere. *Astrophys. Journ.*, vol. 132, pp. 195-201.

REEVES, E. M., and PARKINSON, W. H.

- 1970a. An atlas of extreme-ultraviolet spectroheliograms from OSO-IV. *Astrophys. Journ. Suppl.*, vol. 21, pp. 1-30.
- 1970b. Calibration changes in EUV solar satellite instrumentation. *Appl. Opt.*, vol. 9, pp. 1201-1208.

ROSSELAND, S.

1926. On the origin of bright lines in stellar spectra. *Astrophys. Journ.*, vol. 63, pp. 218-235.

SARAPH, H. E., SEATON, M. J., and SHEMMING, J.

1969. Excitation of forbidden lines in gaseous nebulae. I. Formulation and calculations for  $2P^q$  ions. *Phil. Trans. Roy. Soc.*, vol. A264, pp. 77-105.

SCHUSTER, A.

1905. Radiation through a foggy atmosphere. *Astrophys. Journ.*, vol. 21, pp. 1-22.

SEATON, M. J.

1964. The spectrum of the solar corona. *Planet. Space Sci.*, vol. 12, pp. 55-74.

STAUFFER, A. D., and McDOWELL, M. R. C.

1966. An impact parameter treatment of the excitation of atoms by charged particles. *Proc. Phys. Soc.*, vol. 89, pp. 289-298.

STONE, E. J., and ZIPF, E. C.

1971. Excitation of the O I ( $^3S$ ) and N I ( $^4P$ ) resonance states by electron impact on O and N. *Phys. Rev. A*, vol. 4, pp. 610-613.

THOMAS, R. N.

1948. Superthermic phenomena in stellar atmospheres. II. Departure from thermodynamic equilibrium in an idealized chromosphere. *Astrophys. Journ.*, vol. 108, pp. 142-152.

THOMAS, R. N.

1957. The source function in a non-equilibrium atmosphere. I. The resonance lines. *Astrophys. Journ.*, vol. 125, pp. 260-274.

1965. Some Aspects of Non-Equilibrium Thermodynamics in the Presence of a Radiation Field. University of Colorado Press, Boulder, Colorado.

THOMAS, R. N., and ATHAY, R. G.

1961. Physics of the Solar Chromosphere. Interscience Publ. Co., New York.

THOMAS, R. N., and GEBBIE, K. B.

1971. The solar chromosphere and the general structure of a stellar atmosphere. In Menzel Symposium on Solar Physics, Atomic Spectra and Gaseous Nebulae. NBS Spec. Publ., pp. 84-111, in press.

TOMITA, Y.

1960. On the interpretation of the Fraunhofer line Na D<sub>1</sub>. *Publ. Astron. Soc. Japan*, vol. 12, pp. 524-551.

TONDELLO, G., and McWHIRTER, R. W. P.

1971. Measurements of excitation coefficients for singlet and triplet transitions of neon VIII. *Journ. Phys. B.*, to be published.

VAN REGEMORTER, H.

1962. Rate of collisional excitation in stellar atmospheres. *Astrophys. Journ.*, vol. 136, pp. 906-915.

VERNAZZA, J., AVRETT, E. H., and LOESER, R.

1971. In preparation.

WHITE, O. R., and SUEMOTO, Z.

1968. A measurement of the solar H and K profiles. *Solar Phys.*, vol. 3, pp. 523-530.

WIESE, W. L., SMITH, M. W., and GLENNON, B. M.

1966. Atomic Transition Probabilities, vol. I. Government Printing Office, Washington, D. C.

WIESE, W. L., SMITH, M. W., and MILES, B. M.

1969. Atomic Transition Probabilities, vol. II. Government Printing Office, Washington, D. C.

WITHBROE, G. L.

1970a. Solar XUV limb brightening observations. II. Lines formed in the chromospheric-coronal transition region. *Solar Phys.*, vol. 11, pp. 208-221.

1970b. Solar XUV limb brightening observations. I. The lithium-like ions. *Solar Phys.*, vol. 11, pp. 42-58.

WOFSEY, S., REID, R. H. G., and DALGARNO, A.

1971. Spin-change scattering of C II and O I by atomic hydrogen. *Astrophys. Journ.*, vol. 168, pp. 161-167.

ZIRKER, J. B.

1968. The solar H and K lines of ionized calcium. *Solar Phys.*, vol. 3, pp. 164-180.

APPENDIX  
SOME REMARKS ON THE Ca II K LINE PROFILES

## APPENDIX

## SOME REMARKS ON THE Ca II K LINE PROFILES

Since the following work uses a different method of approach to the problem of solar line profiles from that which we have used in Sections 4 through 7, it was felt best to place this work in a separate appendix. Since so many investigators have studied the formation of the H and K lines of Ca II, we did not feel it worthwhile to go over the same ground once more. Instead, we have studied a restricted problem, which may be of some use as a guide for more extensive and more self-consistent work in which a computer program such as PANDORA is used.

The H and K lines of Ca II have been extensively studied, and many attempts have been made to explain the profiles of the central portions of these lines in the solar spectrum. Engvold (1966) and later Zirker (1968) devised iterative methods of extracting the source function ( $S_K$ ) and micro-turbulent velocity ( $v_t$ ) as functions of optical depth directly from the observed line profiles. Later authors, including Athay and Skumanich (1968), have criticized the conclusions of Engvold and Zirker, saying that the iterative methods do not yield unique results and that the peaks in the source functions obtained by them almost certainly occur at unrealistically small optical depths.

More recently, Beebe and Johnson (1969) and Beebe (1971) have attempted to explain the variation of the H and K line profiles across the solar disk by means of a two-component model atmosphere. These two studies are not wholly self-consistent, however, in that interaction between the two components of the atmosphere is not considered.

We report here an attempt to find the extent to which a plane-parallel, one-component model can reproduce the observed solar profiles. While it is clear from photographs taken in the K line of Ca II that the region of the solar atmosphere where this line is formed has a complex structure and is by no means homogeneous, we feel that the model of a plane-parallel atmosphere should nevertheless be capable of yielding information about the true sun. Athay and Skumanich computed profiles for a series of proposed depth variations of Doppler width, computing  $S_K$  from the given atmospheric model. We note that none of their graphs shows limb darkening at all wavelengths, as is certainly required by the data of Zirker. We have computed a series of line profiles for several assumed variations of  $v_t$  and  $S_K$  with optical depth. Our curves of  $v_t$  and  $S_K$  have not been defined parametrically but have been chosen by a successive-trial method, using information from previous cases as judiciously as possible. Our "best" profiles are shown in Figure A-1, where the solid lines represent observations at  $\mu = 1.0$  from White and Suemoto (1968) and at  $\mu = 0.6$ ,  $\mu = 0.3$ , and  $\mu = 0.1$  from Zirker (1968). We have averaged the red and blue sides of the observed profile in each case. Our adopted intensity for the continuum at  $\lambda 3933$  is  $2.27 \times 10^{-5}$  erg cm<sup>-2</sup> sec<sup>-1</sup> ster<sup>-1</sup> Hz<sup>-1</sup>, as derived by Linsky and Avrett (1970) from the data of Houtgast (1965). This intensity corresponds to  $B_v$  (6450 K). The corresponding dashed curves in Figure A-1 represent our "best-fit" profiles at these same  $\mu$  points. The curves of  $v_t$  (in km sec<sup>-1</sup>) and  $S_K$  (in units of ergs cm<sup>-2</sup> sec<sup>-1</sup> ster<sup>-1</sup> Hz<sup>-1</sup>) corresponding to the dashed profiles in Figure A-1 are shown in Figure A-2.

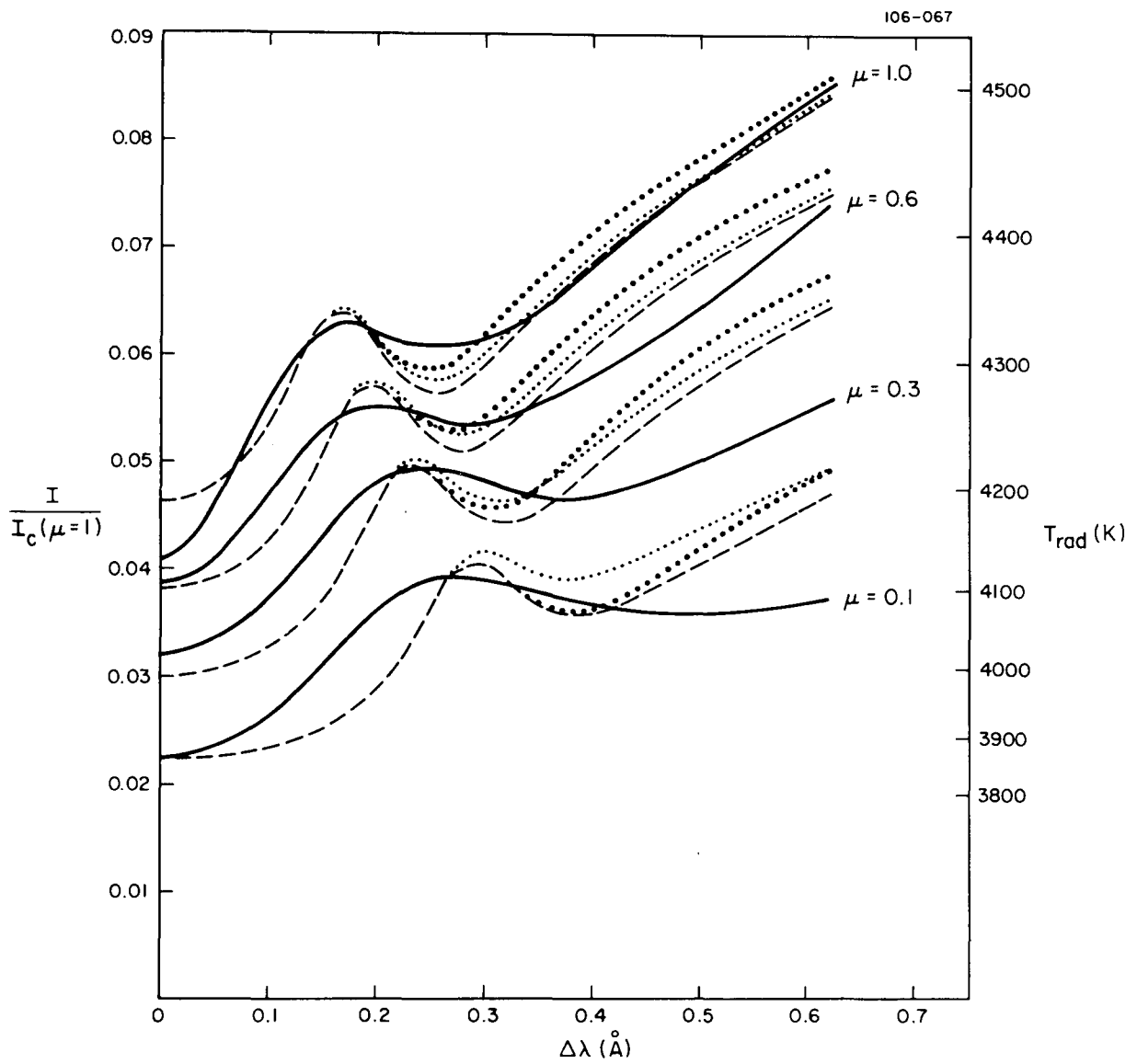


Fig.A-1. Observed and computed profiles for the K line. Solid lines: observations of White and Suemoto (1968) and Zirker (1968); dashed lines: "best-fit" computed profiles; light dotted lines: first alternative set of profiles; heavy dotted lines: second alternative set of profiles.

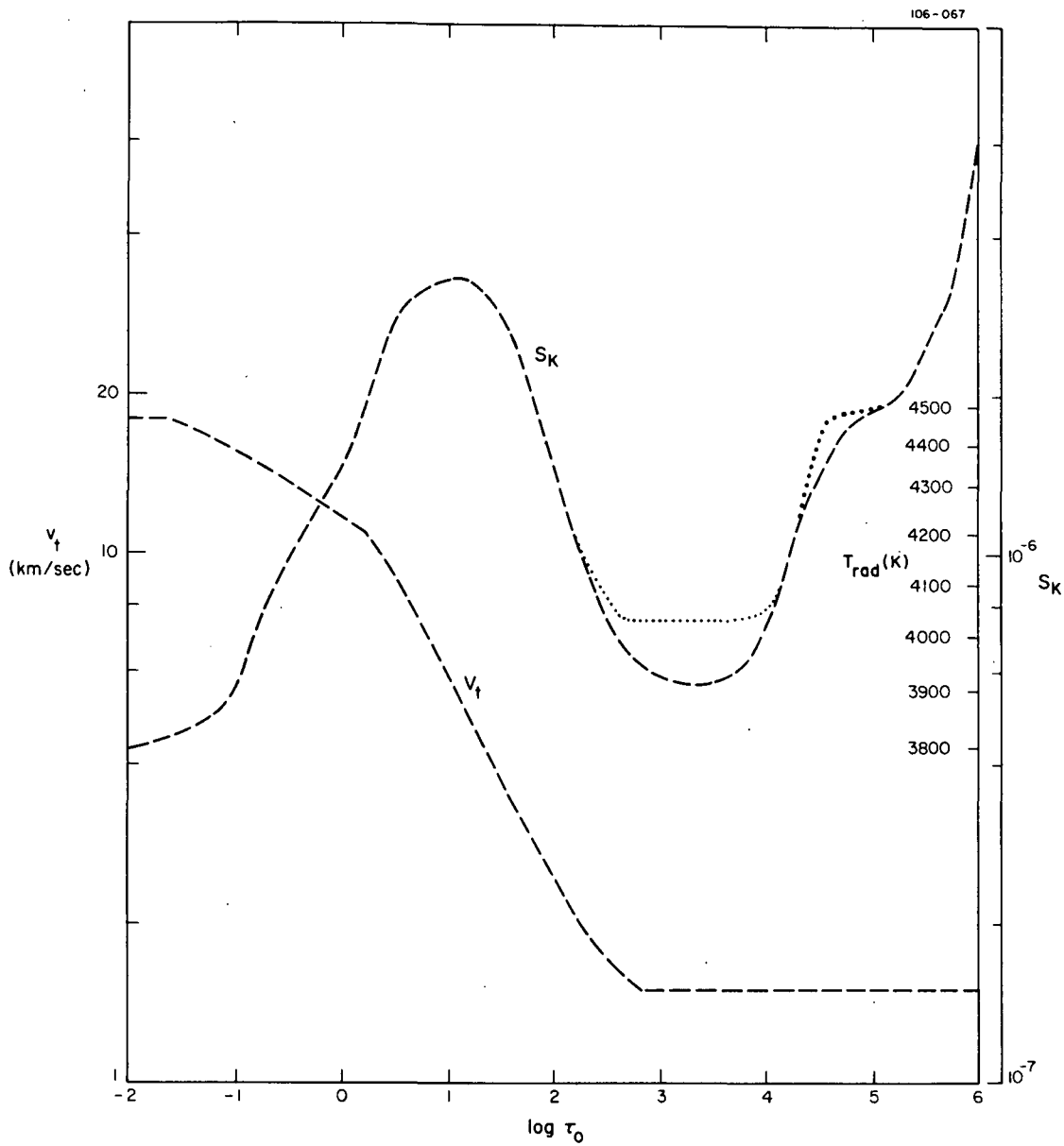


Fig. A-2. Source function ( $S_K$ ) and microturbulent velocity ( $v_t$ ) plotted vs. line-center optical depth ( $\tau_0$ ). Dashed lines: curves corresponding to "best-fit" computed profiles; light dotted line: variation in  $S_K$  for first alternative set of profiles; heavy dotted line: variation in  $S_K$  for second alternative set of profiles.

For all the computations shown here, we have used Voigt profiles for the atomic absorption profile. We have included damping due to natural broadening, collisions with neutral hydrogen atoms, and collisions with electrons. Since natural broadening is the dominant source of damping in most of the regions of the solar atmosphere considered here, we do not tabulate our broadening constants at each optical depth. We used values similar to those in the computations reported by Linsky and Avrett (1970).

The theoretical profiles given here are in much closer agreement with the observations than are those of Athay and Skumanich and are in at least as good agreement as are those of Zirker. Defining  $\Delta\lambda_2$  as the wavelength displacement from line center to the peak intensity point, we find that the computed variation of  $\Delta\lambda_2$  with  $\mu$  is very close to the observations of this quantity. On the basis of the calculated results, we conclude the following:

(1) In order to obtain computed limb darkening at all wavelengths, as is observed, the variation of  $v_t$  with depth must be such that the region of large  $S_K$  and then decreasing  $S_K$  with increasing line-center optical depth has practically no effect on the emergent line profiles. In our model, this is achieved by the rapid decrease in  $v_t$  from  $\log \tau_0 = 0.2$  to  $\log \tau_0 = 3.0$ . This decrease results in the fact that for  $\Delta\lambda > 0.25 \text{ \AA}$ , the region  $0.2 < \log \tau_0 < 3.4$  is optically thin and contributes very little emergent radiation, while for  $\Delta\lambda < 0.25 \text{ \AA}$ , the region above  $\log \tau_0 = 0.2$  has sufficient optical thickness to obscure the region  $\log \tau_0 > 0.2$ . Conversely, since the region  $0.2 < \log \tau_0 < 3.4$  does not affect the emitted profiles, the source function in this region is very poorly determined and has been chosen primarily so that the outward increase in the line source function occurs over the same region in  $\log \tau_0$  as the greatest increase in microturbulent velocity. This feature would be expected theoretically, as has been pointed out by Athay and Skumanich (1968).

(2) The brightness temperature corresponding to the minimum region of  $S_K$  is about 3900 K. This may be considered a strong objection against the plausibility of our model if the line source function is equal to the Planck function at this depth, but the  $K_1$  brightness temperature at  $\mu = 0.1$  is 4070 K, and the lower value of 3900 K is obtained by deriving an optimum fit to the observed profile at  $\mu = 0.1$ . The recent observations of Mankin and Strong (1969) indicate a low temperature minimum, although not so low as 3900 K. To demonstrate the effects on the computed profiles of an increase in the minimum value of  $S_K$ , the light dotted curves in Figures A-1 and A-2 show the results of a calculation with a minimum of  $S_K$  corresponding to 4030 K. The profiles are not very sensitive to this change, but the fit is made slightly worse at  $\mu = 0.1$ .

(3) The pronounced limb darkening at all wavelengths is caused in these calculations by two factors. First, the only regions of the solar atmosphere that contribute significantly to the emitted line profile have  $S_K$  increasing inward, and second, the uppermost layer of the atmosphere, with  $\tau_0 < 1$ , has a large Doppler width and a low  $S_K$ , which reduces the emergent intensities more strongly near the limb than near the disk center. Without this feature, the limb darkening between  $\Delta\lambda_2$  ( $\mu = 1.0$ ) and  $\Delta\lambda_1$  ( $\mu = 0.1$ ) is present, but much reduced. Here we denote by  $\Delta\lambda_1$  the wavelength displacement from line center to the secondary intensity minimum.

(4) The most difficult feature of the observations to reproduce is the intensities at  $\Delta\lambda_1$ . All our calculations imply that the emergent radiation at  $\Delta\lambda_1$  ( $\mu = 1.0$ ) is emitted over very nearly the same range of depths as is the radiation observed at  $0.62 \text{ \AA}$  ( $\mu = 0.1$ ). The large difference in observed intensities ( $0.061 I_c$  vs.  $0.037 I_c$ ) is therefore hard to reproduce in our

computations. A somewhat sharper inflection in  $S_K$  near  $\log \tau_0 = 4.5$  will improve the agreement between observed and calculated intensities in the  $K_1$  region at  $\mu = 1$ , but the fit in the wing at all  $\mu$  points becomes worse, and the separation of the computed  $K_1$  ( $\mu = 1.0$ ) and  $\Delta\lambda = 0.62$  ( $\mu = 0.1$ ) intensities is not changed. We illustrate this effect by the heavy dotted profiles in Figure A-1 and the corresponding curve in Figure A-2. Possibly a detailed study of well-normalized profiles in the wings of the K line would solve this problem.

Our results are not unique, in the sense that small changes in our curves will not always change the agreement with the observations. As mentioned above,  $S_K$  in the region  $0.2 < \log \tau_0 < 3.4$  is very poorly determined, but outside this region  $S_K$  must be close to our curve except for very small optical depths. It seems that the gradient in  $v_t$  must be at least as steep as we have plotted, although steeper gradients would give equally good results, and it is possible that slightly smaller maximum values of  $v_t$  could give acceptable results.

The purpose of this Appendix has been to explore the possibilities of a one-component model, as a basis of comparison with the results of two-component calculations, and to serve as a starting point for possible future statistical-equilibrium line-transfer calculations using one-component models. One difficulty in this respect, which can be recognized on the basis of work already done by Athay and Skumanich and others, is that detailed non-LTE line-transfer calculations invariably yield source-function maxima at considerably greater optical depths than we have postulated above. Athay and Skumanich found the source-function maximum occurs near  $\log \tau_0 = 3$ , while our results are similar to those of Zirker and Engvold in having the maxima at  $\log \tau_0 \approx 1$ . It may not be possible to resolve this discrepancy within the assumptions of a one-component model.

## References

- Athay, R. G. and Skumanich, A.: 1968, Solar Phys. 4, 176.
- Beebe, H. A.: 1971, Solar Phys. 17, 304.
- Beebe, H. A. and Johnson, H. R.: 1969, Solar Phys. 10, 79.
- Engvold, O.: 1966, Astrophys. Norvegica 10, 101.
- Houtgast, J.: 1965, Proc. Kon. Nederl. Acad. Wetensch. Amsterdam 68  
(ser. B), 306.
- Linsky, J. L. and Avrett, E. H.: 1970, Publ. Astron. Soc. Pacific 82, 169.
- Mankin, W. G. and Strong, J.: 1969, Bull. Am. Astron. Soc. 1, 200  
(abstract).
- White, O. R. and Suemoto, Z.: 1968, Solar Phys. 3, 523.
- Zirker, J. B.: 1968, Solar Phys. 3, 164.

## BIOGRAPHICAL NOTE

ERIC CHIPMAN received his A.B., M.A., and Ph.D. degrees in Astronomy from Harvard University in 1965, 1969, and 1971, respectively. He is currently working as a Postdoctoral Research Associate at the University of Colorado in Boulder, Colorado. His research interests include the structure of the solar atmosphere and the theory of line formation in the spectra of astronomical objects.

## NOTICE

This series of Special Reports was instituted under the supervision of Dr. F. L. Whipple, Director of the Astrophysical Observatory of the Smithsonian Institution, shortly after the launching of the first artificial earth satellite on October 4, 1957. Contributions come from the Staff of the Observatory.

First issued to ensure the immediate dissemination of data for satellite tracking, the reports have continued to provide a rapid distribution of catalogs of satellite observations, orbital information, and preliminary results of data analyses prior to formal publication in the appropriate journals. The Reports are also used extensively for the rapid publication of preliminary or special results in other fields of astrophysics.

The Reports are regularly distributed to all institutions participating in the U. S. space research program and to individual scientists who request them from the Publications Division, Distribution Section, Smithsonian Astrophysical Observatory, Cambridge, Massachusetts 02138.